INTEGRATED COMPUTER VISION AND MICROSCOPY TOOLS FOR ALL-OPTICAL INTERROGATION OF THE NERVOUS AND MUSCULAR SYSTEMS IN *CAENORHABDITIS ELEGANS*

A Dissertation
Presented to
The Academic Faculty

by

Daniel Akashi Porto

In Partial Fulfillment
of the Requirements for the Degree
Doctor of Philosophy in the
School of Bioengineering

Georgia Institute of Technology
December 2018

INTEGRATED COMPUTER VISION AND MICROSCOPY TOOLS FOR ALL-OPTICAL INTERROGATION OF THE NERVOUS AND MUSCULAR SYSTEMS IN *CAENORHABDITIS ELEGANS*

Approved by:

Dr. Hang Lu, Advisor
School of Chemical & Biomolecular Engineering
Georgia Institute of Technology

Dr. Lena Ting
School of Biomedical Engineering
Georgia Institute of Technology

Dr. Patrick McGrath
School of Biology
Georgia Institute of Technology

Dr. Gordon Berman
School of Biology
Emory University

Dr. Robert Butera
School of Electrical and Computer Engineering
Georgia Institute of Technology

Date Approved: October 26th, 2018

To my mother, father, and sister.

ACKNOWLEDGEMENTS

I would like to first and foremost thank my advisor, Dr. Hang Lu, who has provided invaluable advice, mentorship, and support throughout my studies. She has been a truly amazing advisor, allowing me to grow as a graduate student and teaching me how to be a successful researcher. I would also like to thank my committee members, Dr. Patrick McGrath, Dr. Robert Butera, Dr. Lena Ting, and Dr. Gordon Berman, for providing constructive feedback and guidance in my research. I would also like to thank my collaborators, particularly Dr. Guy Benian, for expanding my understanding and research.

I wish to thank all the current and past members of the Lu Lab, who have helped make my time here a positive experience. I would like to especially thank my "cohort" lab mates, Weipeng Zhuo, Tel Rouse, Fangyuan Zhao, Dr. Yongmin Cho, and Dr. Emily Jackson, for all of their intellectual and emotional support. I also wish to give special thanks to Dr. Ivan de Carlos Cáceres and Dr. Maria Elena de Casas, past members of the lab that were great mentors and provided invaluable guidance. Additionally, I would like to thank Jack Giblin and Yiran Zhao, two dedicated undergraduate students who provided vital contributions to my work.

Lastly, I would like to express my indefinable gratitude to my family for supporting me throughout my studies. I would especially like to thank my mother, Yuko Akashi, who has always encouraged me to pursue my interests. Finally, I would like to give a special thanks to my partner Mary, who has provided unmatched love and support.

TABLE OF CONTENTS

LIST OF TABLES

LIST OF FIGURES

LIST OF SYMBOLS AND ABBREVIATIONS

C. elegans	*Caenorhabditis elegans*
E. coli	*Escherichia coli*
GECI	Genetically Encoded Calcium Indicator
GFP/RFP	Green/Red Fluorescent Protein
ChR2	Channelrhopsin
M9	Buffer suitable for washing off *C. elegans*
NGM	Nematode Growth Medium
OP50	Strain of E. coli used as feedstock for *C. elegans*
PDMS	Polydimethylsiloxane, used for microfluidic devices

SUMMARY

All animals constantly process sensory information from the environment to guide behavioral responses. A fundamental question in neuroscience is to understand how the nervous system uses neuronal circuits to perform neuronal computations between environmental signals and behavioral outputs, or in terms of systems analysis, what are transfer functions that describe this system's function? A key challenge in answering this question in humans is the overwhelming complexity of the human brain. Furthermore, technical challenges limit the capabilities and accuracy of measurements of neuronal activity and behavioral outputs while simultaneously probing parts of the circuit. *Caenorhabditis elegans* is a model organism with a small nervous system consisting of only 302 neurons, and has allowed for the elucidation of genetic and circuit mechanisms of neuronal computations. Additionally, advancements in experimental methodologies such as calcium imaging, optogenetics, and behavior tracking have enabled robust experimentation and analysis. However, conventional instrumentation used to perform these experiments are limited in the integration of these tools and analytical frameworks for extracted data.

This thesis focuses on the development of several integrated platforms to perform optical interrogation of various aspects of the nervous system. I use image processing techniques and microscopy tools to improve the throughput and robustness of both experimentation and analysis. These platforms were implemented to address specific biological questions, and were used in experiments involving phenotyping morphology, measuring neuronal activity using functional imaging, activation of excitable cells using

optogenetics, and behavior tracking using computer vision techniques. Using these platforms, I developed a reverse correlation methodology to systematically inspect the mechanosensation circuit in *C. elegans*. I elucidate linear and nonlinear transformations that characterize the temporal and spatial properties of the neural circuitry, providing models that can predict its function. In another application, I used the developed platforms to perform FRET imaging of muscles in freely moving animals. This enabled the investigation of conformational changes of the muscle protein twitchin *in vivo*. In addition to these two biological investigations, I applied the developed techniques to address other limitations in *C. elegans* research, including robust calcium imaging analysis in microfluidic devices, as well high-throughput screens for a spinal muscular atrophy model and a lipid storage mutant model. Together, the newly developed platforms and analysis pipelines have improved our ability to investigate activities and functions of neural circuits, and have enabled novel insights about the nervous and muscular systems of *C. elegans*.

CHAPTER 1. INTRODUCTION

Our brain is constantly monitoring sensory information in multiple modalities as we traverse through complex environments. A key goal in neuroscience is to understand how the nervous system processes this complex information to guide motor outputs. This aspect of the nervous system, often called sensorimotor integration, is vital for healthy function, and abnormalities in sensorimotor integration are associated with a number disorders, such as Parkinson's, dystonia, and stroke. Additionally, further understanding of sensorimotor integration with a physical framework has implications in the field of engineering, such as with prosthetics and brain-machine-interfaces (BMI). Because of all these implications, sensorimotor integration, and quantitative neuroscience in general has been greatly researched in recent years.

However, even with the great efforts, the biological mechanisms involved in sensorimotor integration are poorly understood in humans. There are both technical and ethical reasons for why it is difficult to probe biological mechanisms of sensorimotor integration in the human brain. Because of this, model organisms have been hugely successful in elucidating universal mechanisms in neuronal processes (i.e. mice, zebrafish, and fruit flies). More recently, the nematode *C. elegans* has gained popularity as an ideal model organism in neuroscience. It has a relatively small nervous system, consisting of only 302 neurons, which has allowed researchers to create a complete wiring diagram of all its neurons, making it the first organism with a fully mapped connectome. Additionally, a large array of genetic tools have been developed and optimized, allowing for in-depth investigations of genetic mechanisms affecting neuronal processes. Lastly, the animal is

optically transparent, allowing for *in vivo* studies with optical tools such as genetically encoded calcium indicators and optogenetics.

Despite the many advantages of *C. elegans* as a model organism, its millimeter body size poses several experimental challenges, such as with handling and manipulating the animals. A large field of research is primarily focused on the generation of technologies to overcome experimental challenges when working with *C. elegans*. Arguably the biggest technological advancement in the *C. elegans* community has been introduction of microfluidics, which has been huge in improving experimental throughput and even allowing for novel experimental paradigms. Another big advancement in the field has been the use of genetically encoded functional sensors and actuators, allowing for non-invasive measuring and probing of neuronal activity. A third key technical advancement has been the use of image processing and computer vision techniques to analyze microscopy images and videos. More detailed background on all these techniques is included in later sections of this chapter. Although these techniques have greatly advanced our understanding of the nervous systems, instrumentation used for these experiments experiments are typically limited to one set of measurements, limiting analysis of simultaneous signals.

In this thesis, I demonstrate a variety of integrated platforms for optical interrogation of the nervous and muscular systems of *C. elegans,* and applications of these platforms to address specific biological questions. The following sections serve as a brief review of prior research on methods of investigation the *C. elegans* nervous and muscular systems, present the limitations of previous methods, and introduce the objectives of this work. Each chapter in this thesis will contain a more detailed introduction specific to that chapter.

1.1 *C. elegans* as model organism in neuroscience

Analogous to the human nervous system, the *C. elegans* nervous system consists of a network of sensory neurons, interneurons, and motor neurons. These neurons are physically connected through both chemical and electrical synapses. In contrast to the human nervous system, the *C. elegans* nervous system is extremely small, consisting of only 302 neurons, all of which have assigned names[1] . Additionally, all the synaptic connections have been mapped, making *C. elegans* the first organism with a fully mapped connectome. This mapped network has been an invaluable tool for studying systems-level neuroscience. For example, the neurons involved in mechanosensation have been elucidated using the knowledge from the connectome in combination with cell-specific ablations[2].

In addition to system-level neuroscience, *C. elegans* has also been shown to be an ideal model for genetic and mechanistic investigations of the nervous system. Many of the key molecules involved in neuronal functions, such as neurotransmitters and voltage-gated channels, have been evolutionarily preserved; the *C. elegans* genome have homologs for the majority of these molecules. Furthermore, the majority of *C. elegans* population consists of hermaphrodites, which produce clonal prodigies in large numbers (~300 per adult). These factors make the worm an ideal animal to perform both forward and reverse genetic screens, elucidating mechanisms and pathways involved in a variety of neuronal processes, such as neurodegeneration, sensory transduction, and learning [3] .

1.1.1 Mechanosensation in C. elegans

The perception of touch arises from various types of mechanoreceptors. In the human hand, there are 4 types of mechanoreceptors, SA1, SA2, RA1, and RA2, which are located throughout the hand[4]. These 4 mechanoreceptors have different receptive fields, allowing for precise and flexible tactile sensation. Although receptive fields for various mechanoreceptors have been thoroughly characterized, they only provide information about the spatial properties of these mechanoreceptors, and not much has been studied about their temporal properties, which are significant for downstream processing in interneurons[5].

Mechanosensation has been widely studied in *C. elegans*. In fact, the neural circuit for touch was one of the first thoroughly mapped circuit[2]. It is now known which sensory neurons act as mechanoreceptors [6], and the interneurons and motor neurons associated with mechanosensation have been elucidated. The types of stimuli that each of the mechanoreceptors respond to have been well characterized. For example, it has been established that six of these sensory neurons, AVM, ALM(L/R), PVM, PLM(L/R), are responsible for gentle touch sensation, whereas the PVD(L/R) neurons have been shown to respond to harsh touch[6]. Although these mechanoreceptors have been thoroughly characterized, their descriptions are mostly qualitative, lacking quantitative information about their temporal and spatial properties. Additionally, many of the mechanoreceptors are presynaptic to the same command interneurons; it is not well understood how these interneurons distinguish between signals from these various mechanoreceptors. In order to address these questions, it would be ideal to characterize spatio-temporal receptive fields for the neurons in the mechanosensory circuit.

1.2 Conventional approaches for investigation of *C. elegans* neural circuits

1.2.1 Behavioral assays

One of the most traditional methods for interrogating neuronal function is to observe how it affects its behavioural outputs by performing behavioural assays. Particularly with *C. elegans*, because of their stereotyped development, behavioural assays allow for investigation of cellular and mechanistic level factors affecting neuronal activity. For example, a number of sensory neurons have been identified by performing behavioural assays to natural stimuli, such as mechanosensation, chemosensation, egg-laying, and many others [6].

1.2.2 Electrophysiology

The conventional method for measuring neuronal activity is by directly measuring its electrical activity with patch clamping [7]. It is still considered the most accurate and precise method for measuring the activity of neurons. Furthermore, patch clamp allows for recording single-channel activity. However, some experimental limitations limit its use in applications requiring high throughputs. First, animals must be immobilized for this procedure, typically with the use of glue. This not only limits the throughput of recording activity, but also the type of experiments possible while performing recordings, particularly observing behavioural outputs. Additionally, suppressing motor commands can have unknown effects on the neuronal activity being measured. Second, the procedure for performing patch clamp experiments with *C. elegans* requires expertise and can be quite laborious, limiting the throughput and scale of experiments possible.

1.3 Optical approaches for investigation of *C. elegans* nervous and muscular systems

1.3.1 Calcium imaging

One of the challenges in neuroscience is the measuring and control of neuronal activity without harming the animal being studied. In recent years, there have been many advances in biomolecular engineering that has allowed for non-invasive, optical measuring and control of neuronal activities. One such technology is calcium imaging with genetically-encoded calcium indicators (GECI), which allows for optical imaging of neuronal activity[8-10]. GECIs are fluorescent molecules that increase their fluorescence when binding to calcium. This provides an optical readout of neuronal or muscular activity because intracellular calcium concentrations increase when these cells are active. This allows for non-invasive measuring neuronal activity. Calcium imaging has been widely used in *C. elegans* to elucidate the function of many neurons without having to use invasive electrophysiology techniques[11-16].

1.3.2 Optogenetics

Another important optical tool that has been growing in neuroscience is optogenetics[17-24]. Optogenetic reagents are molecules that allow for activation of cells using light. One example is Channelrhodopsin (ChR2), which is a proton pump that is activated with blue light. These reagents can be specifically targeted to cell of interest by using genetic promotors. This tool therefore enables direct stimulation of specific neurons in a non-invasive manner. In the past decade, many functional circuits in *C. elegans* have been characterized using optogenetics to probe specific neurons[25-28].

1.3.3 Quantitative Behavior Analysis

Another important aspect of studying *C. elegans* neural circuitry is the analysis of their behavior, as it is the ultimate output of the nervous system. *C. elegans* exhibit a repertoire of behaviors, mostly stemming from variations in locomotion, such as reversals, pauses, turns, or pirouettes. Behavior has been used to assay animals' responses to various stimuli; this includes chemotaxis[29, 30], thermotaxis [31-34], and learning assays[35, 36]. Traditionally, these behaviors were quantified manually by inspecting animals under a microscope. However, in recent years there have been many developments using tracking technologies and computer vision to automatically quantify behaviors [37-45] .

1.3.4 Experimental platforms

All of these techniques have greatly advanced experimentation involving *C. elegans* neural circuitry. Particularly, these tools all use either optical read-outs or optical stimulation of the circuitry. These non-invasive tools allow for more direct investigations of relationships between different parts of the nervous and muscular systems (Figure 2.1). However, conventional instrumentation used to apply these tools do not allow for the integration of multiple types of measurements and probes.

In recent years, there have been many publications involving imaging platforms for performing calcium imaging, optogenetics experiments, and behavior analysis in *C. elegans*. Many platforms are capable of performing calcium imaging in freely moving worms, but are not able to deliver patterned illumination for optogenetics experiments [46-48]. There are some systems capable of delivering patterned illumination in freely moving animals, but are not capable of performing calcium imaging[49, 50]. Recently, a system was published that is capable of patterned illumination for both optogenetics and calcium

imaging in freely moving animals[51], but uses low magnification and has limited spatial resolution, not allowing for control of specific neurons in the head. The platform developed in [52] uses high magnification and can perform simultaneous calcium imaging and optogenetics of individual neurons. However, the platform is not compatible with low magnification and does not allow for whole-animal patterned illumination. There is a physical trade-off between field of view and spatial resolution, and some systems have overcome this problem by using two objectives simultaneously[53]. However, the illumination system of patterned illumination is still limited to only one of the objectives. Altogether, integrated platforms can improve experimentation throughput and capabilities, but tradeoffs need to be considered for specific applications.

1.4 Thesis objective

Although several technical advancements have improved interrogation of neuronal function in *C. elegans*, there are technical limitations to current methods that prevent multi-modal measurements and probing. In order to overcome these technical limitations, the purpose of this thesis is to develop platforms that integrate optical tools with automated computer vision techniques to allow for high-throughput and precise interrogation of the nervous and muscular systems of *C. elegans*.

1.5 Thesis outline

This thesis consists of five chapters. Chapter Two presents a collection of integrated tools developed to investigate neuronal function in *C. elegans*. This work demonstrates the utilization of combining microfluidics with heuristic-based approaches of image processing to answer specific biological questions. Chapter Three presents a novel

approach to interrogate neuronal function in *C. elegans* by using reverse correlation. In this work, an integrated platform for optogenetic stimulus and simultaneous behavior feedback is used to apply reverse correlation, a classic approach used to quantitatively characterize neural systems. Chapter Four presents the application of functional imaging in freely moving animals to investigate conformational changes in twitchin, a key muscle protein. In addition to the validation of the use of integrated systems, this work examines structural dynamics of a specific protein *in vivo*. Lastly, the last chapter provides a conclusion and suggestions for future work.

CHAPTER 2. INTEGRATED COMPUTER VISION AND MICROSCOPY TOOLS FOR ALL-OPTICAL ANALYSIS OF NEURAL CIRCUITS IN *C. ELEGANS*

2.1 Introduction

One of the reasons *C. elegans* has been a successful model organism in neuroscience is its optical transparency, allowing for *in vivo* inspection of its neural circuitry with fluorescence microscopy. Furthermore, microfluidics has greatly improved throughput in *C. elegans* experimentation, particularly with imaging and probing various aspects of its nervous system. However, many labs still rely on generic open-source tools like ImageJ for image analysis. And because of the inherent noise in biological samples, these applications are limited, and manual inspection is typically required for complicated analysis. In recent years, there has been much progress in the development of image processing techniques for inspecting biological samples. Particularly, machine learning has been hugely successful in performing complex analysis of images. Although these algorithms have shown promise, they typically require expertise for use in specific applications and are typically hindered by varying levels of noise in training and experimental sets.

In this chapter, I will highlight various integrated tools, with a focus on heuristic methods, used for experimentation and analysis of *C. elegans* samples. The techniques described in this chapter will highlight the utility of integrating novel software with existing

hardware to improve both throughput and robustness of experiments involving neural circuits in *C. elegans*.

A number of technical advancements, specifically microfluidics, functional imaging, optogenetics, and behavior tracking, have been invaluable in advancing understanding of the *C. elegans* neural circuitry (Figure 2.1). In order to improve throughput and robustness of experiments involving these tools, I developed various platforms that integrate various tools with heuristics-based image processing. These integrated platforms were designed for specific applications in collaborations with other biologists, allowing for novel insights with improved experimentation.

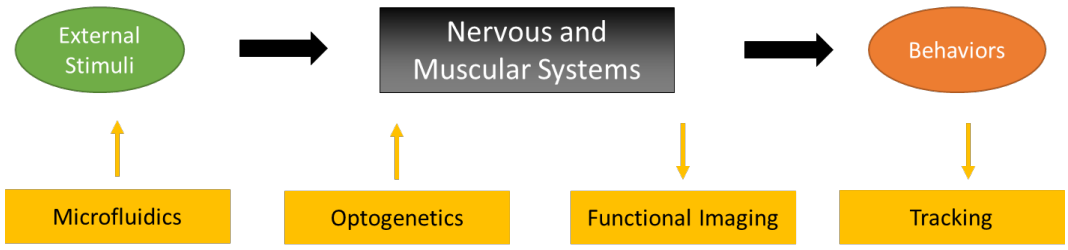

Figure 2.1 State-of-the-art techniques used for measuring and probing different levels of neural circuitry.

In section 1, I demonstrate the use of microfluidics with image processing for performing an automated forward screen of neurodegeneration. In this work, an algorithm was developed to automatically inspect static images of fluorescent animals. In section 2, I develop a neuron tracking algorithm to improve throughput and accuracy in analysis of functional imaging recordings. This tool was combined with a novel microfluidic device to improve mechanosensation experimentation in *C. elegans*. In section 3, I combine the neuron tracker with a previously developed platform for selective illumination. This

platform was used to investigate the neuronal and genetic pathways involved in proprioception.

2.2 Materials and Methods

2.2.1 Microfluidic Devices

Microfluidic devices were fabricated using standard soft lithography methods to create single-layer chips made from the elastomer polydimethylsiloxane (PDMS, Dow Corning Sylgard 184)[54]. Master molds were fabricated as in previous work using silicon wafers, SU-8 photoresist (Microchem), and treated with tridecafluoro-1,1,2,2-tetrahydrooctyl-1-trichlorosilane vapor (United Chemical Technologies) to reduce elastomer adhesion to the substrate[55-57]. Likewise, thermal bonding between a thin (~0.5mm) 20:1 and a thicker (~3mm) 10:1 layer of PDMS was used during chip fabrication to facilitate valve flexibility, while maintaining overall rigidity. After cutting and preparing PDMS devices to interface with tubing and pins, chips were bonded to cover-glass using oxygen plasma. Similar to previous work in the lab, we used partially closed valves and pressure driven flow to route, image, and sort animals within the device.

For the work described in the first section, channel and chip feature height for our presented design is approximately 60μm for all areas excluding the curved portion of the flow channel in the imaging area, which is approximately 40μm. For the work described in the second section, The device consists of a worm inlet/outlet, an imaging channel (50–60 μm deep), and four sets of actuated PDMS membranes. Animals loosely fit in the channel and are trapped (but not held) in the imaging area by two sets of actuated membranes. The width of an actuated PDMS membrane is 150 μm, the distance between

the first and second sets of membranes is 200 μm and that between the second and third sets of membranes is 250 μm. To create the actuated PDMS structure to touch and trap worms, a multi-layer soft lithography process[58] was used. For the bottom flow layer of features, 23: 1 PDMS was deposited via spin coating to create a thin layer. For the top control layer, 10: 1 PDMS was directly poured onto a blank master, which does not have any features, to create a thick and mechanically rigid handle layer. Both layers were then placed into a 90 °C oven for 25–30 minutes until the control layer PDMS was rigid but sticky. After they were manually aligned, additional 10:1 PDMS was poured and cured for several hours to create a rigid handling layer for the device.

2.2.2 C. elegans culture

For all experiments, unless otherwise stated, *C. elegans* was maintained under standard conditions and fed OP50 bacteria. The strains used in this chapter include:

NA1355: gbIs4[Punc-25::smn-1 RNAi sas;Pchs-2::GFP];oxIs12[Punc-47::GFP;lin-15(+)]

NA1330: gbIs4[Punc-25::smn-1 RNAi sas; Pchs-2::GFP]

AQ3236: ljIs142[mec-4::GCaMP6m::SL2TagRFP, unc-119] II; unc-119(ed3) III

TV17924: wyls5007[ser2prom3::GCaMP6, egl-17::mCherry] X

CX10979: kyEx2865[sra-6::GCaMP3, Pofm-1::GFP]

For the genetic screens performed in section 1, for both the manual pilot screen and the automated screen, a standard concentration of the chemical mutagen ethyl methanesulfonate (Sigma Aldrich) was used to mutagenize animals in order to perform a

pooled F2 suppressor screen of gbIs4, the *smn-1*(RNAi sas) mutant. Animals were screened when most animals reached gravid adulthood in terms of age.

2.2.3 Image Processing and Platform Automation

For all image processing, MATLAB® and the MATLAB® Image Processing and Computer Vision Systems Toolboxes were used. System automation describes the process of autonomously controlling all system components to execute animal loading, imaging, phenotype analysis, and sorting. System setup is similar to previous work in the lab, utilizing off-chip components such as pneumatic solenoids, a compound microscope, and a digital CCD camera to control on-chip valves; however, no cooling system was used for immobilization in the studies described in this chapter. All system automation software was programmed in MATLAB® in conjunction with Micro-Manager

2.3 Results

2.3.1 Automated Screening of C. elegans Neurodegeneration Mutants Enabled by Microfluidics and Image Analysis Algorithms

The work described in this section is adapted from a published article [59]. The work was done together with an alumnus of the lab, Dr. Ivan de Carlos Cáceres, and in collaboration with Dr. Elia di Shiavi (IBBR, CNR, Naples, Italy).

2.3.1.1 Background

Neuronal degeneration is a fundamental biological phenomena and a characteristic attribute of neuromuscular diseases, which affect as many as 1 in every 3,000 people [60].

One such disease is spinal muscular atrophy (SMA), an autosomal recessive neurodegenerative disorder that is one of the leading genetic causes of infant mortality [61]. SMA results from a loss of function of survival motor neuron protein (SMN) due to mutations in the SMN1 gene [62, 63]. The decreased SMN function causes specific motor neuron degeneration leading to muscular wasting, paralysis, and even death [61, 64]. Although the genetic bases of SMA have been shown to reside in the SMN1 gene, the molecular mechanisms and pathogenesis leading to SMA remain poorly understood [65]. Currently there are only few well-characterized genetic modulators of human SMN, such as SMN2 and PLS3 [66-68]. Studies using *C. elegans* to discover additional modulators of SMN have utilized visual inspection to measure pharyngeal pumping rates, custom image analysis methods to measure motility, or the COPAS Biosorter to measure animal body length [66, 69-73]. These methods, however, either require manual analysis, are comparatively low-throughput, or provide indirect correlations of motor neuron degeneration. The limitations in these systems, therefore, bottleneck the discovery of SMN modulators and ultimately potential therapies for SMA.

To overcome these limitations, we developed an automated system using microfluidics and computer vision. By manipulating *C. elegans* in microfluidic chips and automatically analysing high-magnitude images, throughput gains up to two orders of magnitude are achieved when compared to manual methods of handling [55]. Additionally, screening of nematodes on-chip can be performed to take advantage of *C. elegans* low cost, rapid life cycle, and large number of progeny [55, 57, 74-76]. Here, for the first time, we present a fully automated system to identify modulators of motor neuron phenotypes using genetic screening techniques. Our system reduces human bias and subjective analysis from

visual screening practices. Phenotype analysis is rapid, performed within 12 seconds per animal on average, as we directly inspect the animal nervous system, removing the need for behavioral analysis or indirect correlations to motor neuron degeneration. We demonstrate the utility of our system by performing an automated screen and isolating 21 mutants that rescue the neurodegenerative phenotype seen in *C. elegans* D-type motor neurons due to the silencing of *smn-1*. Many of the isolated double mutants also show significant improvement of locomotion.

2.3.1.2 Microfluidic device performance and pilot screen

In order to perform genetic screens in an automated manner, we used a single-layer microfluidic device, shown in Figure 2.2. Previous work has shown the potential of microfluidics for vastly improving the throughput of imaging, sorting, and genetic screening studies involving *C. elegans* [55, 57, 74, 75, 77]. However, a key limitation in many of these devices is the lack of orientation control. For this screen, the device was adapted from existing designs, using curved geometries to passively position animals into lateral orientations for improved inspection and imaging [75]. This orientation method is particularly advantageous when inspecting objects along the ventral nerve cord, such as the D-type motor neurons.

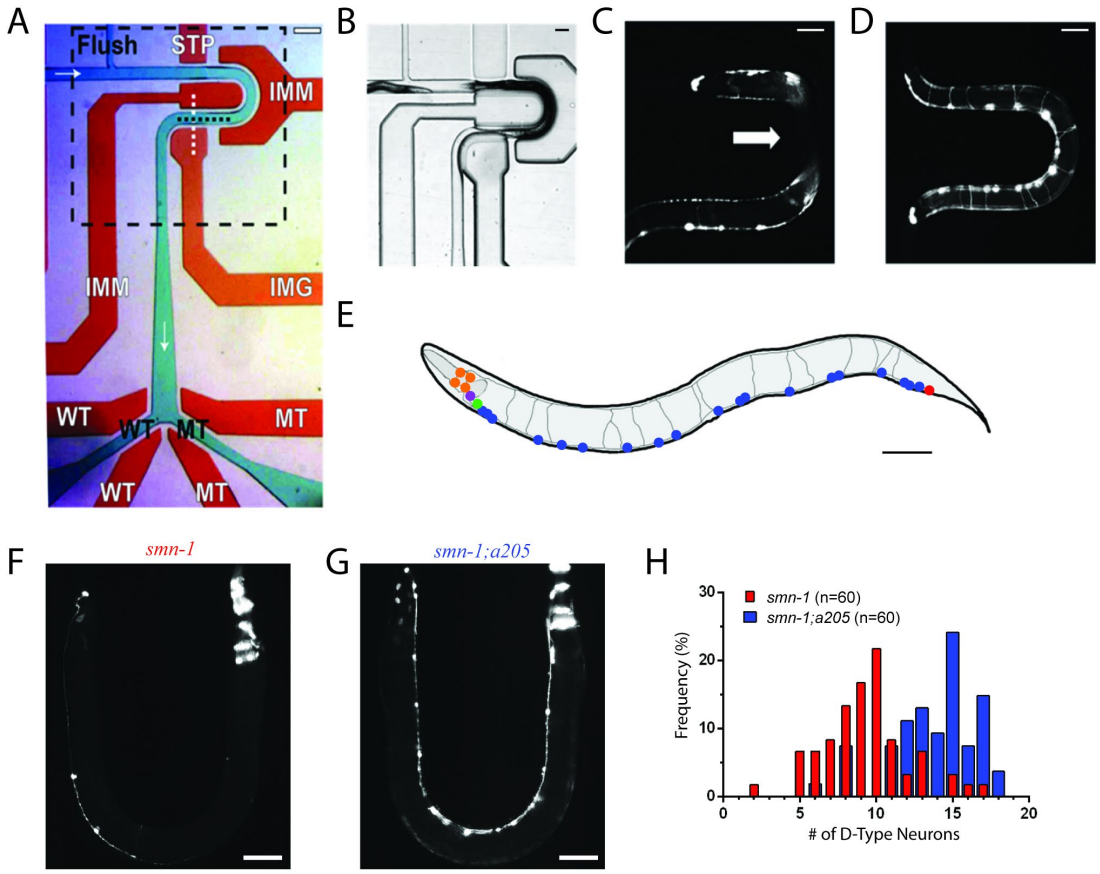

Figure 2.2 Single layer microfluidic device. (A) Device used for on-chip characterization and automated sorting of *C. elegans*. Flow layer is shown in green with black text, valve control layer shown in red with white text. Fluid flows from left to right, top to bottom, and is marked by white arrows. Flush channel, wild-type (WT), and mutant (MT) channels are all labelled. STP is the stop valve, IMM are the immobilization valves, IMG is the imaging valve, and WT and MT are the wild-type and mutant valves. Imaging area shown with dashed black box. Scale bar is 200µm. (B) Imaging area shown in panel A. (C) Example image of an animal body obstructed by immobilization valves. (D) Example image of an animal body not obstructed by immobilization valves. (E) A rendering of a representative image of an adult worm carrying gbIs4[Punc-25::*smn-1*(RNAi sas); Pchs-2::GFP] and oxIs12[Punc-47::GFP] transgenes. D-type motor neurons are shown in blue, cells expressing Pchs-2::GFP co-injection marker in orange, other GABA neurons where *smn-1* is not silenced in red, green and purple. (F) Image of one of the most severe example of *smn-1*(RNAi sas) transgenic animals with 2 out of 19 visible D-type motor neurons. (G) Image of allele *smn-1*;a205 with 16 out of 19 visible D-type motor neurons. Scale bar for all panels is 70µm. (H) Histogram demonstrating differences between motor neuron distributions within the two populations. Figure adapted from [59].

To verify our ability to find suppressors of the *smn-1* mutation using our microfluidic system, we first performed a manual pilot screen of ~1,000 mutagenized animals. We used a strain in which the function of *smn-1* is selectively reduced in D-type GABA motor neurons using a neuron-specific RNAi method [78] (Figure 2.2E). The silencing of *smn-1* in these neurons induces degeneration, detectable as the disappearance of motor neurons expressing GFP (from the oxIs12[Punc-47::GFP] transgene) (Figure 2.2F). We performed mutagenesis on a population of *smn-1*(RNAi sas) mutants and loaded and manually inspected mutagenized animals on-chip to search for animals with a high number of neurons. All animals were inspected as gravid adults as age-associated neurodegenerative diseases in humans demonstrate similar age dependence in many *C. elegans* transgenic models, including ours. From this screen, we isolated allele a205 (Figure 2.2G), which displayed a statistically significant difference in visible neuron number when compared to *smn-1*(RNAi sas) knockdown mutant, 13.8±2.7 for *smn-1*;a205 (n=54) versus 9.3±2.8 for *smn-1* (n=60) respectively (population average ± standard deviation, $p<0.0001$, t-test).

2.3.1.3 Software design and validation for automated screen

My main contribution to this work was on the development and testing of a custom neuron detection software. Figure 2.3A demonstrates the methodology used for detecting an animal within the imaging area of the device, comparing intensities in the background (β), worm (ω), and correct position (ρ) areas. This method uses average intensity thresholds of each region to scan for the presence of nematodes. Figure 2.3B-F displays the step by step process of discovering neurons while minimizing the detection of false positives such as miscellaneous image artefacts, fluorescent co-injection marker present in the head of the

animal, or neurons where *smn-1* is not silenced in the tail. We verified the effectiveness of this method by hand-selecting neurons from a set of high quality images and compared them with our software results. Strain *smn-1*;a205 was used in place of *smn-1* due to interest in isolating similar phenotypes with a comparatively high number of neurons from suppressor screens (14 neurons on average for *smn-1*;a205 versus 9 for *smn-1*).

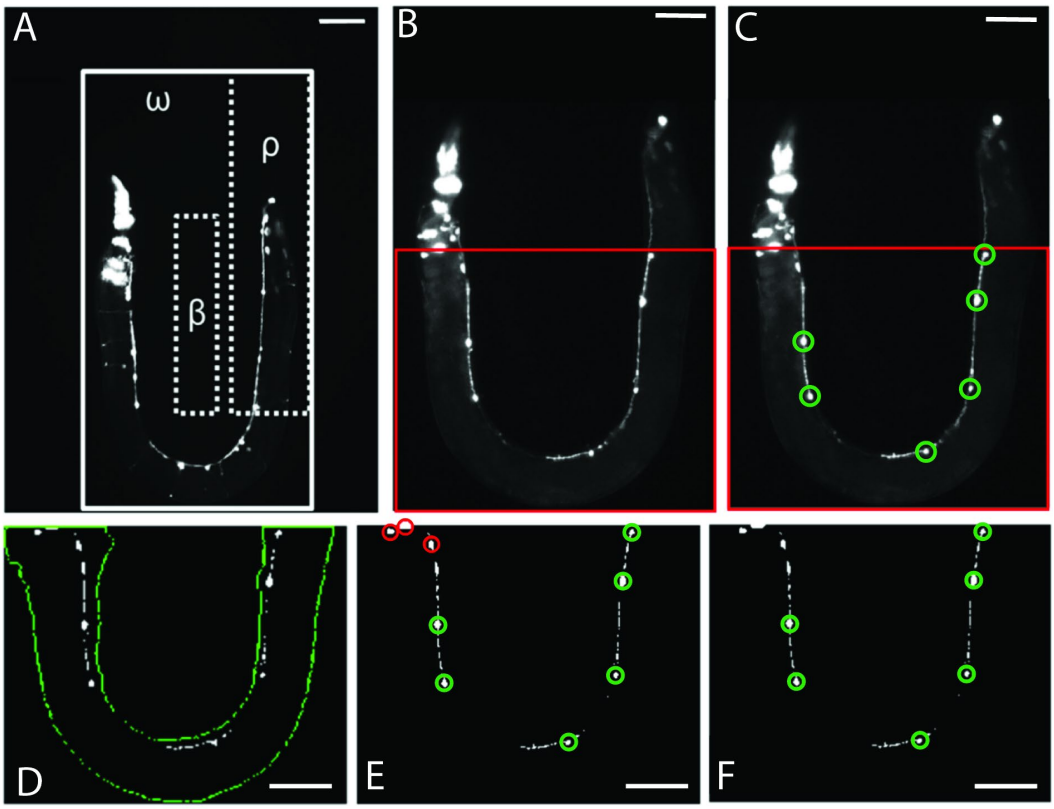

Figure 2.3 On-chip image analysis for system automation. (A) Image of animal taken on-chip with example background (β), worm imaging (ω), and correct position (ρ) regions marked. Solid line borders ω, while dashed boxes show β and ρ. (B) Representative zoomed in image of ω in panel A. (C) Results of image analysis. Detected D-type motor neurons circled in green. Red box in B-C marks analysis area. (D) Segmentation of key features using empirically determined global thresholds. Worm body outline is shown in green while detected objects are shown in white. Objects detected outside of worm body are discarded. (E) Size and morphology filtering to isolate detected neurons. True positive segmentation results from D circled in green. False positive neurons detected during intensity segmentation, but removed due to size and morphological filtering, circled in red. (F) Remaining objects after all

image analysis processes shown circled in green. Scale bar for all panels is 70µm. Figure adapted from [59].

Using these images, we found that our software algorithm was capable of correctly identifying 87% of fluorescently labelled motor neurons in our image library (448 correctly identified out of 513 determined visually, 56 total images). The amount of false positives, or objects detected by our program that were not actually neurons was 8% (39 of all 487 objects detected); while the amount of false negatives, or actual neurons that were not detected by our software, was 13% (65 of 513 visually determined neurons). The average number of false positives per image was 0.7±0.8, while false negatives per image was 1.2±1.3 (mean ± standard deviation, n=56).

Reviewing segmented neurons from our image library reveals that most false positives are due to mistaking puncta, RME or DVB neurons, and cells expressing the co-injection marker, for D-type motor neurons. Size filters in our custom software reduce the number of puncta and RME neurons detected by removing objects too small or too large to be considered D-type neurons. However, a careful balance must be maintained when setting size thresholds as altering ranges to decrease false positives can simultaneously increase the number of false negatives, resulting in actual neurons not meeting requirements for detection. In this work, size thresholds were determined from empirical results and set to values to minimize the amount of both false positives and negatives.

To further decrease the number of false positives, we also limited the area of image analysis (area labelled in red in Figure 2.3B), and applied a mean filter to binary images. Image analysis was reduced to the mentioned area due to the observation that curved device geometry places head and tail regions in the same image section. Therefore, removing these

areas from analysis decreases the risk of detecting false positives in head and tail regions which contain RME and DVB neurons, as well as cells expressing the co-injection marker. To compensate for occurrences when the head area of the animal is within our analysis region, we use a mean filter to combine and remove any objects within close proximity of each other that are falsely detected as neurons. While the head region of animals are the most prone to detection of a high number of false positives (Figure 2.4A-B), this can also occur due to animals with egg laying deficiencies (Figure 2.4C-D), or due to multiple animals within the analysis region (Figure 2.4E-F).

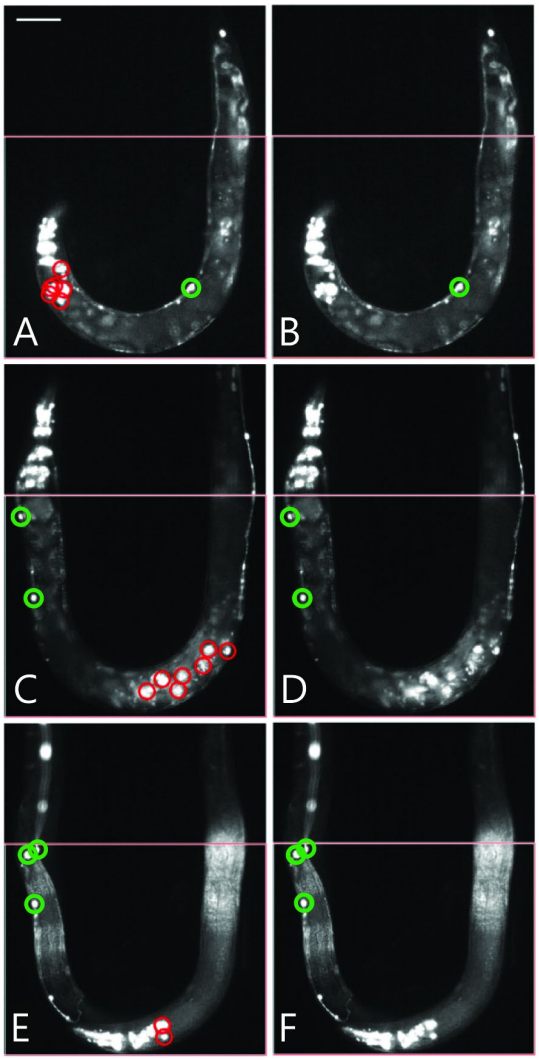

Figure 2.4 Application of mean-filter to remove false positives. (A) Image of randomly mutated *smn-1*(RNAi sas) animal loaded on-chip with the head region present in the analysis area. Co-injection marker expressing cells, not removed by previous analysis steps, are falsely detected as neurons, labelled in red. (B) Results of mean and size filter to remove false-positives from panel A. Objects that were previously detected in the head region have been removed. Final results shown in green. (C) Image of randomly mutated *smn-1*(RNAi sas) animal loaded on-chip demonstrating egg laying deficiency. Fluorescent markers of progeny within parent falsely detected as neurons labelled in red. (D) Results of mean and size filter, objects previously detected within the animal body removed. Final results shown in green. (E) Example of multiple animals within the imaging area. Falsely detected neurons from the head of one animal are detected along with neurons from the other animal's body. Falsely detected D-type neurons shown in red. (F) Results after applying mean and size filter to remove co-injection markers seen in head of worm. Final results shown in green. Scale bar for all panels is 70µm. Figure adapted from [59].

False negatives detected in our sample image library can be attributed to neurons not meeting minimum or maximum size threshold requirements. These instances occur when neurons are too small due to natural variation between animal expression and size, or too large due to diffused light from out of focus neurons. Images captured for analysis within our device are captured at a single focal plane, which expedites the time required for image acquisition and removes the need for further immobilization schemes typically required for Z-stacks. Additionally, we do not observe a focus drift during our experimental sessions.

While any error in our detection results is undesirable, we are especially concerned with high numbers of false positives because they mimic a partial rescue phenotype. In this case, we err on the side of having a higher number of false negatives than false positives as putative suppressors require further phenotyping to assess penetrance and degree of rescue. Software results from testing on our sample image library show that both the average false positive and false negative rates for neuron detection are approximately one neuron, and are considerably low when compared to the average difference in neuron number between *smn-1*(RNAi sas) phenotype and suppressors of that mutation (approximately five). Therefore, neuron detection software is adequate for an automated screen.

2.3.1.4 Automated screen for suppressors of *smn-1* silencing

To test the ability of our system to successfully identify and sort suppressors of the *smn-1*(RNAi sas) phenotype (referred to as double mutants from this point forward), we performed an automated pilot screen of over 7,500 F2 mutagenized animals (>750 haploid

genomes). Our average screening rate was approximately 300 animals per hour, calculated over 8 trials on different days, and utilizing multiple microfluidic devices of identical design. All animals were imaged and analyzed using a single focal plane on-chip, determined manually at the beginning of each screen. Similarly, analysis regions for automated worm detection were manually selected at the beginning of each automated screening experiment.

In this automated screen, we isolated 74 potential double mutants. Of these double mutants detected and sorted by our automated system, approximately 62% were visually verified as having phenotypes different from *smn-1*(RNAi sas) mutants, containing 10 or more neurons within the analysis area (n=46 over 74 total mutants). This analysis, however, takes into account double mutants sorted before the implementation of a mean filter to reduce the number of false positives in neuron detection. Analysing only mutants sorted after the implementation of the mean filter increases the sorting accuracy of our system to 85% (n=23 of 27 total).

Many factors can lead to classification errors during automated phenotype analysis due to the random nature of forward genetic screens. Differences in body size (affecting head position), loading of multiple worms into the imaging area, or animals with progeny that have hatched inside of them complicate analysis, normally requiring individual software solutions specific for each circumstance. However, using a mean filter as the final step in neuron detection provided a single solution for these issues while increasing the sorting accuracy of our system 23%.

2.3.1.5 Characterization of isolated alleles

From our potential pool of 74 double mutants, we decided to confirm the data from the automated screening by manual inspection and scoring of each population. This secondary screening resulted in 21 suppressors of the *smn-1*(RNAi sas) phenotype (Figure 2.5), isolated from eight different pooled populations. A table of the number of neurons for each isolated allele is listed in Table A.1. All double mutants were found to be statistically different when compared to the *smn-1*(RNAi sas) single mutant ($p<0.0001$ for all alleles except a185, which is $p<0.001$, one-way ANOVA Dunnett's post-test).

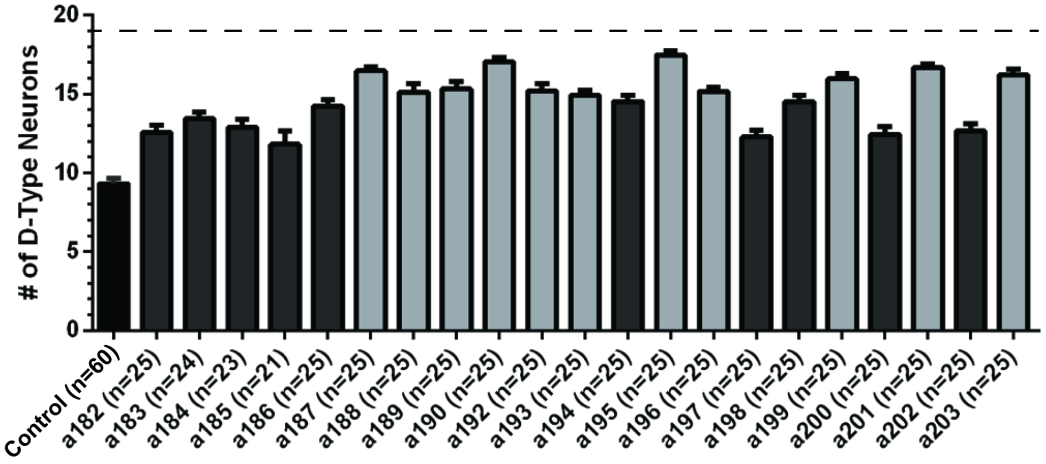

Figure 2.5 Average number of D-type motor neurons per allele. Error bars represent standard error of mean. Control is shown in black (non mutagenized) and corresponds to *smn-1*(RNAi sas) single mutant; isolated alleles are shown in grey. All animals carry the transgenes oxIs12[Punc-47::GFP] and gbIs4[Punc-25::*smn-1*(RNAi sas)]. Dashed line corresponds to wild-type condition, where all 19 motor neurons are always visible. Lighter grey designates alleles considered to be strong suppressors of the *smn-1*(RNAi sas) phenotype. Data were obtained by manual scoring the double mutants. Figure adapted from [59].

Figure 2.6A demonstrates the cumulative distribution functions (CDF) for all isolated double mutants which can be used to visualize the differences in numerical distributions between alleles. Analyzing the CDF illustrates the effect of the allele for

suppressing the neurodegenerative phenotype of *smn-1*(RNAi sas) in a whole population. The farther right shifted the distribution function is, the more consistent the suppression. Furthermore, this characterization demonstrates the variability in the phenotypes of *smn-1* and the discovered suppressor mutants. The CDF for alleles a194-a198 and a202-a203 are shown in Figure 2.6B and display varying levels of *smn-1*(RNAi sas) rescue for strains isolated from the same pooled population. A histogram of three representative alleles from this group is shown in Figure 2.6C and reveals the small amount of overlap between each double mutant, demonstrating unique phenotypes among potential siblings. These comparisons illustrate that our system is capable of capturing animals with varying levels of *smn-1*(RNAi sas) rescue, even when screening for single animals. Additionally, our system is not limited to only strong suppressors of the neurodegenerative mutation.

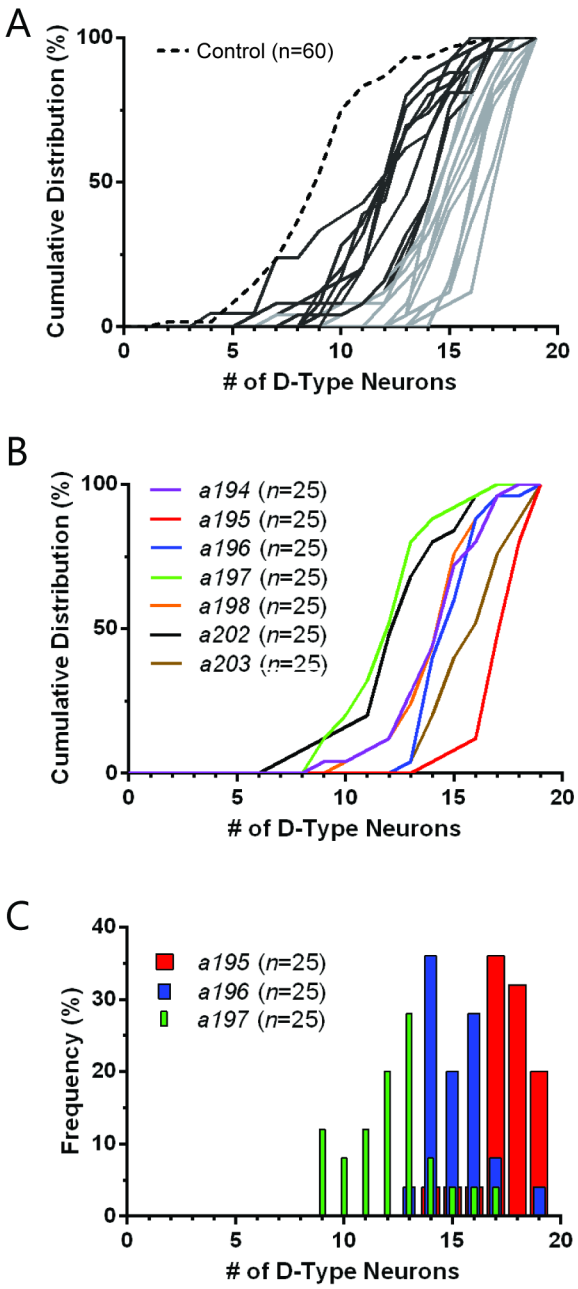

Figure 2.6 Characterization of isolated alleles. (A) Cumulative distribution functions (CDF) for isolated alleles from automated suppressor screen. Control is *smn-1*(RNAi sas) single mutant (non mutagenized) and is shown in dashed black line;s putative double mutant alleles in grey. Lighter grey designates alleles considered to be strong suppressors of the *smn-1*(RNAi sas) phenotype. (B) CDFs for seven alleles isolated from same F1 parent population (possible siblings). (C) Histogram for alleles a195, a196, and a197 shown in panel B. Only data from manual scoring, not image analysis, was used for this figure. Figure adapted from [59].

To verify whether any of the mutant alleles affects the RNAi machinery, thus causing a non-informative "technical" suppression of *smn-1*(RNAi sas) induced degeneration, we silenced *mom-2* essential gene using RNAi by feeding [79] (Figure 2.7). RNA interference of *mom-2* causes a fully penetrant embryonic lethality in wild-type animals and *smn-1*(RNAi sas) non-mutagenized parental strain and this phenotype is completely suppressed in *rde-1* knock out animals, which are strongly resistant to RNAi. Among the 21 suppressors obtained from the secondary screening, only 10 alleles showed 100% lethality, while four showed an almost complete suppression of the phenotype, similar to *rde-1* positive control mutant strain, and therefore discarded from further analysis. To demonstrate that the suppression of *smn-1*(RNAi sas) neurodegenerative phenotype corresponds to a functional rescue of the effects caused by *smn-1* silencing, we tested the locomotion behaviour of suppressor alleles (not impaired in RNAi) choosing the strongest and healthy ones. The regulation of *C. elegans* backward movement involves D-type motor neurons [80] and the silencing of *smn-1* in these neurons causes severe defects in locomotion [78]. Most of the alleles tested show a strong and significant increase in the number of animals with a normal backward movement compared to *smn-1* alone (Figure 2.8), confirming a functional rescue and the role of 9 isolated alleles in suppressing various *smn-1*(RNAi sas) induced defects. Unexpectedly all these alleles showed a dominant or semidominant mode of inheritance, except a196 allele.

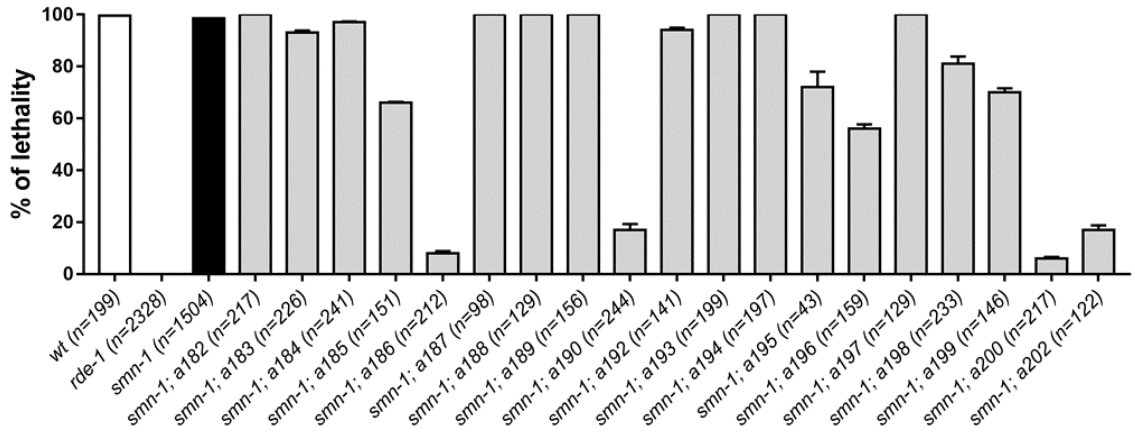

Figure 2.7 Characterization of the RNAi efficiency in isolated alleles by silencing mom-2 essential gene. Each bar represents the percentage of unhatched eggs over the entire progeny laid. Error bars represent standard error of mean. The total progeny scored is indicated (n). Only a186, a190, a200, a202 alleles present a severe impairment in the RNAi machinery, below 50% of lethality. All animals, except the wild-type (wt) and rde-1(ne219), carry the transgenes gbIs4[Punc-25::*smn-1*(RNAi sas)]; oxIs12[Punc-47::GFP]. Figure adapted from [59].

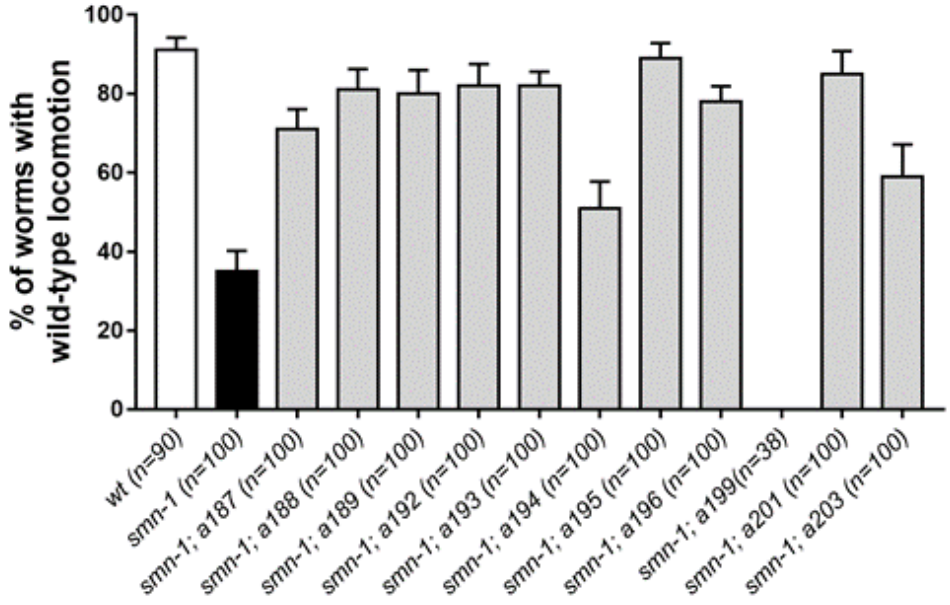

Figure 2.8 Most of the interesting alleles rescue the defect in locomotion of *smn-1*(RNAi sas). Each bar represents the mean percentage of animals with a normal backward locomotion. Error bars represent standard error of mean. The number of animal tested is indicated (n). All the alleles present a significant rescue compared to

***smn-1* alone (P<0.005, non-parametric Kruskal-Wallis test), except a194 (P=0.2434) and a199 which are completely immobile. All animals, except the wild-type (wt), carry the transgene gbIs4[Punc-25::*smn-1*(RNAi sas)]. Figure adapted from [59].**

2.3.2 Automated and controlled mechanical stimulation and functional imaging in vivo in C. elegans

The work described in this section is adapted from a published article [81]. The work was done together with an alumnus of the lab, Dr. Yongmin Cho, and in collaboration with Dr. William Schafer (Medical Research Council Laboratory of Molecular Biology, Cambridge, UK) .

2.3.2.1 Background and Justification

C. elegans is a useful genetic model system for investigating mechanisms involved in sensory behavior which are potentially relevant to human diseases. While utilities of advanced techniques such as microfluidics have accelerated some areas of *C. elegans* sensory biology such as chemosensation, studies of mechanosensation conventionally require immobilization by glue and manual delivery of stimuli, leading to low experimental throughput and high variability. In this section, I present work in collaboration with a previous member of the lab, Dr. Yongmin Cho, where we develop a microfluidic platform that precisely and robustly delivers a wide range of mechanical stimuli and can also be used in conjunction with functional imaging and optical interrogation techniques. The platform is fully automated, thereby greatly enhancing the throughput and robustness of experiments. We show that the behavior of the well-known gentle and harsh touch neurons and their receptive fields can be recapitulated. Using calcium dynamics as a read-out, we demonstrate its ability to perform a drug screen in vivo. In addition, I build on calcium

imaging analysis to characterize activity in neuronal processes in addition to cell bodies. We envision that this system will be able to greatly accelerate the discovery of genes and molecules involved in mechanosensation and multimodal sensory behavior, as well as the discovery of therapeutics for related diseases.

2.3.2.2 Neuron Tracking and Custom GUI allow for precise and high-throughput quantification of calcium signals

In collaboration with Dr. Yongmin Cho, a microfluidic device was optimized to deliver precise and repeatable mechanical stimuli to different anatomical regions of *C. elegans* (Figure 2.9). Animals are loaded into an imaging channel (where the animals are not immobilized but their movement is much reduced from freely moving behavior), and mechanical stimuli are delivered through two pairs of in-plane PDMS membrane structures (Figure 2.9A). Our design and the fabrication protocol allows deflections and deformations in similar ranges to conventional approaches, and roughly linear with the actuation pressure (Figure 2.9B). This design retains animals in plane and relatively stationary but not fully immobilized, thus allowing high quality imaging of calcium transients in cell bodies and subcellular processes (Figure 2.9C).

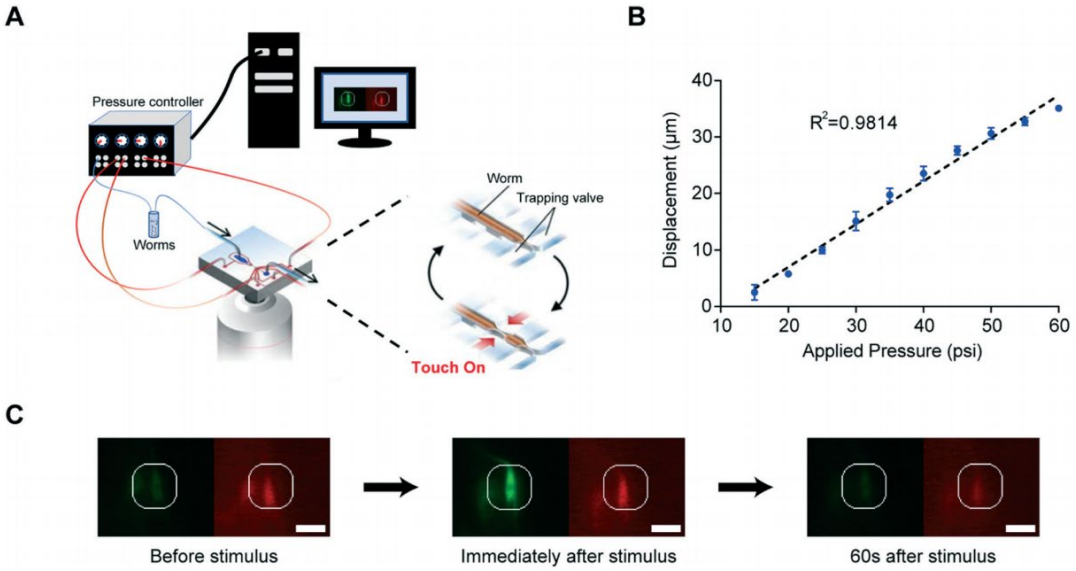

Figure 2.9 The microfluidic platform can robustly deliver a mechanical stimulus and allow imaging of calcium responses in *C. elegans* mechanoreceptor neurons. (A) An integrated system for automated functional imaging of *C. elegans* in microfluidic devices. Individual animals were sequentially loaded via a pressure-driven flow. The device employs multiple sets of actuated structures: valves to trap animals in a reproducible position and two sets of actuation valves used to deliver mechanical stimuli to different regions of the body. All actuators and loading procedures were automatically controlled by a customized MATLAB script. (B) Displacement of the actuated membrane by applying pressure (n = 4 worms). Measurements were obtained from images of transgenic worms expressing GFP along the body-wall muscle (stEx30[myo-3p::GFP + rol6(su1006)]). The R-squared value is 0.9814. (C) Sample frames from an activated neuron show changes in fluorescence due to the mechanical stimulus. Because neurons of interest move during recordings due to the mechanical stimulus and behavioural responses, a tracking algorithm was developed to automatically record the GCaMP and RFP intensities from individual trials. Scale bar: 10 µm. Figure adapted from [81].

To automatically identify the fluorescently labelled neuron of interest and extract quantitative calcium transients, we developed a neuron tracking algorithm (Figure 2.10). This was necessary because worms are not fully immobilized in the device, and mechanical stimuli often caused the neuron of interest to move within the field-of-view. The neuron tracking algorithm consists of a series of image processing steps applied to each frame of a recording. For each frame i, raw images are processed through a blob filter (Laplace of

Gaussian filter) to improve contrast and facilitate segmentation. Blob filtered images are segmented by applying an empirically determined threshold. The neuron of interest is identified by the user in the first frame, and by distance to the neuron in the previous frame. Lastly, once the neuron is detected for each frame, intensity values are extracted (Green ROI, Red ROI, Green Background, and Red Background).

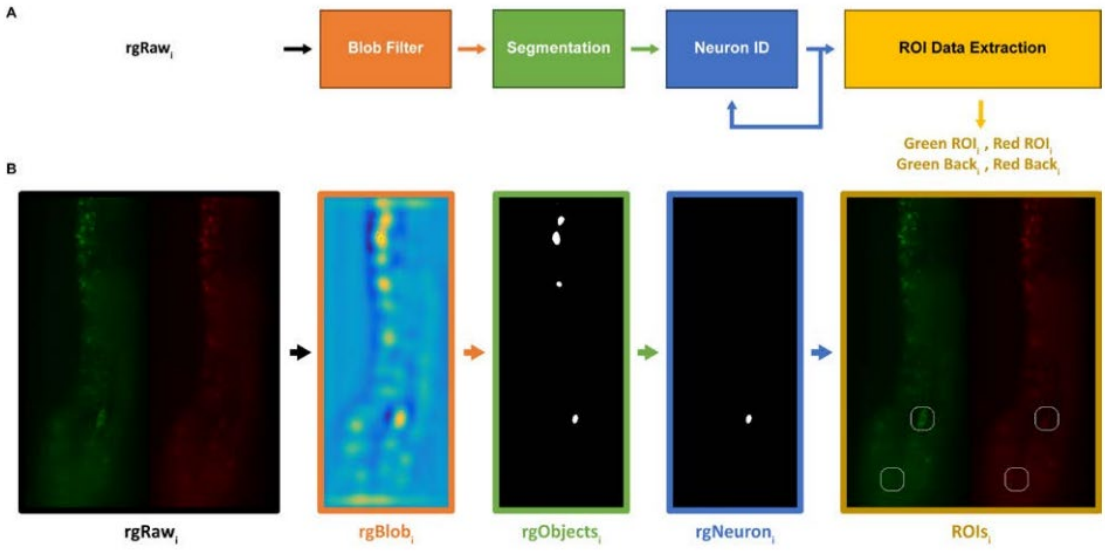

Figure 2.10 Neuron Tracker Algorithm. A) Algorithm schematic. B) Sample frame.

In order to analyze calcium recordings in a robust manner, we also developed an easy to use graphical-user-interface (GUI) (Figure 2.11). The program was designed to enable single neuron tracking for fluorescence recordings of any given neuron. The GUI makes it easy for any researcher to extract quantitative information from recordings. The user simply has to set the parameters for the tracker, and the algorithm will automatically analyze every frame of the recording. Another key feature of the GUI is that it allows for user supervision during the automated analysis. This allows the user to interrupt the program if a tracking error occurs, and manually correct the ROI that includes the neuron

of interest. By combining the tracking algorithm with supervised automation, we improve the throughput while maintaining the accuracy of analysis.

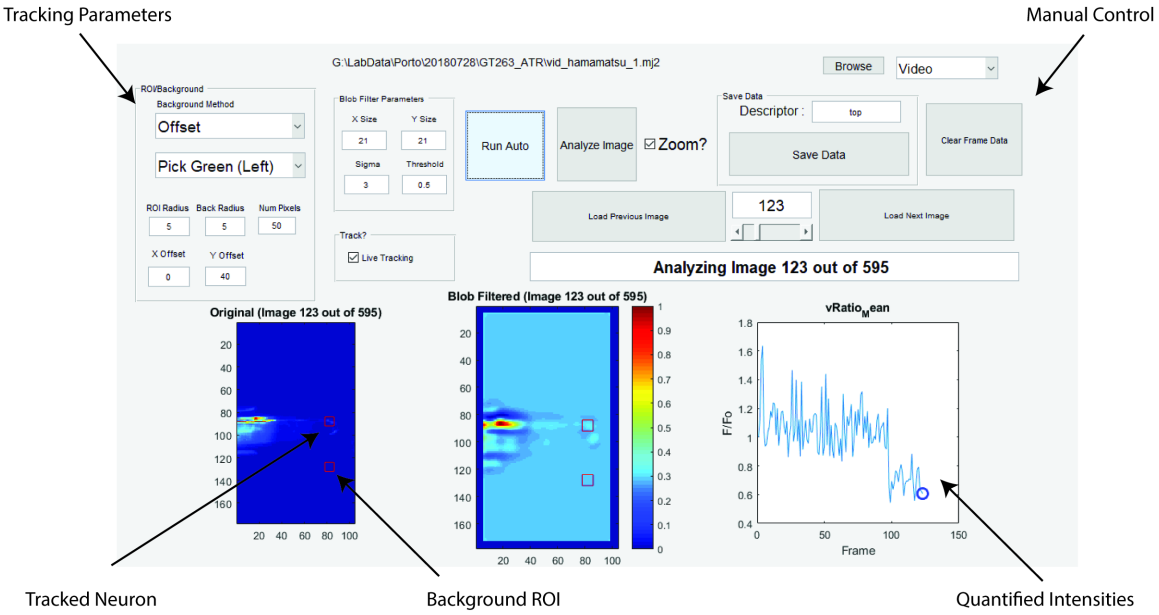

Figure 2.11 Screenshot of Graphical User Interface (GUI) designed for using neuron tracker algorithm to analyze calcium imaging recordings. Manual Control of analysis enables for user supervision of the automated tracking algorithm.

2.3.2.3 Tracking of neuronal processes in calcium imaging recordings for spatiotemporal analysis

The neuron tracker software has shown to be a great tool for extracting fluorescence intensity in the cell body of neurons. However, this method does not provide spatial patterns of activity along axons or dendrites. While neuronal processes are known to encode information through spatial activity, this information is uncharacterized in typical calcium imaging recordings, due to technical limitations including the relative dimness and varying shapes of neuronal processes.

In addition to the neuron tracker algorithm, I have also worked on a new method for analyzing calcium activity in neuronal processes to produce a spatial map of activity. In order to segment the relatively dim neuronal processes, we employ a series of image processing methods to individual frames of a calcium imaging recording. A tracking algorithm is used to track specific branches and extract calcium activity throughout the recordings. We applied this technique to inspect the calcium dynamics in the processes of several neurons, including the gentle touch neurons ALM, AVM, and PLM, and the nociceptive neuron PVD. By using this method, we can produce spatiotemporal maps of activity in specific branches (Figure 2.12). Ultimately, this approach provides a new method of analyzing standard calcium imaging recordings and enables the visualization of previously uncharacterized activity in neuronal processes.

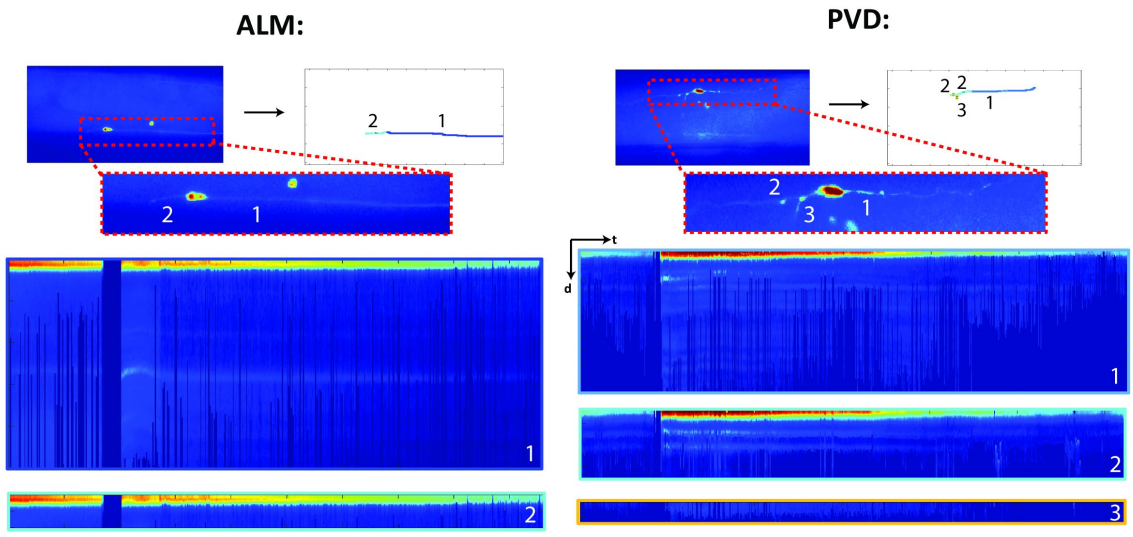

Figure 2.12 Spatiotemporal analysis of calcium recordings. Individual processes are segmented and tracked to create spatiotemporal maps of calcium activity. This method was applied to ALM (left) and PVD (right). Each heatmap represents extracted activities for an individual branch, with the x-axis representing time and y-axis representing distance from beginning of branch.

2.3.3 Investigation of Proprioception in C. elegans using Simultaneous Calcium Imaging and Optogenetics

2.3.3.1 Background

Calcium imaging is now one of the most widely used techniques for measuring neuronal activity in *C. elegans*. An orthogonal optical technique for controlling neuronal activity is optogenetics. Analogous to calcium imaging, optogenetics typically refers to the use of genetically encoded light-activated channels, allowing for optical probing of excitable cells. Therefore, with the combination of these two techniques, we can perform both "reads" and "writes" of specific neurons using only light.

There are several challenges to performing experiments with both of these techniques simultaneously. The biggest challenge is the overlap in excitation wavelengths for common reagents. Specifically, the most commonly used GECI in *C. elegans* is GCaMP and its variants, which are all excited by blue light. Similarly, the most commonly used reagent for optogenetics in channelrhodopsin (ChR2), which is also excited by blue light. This overlap in wavelengths is a huge barrier for experimentation, as imaging GCaMP will consequently activate neurons expressing ChR2, making it impossible to determine whether measured activity was caused by the stimulus.

2.3.3.2 Selective illumination enables simultaneous calcium imaging and optogenetic probing

One solution to overcoming the spectral overlap in excitation wavelengths is to develop reagents with different operational wavelengths. Indeed, over recent years there

have been many research groups that have developed a number of GECIs and optogenetic reagents with varying excitation wavelengths. However, the creation of new strains with novel reagents requires a large degree of expertise limited to biological laboratories, and is extensively laborious, typically requiring months of work.

In this work, we sought to develop a platform for simultaneous calcium imaging and optogenetic probing with the same color. We use an approach similar to [52], where selective illumination with varying intensities is used to separate the two modalities; a low-intensity blue light is used to excite and image GCaMP, and a high-intensity blue light is used to excite ChR2. Guo et al combine a microscope with a DLP array, allowing for selective illumination of patterns with high precision. In our platform, we use the projector-microscope setup to deliver selective illumination. By using the additional optics for fluorescence imaging, we can image GCaMP as well as provide the excitation light for ChR2. Using our platform, we can selectively illuminate regions with a precision of ~10um, and provide a large enough dynamic range of intensities to separately excite GCaMP and ChR2.

2.3.3.3 Investigation of PVD as proprioceptive neuron

We use the developed platform to investigate the function of PVDs as proprioceptive neurons. Proprioception is the sense of one's own body posture and movements. In other words, proprioceptive sensory systems provide feedback of muscle activity back to neural circuits.

In order to test PVD's function in proprioception, we sought to use our platform to measure the activity in PVD's cell body in response to muscle activation. We used

optogenetics to stimulate body wall muscles and calcium imaging to measure activity in PVD. To do this, we created a line of worms expressing ChR2 in body wall muscles and GCaMP in PVD. We used a microfluidic device consisting of a single channel to partially immobilize animals, allowing for high-magnification imaging of the PVD cell bodies while allowing for the animal to actuate its muscles. The projector-microscope platform was used to deliver selective illumination to stimulate muscles, as well as providing a low-level excitation intensity to simultaneously image PVD (Figure 2.13). Animals were robustly stimulated using this experimental setup, with contractions being clearly visible upon stimulation.

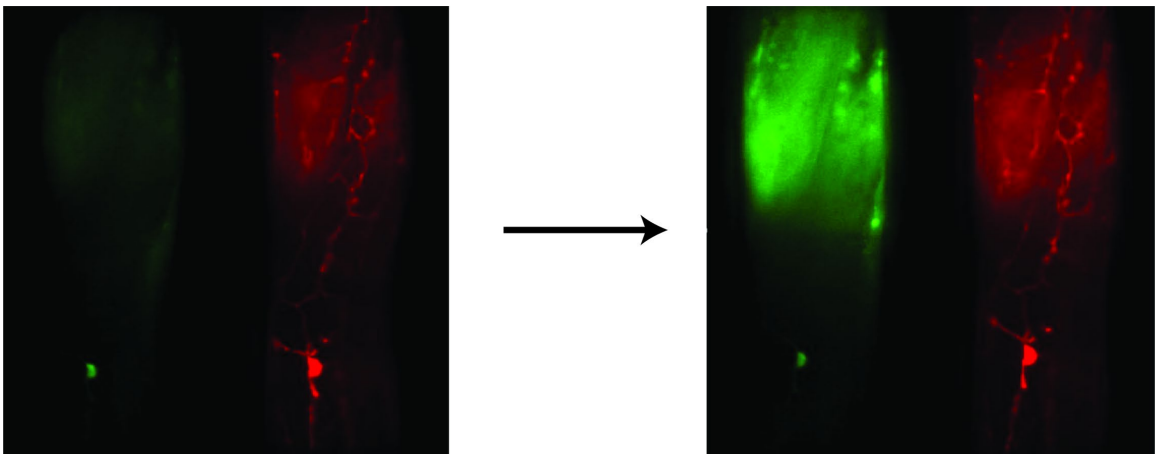

Figure 2.13 Selective Illumination of Muscles with simultaneous calcium imaging of PVD.

The neuron tracker algorithm was used to analyze recordings, extracting calcium traces of PVD in response to muscle activation. We tested animals fed ATR, a cofactor required for ChR2 function, as well as control animals that were not fed ATR. Unfortunately, we did not observe significant differences in PVD activity between the two groups (Figure 2.14). Neither group showed reliable activity in response to the light

stimulus, although interestingly both groups showed spontaneous bursts of activity. Further investigation can be done to optimize light stimulus patterns that can reliably activate PVD.

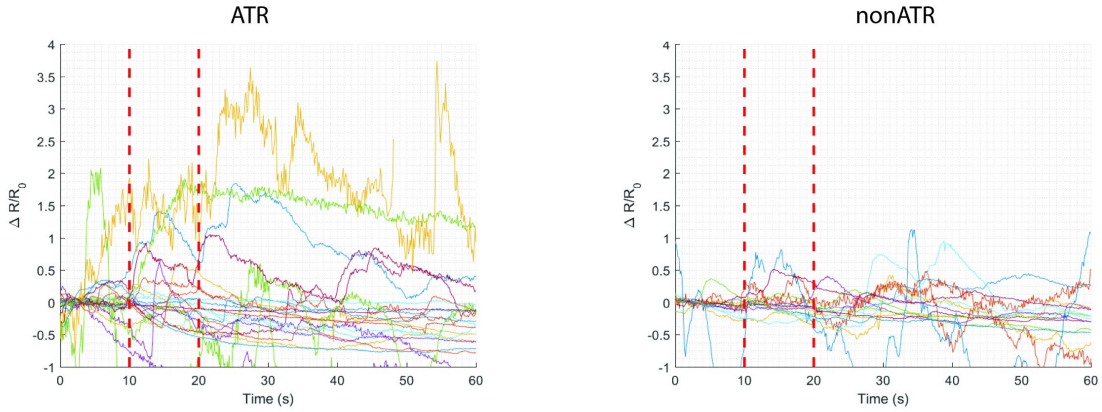

Figure 2.14 Sample traces of calcium activity in PVD in response to optogenetic activation of muscles.

2.4 Discussion

In this chapter, I have described three different applications of integrating novel software with existing hardware to improve both throughput and robustness of experiments involving neural circuits in *C. elegans*. In section 1, I demonstrate the use of microfluidics with image processing for performing an automated forward screen of neurodegeneration. In this work, an algorithm was developed to automatically inspect static images of fluorescent animals. In section 2, I develop a neuron tracking algorithm to improve throughput and accuracy in analysis of functional imaging recordings. This tool was combined with a novel microfluidic device to improve mechanosensation experimentation in *C. elegans*. In section 3, I combine the neuron tracker with a previously developed platform for selective illumination. This platform was used to investigate the neuronal and

genetic pathways involved in proprioception. In all applications, novel platforms designed for the specific applications allowed for robust experimentation and analysis.

In addition to the examples highlighted in this chapter, I use the technologies described in this chapter to perform in-depth investigations of the nervous and muscular systems in *C. elegans* in the following chapters. In chapter 3, I use the selective illumination platform to develop a reverse correlation methodology and investigate the spatial and temporal dynamics of the mechanosensation circuit in *C. elegans*. In chapter 4, I perform functional imaging in freely moving animals to investigate the function of the muscle protein twitchin. Altogether, the newly developed tools I describe in this chapter have not only advanced experimental and quantitative methodologies, but also allowed for novel biological insights.

CHAPTER 3. REVERSE-CORRELATION ANALYSIS OF THE MECHANOSENSATION CIRCUIT AND BEHAVIOR IN *C. ELEGANS*

Animals must integrate the activity of multiple mechanoreceptors to navigate complex environments. In *Caenorhabditis elegans*, the general roles of the mechanosensory neurons have been defined, but most studies involve end-point or single-time-point measurements, and thus lack dynamical information. In this chapter, I formulate a set of unbiased quantitative characterizations of the mechanosensory system by using reverse correlation analysis on behavior. I use a custom tracking, selective illumination, and optogenetics platform to compare two mechanosensory systems: the gentle-touch (TRNs) and harsh-touch (PVD) circuits. This method yields characteristic linear filters that allow for prediction of behavioral responses. The resulting filters are consistent with previous findings, and further provide new insights on the dynamics and spatial encoding of the systems. The results suggest that the tiled network of the gentle-touch neurons has better resolution for spatial encoding than the harsh-touch neurons. Additionally, linear-nonlinear models accurately predict behavioral responses based only on sensory neuron activity. This platform captures the overall dynamics of behavior induced by the activation of sensory neurons, providing simple transformations that quantitatively characterize these systems. Furthermore, this platform can be extended to capture the behavioral dynamics induced by any neuron or other excitable cells in the animal.

3.1 Introduction

A key function of the nervous system is to integrate the activity from a variety of sensory neurons and transform these neuronal signals into specific behavioral responses. This integration occurs not only across sensory modalities but also spatially and temporally within a single modality such as in mechanosensation [4]. Characterizations of how the nervous system processes this information is vital for understanding brain function and allowing for prediction of behavioral responses. *Caenorhabditis elegans*, a nematode with a mapped connectome and powerful genetic and physiology tools, is an effective model organism for investigating relationships between sensory inputs and downstream activity [82, 83]. The components of the neural circuits involved in *C. elegans* mechanosensation have been elucidated through various genetic and behavioral analyses, coupled with neuronal cell ablation assays [2, 84, 85]. Two sets of mechanoreceptors are specifically responsible for sensing touch throughout the body: the gentle touch sensing TRNs and harsh touch sensing PVDs [6]. These specific neurons have been the focus of a number of studies, including genetic dissections of the mechanical signal transduction, their calcium responses and the eventual behavioral outcomes [2, 81, 86-91]. However, most descriptions are specific to a single specific input stimulus, typically a single pulse with an eye lash or a metal pick, and specific behaviors. This leaves unexplored space of the stimuli and outputs, leading to descriptions that are potentially biased toward a specific stimulus, and not allowing for the generalizable prediction of the system.

To map the transformations between mechanoreceptor neurons and behavioral outputs, we sought to model these transformations in an unbiased quantitative framework that captures the systems' dynamics in a predictive manner. This is computationally challenging because of the stochasticity and complexity of the animal's behavioral

repertoire, as well as the various time scales and frequencies relevant in the system [92-94]. A successful technique for characterizing neuronal systems is the use of reverse correlation analysis with a white noise stimulus [5, 95-101]. This methodology is commonly applied in sensory physiology to model a sensory neuron's response to natural stimuli as a linear filter. The computed linear filters provide a complete description of the linear dynamics of the neuron, and can be used in conjunction with a nonlinear filter to accurately model its function [102-106]. This technique has also been extended to modeling sensory neurons [107] and behavior in invertebrates [108-112]. However, this technique has not been extended to model and contrast the spatial and temporal properties of behavioral responses to the gentle and harsh touch mechanosensory neurons.

Although reverse correlation analysis allows for accurate estimations of system dynamics, several experimental obstacles hinder its applicability to the mechanosensory circuits in *C. elegans* at present. Current techniques for delivering precise mechanical stimuli to animals involve the delivery of a mechanical force via a stylus or microfluidic device to specific locations on the animal's body [81, 91, 113, 114]. Although ideal for neuronal imaging, these techniques require the immobilization of animals with glue or other techniques, and therefore, do not allow for reverse correlation analysis with behavior response dynamics. Additionally, many of these techniques have a low experimental throughput, and cannot provide the large sample sizes required for reverse correlation studies. One technique that overcomes these challenges is the use of optogenetics, as a light stimulus is more easily controlled, and can be used to activate specific neurons in freely moving animals [51, 110-112]. This fictive stimulus has the added benefit of bypassing differences in receptor protein expressions, allowing for comparison between sensory

systems. In order to apply light stimuli with spatial resolution to activate specific regions of sensory neurons, we adapted a previously developed tracking platform with selective illumination [49]. The custom microscopy system uses a projector and computer vision tools to track the animal, allowing for the delivery of spatially and temporally resolved stimuli required for white noise signal delivery.

Combining these tools, we developed an experimental and computational pipeline for performing white noise analysis on *C. elegans*, and apply this method to elucidate models of transformations between mechanosensory neuron activity and behavioral response. Using our platform, we computed linear filters that characterize the dynamics of the gentle touch sensing TRNs and harsh touch sensing PVDs. These filters provide a quantitative framework for the functions of these neurons, and allowed for the investigation of differences in spatial encoding. Furthermore, this method allowed us to create models that accurately predict behavioral changes in response to mechanosensory neuron activity. Our method provides simple transformations that quantitatively characterize these systems by capturing the spatiotemporal dynamics of behaviors induced by optogenetic activation of sensory neurons.

3.2 Methods and Materials

3.2.1 Strain Maintenance

We used transgenic worms expressing channelrhodopsin in various mechanosensory neurons. Worm populations were cultured at 20C in the dark on standard nematode growth medium (NGM) petri dishes. Plates were coated with OP50 bacteria lawn supplemented with the cofactor required for channelrhodopsin, all-trans¬-retinal (Sigma-

Aldrich). The solution was prepared by diluting a 50mM stock solution (in ethanol) in OP50 suspension to a final concentration of 100uM. Control animals were grown in parallel on OP50 without all-trans¬-retinal. All worms tested were F1 progeny of P0 adults picked onto seeded plates 3-4 days before experiments. Animals were washed to unseeded NGM plates 1hr prior to assays. Animals were then picked to individual plates for experiments. Each animal was exposed to a single stimulus profile and then discarded. The strains used in this work included AQ2334: lite-1(ce314); ljIs123[pmec-4::ChR2; punc-122::rfp] [51] and ZX899: lite-1(ce314); ljIs123[pmec-4::ChR2; punc-122::rfp][90].

3.2.2 Tracking and Light Delivery Platform

Experiments were performed on a tracking system adapted from a previously developed projector based microscopy system[49]. The system uses an inverted microscope (Leica-DMIRB) with a low-magnification objective (x4) to image freely moving animals. We image using near-infrared light by applying a long-pass filter (715nm) to the transmitted light path and capture images using a large sensor NIR camera (Basler acA2040-180kmNIR), which limits interference in blue light used for optogenetics stimulus. A three-color LCD projector is used as the light source for optogenetic stimulus with selective illumination. We use a camera with large sensor area to capture the full body of the animal, and use a small ROI and binning to reduce the size of images to improve processing speed and therefore tracking rate. A Lenovo desktop computer with an Intel Core i7¬4790 Processor (8MB Cache, up to 4.0GHz) and a 512GB Solid State Drive and 16GB RAM was used to process images for tracking and selective illumination. Tracking of individual animals was performed by using images taken with the camera, and processed to compute the centroid of the animal in terms of x-y pixels on the camera FOV. Based on

the position of the computed centroid, a command is sent to a motorized stage to move the animal to the center of the FOV. To apply a light stimulus with spatial and temporal control, we used a modified projector as the light source to the microscope. Images taken with the camera are processed to determine the outline of the animal's body in each frame. The appropriate illumination pattern is then computed and sent to the projector. This process was performed at a rate of 13 frames per second. For each animal, illumination profile and tracking videos were saved for future analysis.

3.2.3 Quantitative Behavior Analysis

To extract quantitative behavioral features from tracking recordings, a custom MATLAB script was developed. A series of segmentation and morphological processes were used to extract body postures in each frame. We combined extracted postures with recorded stage movements to quantify several behaviors. We computed various "continuous" behaviors that have a scalar value for each time point. This includes velocity (magnitude), velocity (angle), acceleration, head angle, angular velocity. We also classified various "discrete" behaviors that have been used in previous works [49, 94, 115]. These include behaviors such as pauses, reversals, omega turns, and turns. Each of these behaviors were classified by applying thresholds on quantified continuous behaviors. Pauses and reversals were classified by applying both vertical and horizontal thresholds on velocity measurements. Omega turns were classified by applying a threshold on the eccentricity of the animal's posture. Curves were classified by applying a threshold on the angle of position trajectory.

3.2.4 White Noise Experiments

We used the selective illumination capability of the tracking system to deliver spatially controlled light stimuli to freely moving animals expressing ChR2 in their mechanosensory neurons. We used a pseudorandom m-sequence, a binary signal with unbiased spectrum, with similar properties to a Gaussian white noise signal [97, 107]. We tested several white noise signals, and found that an m-sequence with a maximum frequency of 2Hz produced reliable results, as it allows for testing time scales appropriate for behavioral responses. We use a light intensity of 0.75mW/mm2 as it induces reliable and varying behavioral responses [49]. The generated pseudorandom sequences were repeats of a 6-bit words, 63 value length m-sequences ($(26\text{-}1)^2 = 126$ values). We applied the same pseudorandom signal for each experimental group, applying the signal through the tracking system and changing values in the m-sequence at 2Hz, which is lower than the Nyquist Frequency (acquisition rate is 13Hz).

3.2.5 Reverse Correlation Analysis

To compute mathematical functions that describe the transformations from sensory neuronal activity into behavior, we first modeled the entire animal as a linear transducer:

$$o(t) = h(t) * s(t) = \int_{-\infty}^{\infty} h(\tau)s(t-\tau)d\tau \quad (1)$$

Where the relationship between the input signal (neuronal activity through optogenetics) s(t) and output signal (behavior) o(t) is characterized by a function h(t). We assume that the system is causal, and $h(t)<0$ for $t<0$. We used standard reverse-correlation similar to [105, 106, 109-112]29,30,33–35, and computed h(t) for specific behaviors by computing a "behavior-weighted-average" (BWA):

$$h(t) \sim BWA = \frac{1}{N}\sum_{\tau} \overrightarrow{s_{\tau-t}} \times v_o(\tau) \quad (2)$$

Where the stimulus preceding each time-point is weighed by the scalar value of the behavior at that time. We convert the input stimulus patterns of -1 and 1 to light stimulus patterns of when the light is on and off, respectively. For continuous behaviors, we used the scalar values at each time points as the weights. For discrete behaviors, we used a binary signal indicating transitions from forward movement to specific states. For all cases, we compute linear filters using 400 points preceding and following each time point (801 total timepoints). The points preceding each time point are computed as a control.

3.2.6 Statistical Significance of Computed Filters

Behavior-weighted averages (BWAs) were tested for significance by comparing their magnitude, computed as the L2 norm, to a distribution of random filters computed with shuffled data. We tested four different methods of shuffling data: cyclic shuffling of the stimulus vector by a random integer, cyclic shuffling of the output vector by a random integer, random permutations of the stimulus vector, and random permutations of the output vector. For each test, we perform the same computation with the shuffled data and repeat 100 times. The BWA is classified as significant if its magnitude is higher than all shuffled data tests. Random integers were generated from a uniform distribution from 1 to length of vector using the MATLAB function rand, and random permutations of vectors were performed using the MATLAB function randperm.

3.2.7 Nonlinear Filters and Model Predictions

We model static nonlinear filters for each behavioral response in order to extract the nonlinear dynamics not captured in the linear filters computed from reverse correlation 49. We first compute linear model predictions by convolving the computed linear filters from presented stimuli in each trial used, as shown in equation (1). We then compare these linear predictions to the measured outputs at each time point, and fit a quadratic function. These quadratic functions are then used as static nonlinear filters in a linear-nonlinear (LN) cascade model for specific behavior transformations.

$$y_{pN}(\mathrm{t}) = F_N(y_{pL}) \tag{3}$$

Where the predicted nonlinear output is a static function of the predicted linear output. We also apply an exponential decay filter (LNE) to capture nonlinear adaptations to the stimuli.

$$y_{pE}(t) = y_{pN}(t)\exp(-\lambda t) \tag{4}$$

3.2.8 Statistics

Linear filters are presented as mean ± SEM as computed by the BWA. The two-tailed Student's t-test was used to compare filter peaks between two groups. Peaks were determined by searching for local maxima in the filters between $-1 < t < 1$. $P<0.005$ was considered statistically significant. Accuracy of best-fit nonlinear filters were computed as coefficients of determination (R^2 values). Performance of models were compared using the sum of squared error (SSE). Values are normalized to the SSE value for linear models.

3.3 Results

3.3.1 Reverse-correlation analysis using optogenetics and behavior tracking

To illuminate the differences between the mechanosensory systems, we characterize and compare the dynamics for these two anatomically distinct sets of mechanosensory neurons: the gentle touch sensing TRNs and the harsh touch sensing PVDs (Figure 3.1A). In order to use reverse correlation for modeling behavioral responses, the two main experimental requirements are the delivery of a white noise stimulus and accurate measurements of the output. For the stimulus, we used optogenetics to directly activate the mechanosensory neurons with a white noise signal. This unmediated input enabled us to activate neurons regardless of expression of mechanotransductive channels. This allows the comparison of how the two systems and their morphologies control downstream activity, rather than differences in their sensory activation. Additionally, whereas a natural stimulus can activate additional sensory neurons and possibly interfere with the characterization, the optogenetic stimulus will only activate the neurons expressing channelrhodopsin. Therefore, the resulting filters characterize the dynamics of behaviors exclusively in response to activation of specific sensory neurons. Our tracking platform enables the delivery of patterned illumination while simultaneously tracking individual animals, allowing for selective activation of specific sections of transgenic animals with high spatial and temporal precision (Figure 3.1B, Methods). We used this platform to deliver the white noise light stimulus for reverse correlation; we activate mechanosensory neurons with a pseudo-random m-sequence pattern, a spectrally unbiased binary signal (Methods).

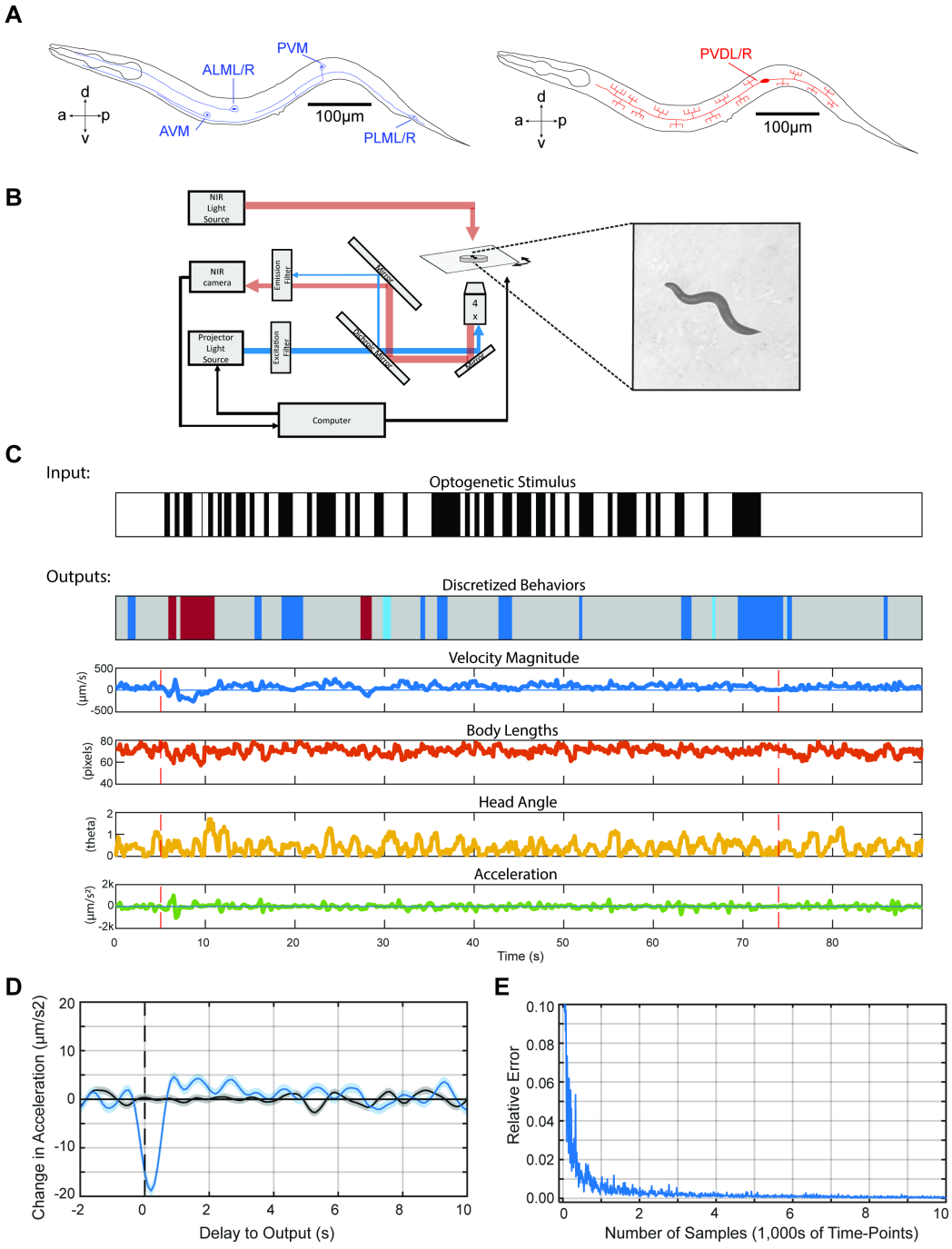

Figure 3.1 Reverse correlation analysis of mechanosensory neurons enabled by tracking and selective illumination platform. (A) Mechanosensory neurons characterized in this study. The gentle touch sensing neurons ALML/R, AVM, PVM, and PLML/R (blue) and harsh touch sensing neurons PVDL/R (red). (B) Schematic of custom tracking system with selective illumination used for reverse correlation experiments (Methods). A projector is used as the light source to enable selective illumination. Captured video frames are processed in real-time to deliver accurate

light patterns on moving animals. (C) Sample stimulus and extracted quantified behavior traces obtained from the custom platform and analysis script (Methods). Input is a binary signal of On and Off. Outputs are characterized for both "discrete" and "continuous" behaviors. Discretized behaviors are classified based on a custom behavior analysis script (Methods). Colors represented in sample output: dark blue represents a pause, red represent reversals, light blue represents turns. (D) A sample filter computed using the BWA computation (Acceleration Response to Anterior TRN, n = 88,031 time-points). (E) The speed of convergence for the BWA as a function of the amount of data used to train the model. The error converges to a relative tolerance of $\delta<0.005$ after 30,000 time-points.

The outputs we seek to characterize are the behavioral responses of animals using the optogenetic stimuli as inputs. We developed a custom computer vision algorithm (Methods) to analyze recordings of animals' behavior in a high-throughput and unbiased manner. The worm's posture and position are extracted for each frame, which are then used to quantify various "continuous" behaviors such as instantaneous velocity, instantaneous head angle, and instantaneous acceleration (Figure 3.1C). In addition to these "continuous" behaviors we also quantified and categorized several classical "discrete" behaviors such as reversals, pauses, and omega turns 18,40–42 (Figure 3.1C, Methods). Each of these continuous and discrete variables was used as a separate output for reverse correlation analysis, yielding a filter for arbitrary stimulus patterns. By using filters for a large portion of the worm's behavioral repertoire, we can describe the overall behavioral response when stimulating specific mechanosensory neurons.

Using the white noise light stimulus for optogenetics and the quantified behavioral responses, we next apply reverse correlation to model *C. elegans* response as transformations of linear and non-linear filters. Classically, when characterizing mammalian neuronal systems, a neuron's response is modeled by computing the average of the stimuli that preceded its action potentials (spike-triggered average or STA) or its

subthreshold voltages (voltage-weighted average or VWA) [105]. Analogously, we estimate the dynamics of *C. elegans* response by computing the behavior weighted average of the stimulus (BWA). When stimulating specific segments of the mechanosensory systems, the BWA represents how the animals characteristically transform patterns of activity of those neurons into specific behaviors, providing a filter estimation of this transformation (Figure 3.1D).

In order to accurately estimate these linear filters, a large sample size is required to test enough input values [95, 106]. To identify the number of samples required in our system, we characterized the speed of convergence of computed filters as the number of input samples increased. We characterized the convergence of filters by computing the L2 norm of the difference between subsequent filters (computed as the absolute difference between filters). We found that our system converges (to a relative tolerance of $\delta<0.005$) after using roughly 30,000 frames of tracking data (Figure 3.1E). With our experimental conditions, this is equivalent to a sample size of roughly 30 animals (Methods).

3.3.2 Linear Filters for anterior and posterior touch receptor neurons (TRNs) robustly capture behavioural dynamics

We first used our method to characterize responses to the touch receptor neurons (TRNs: ALML/R, AVM, PVM, and PLML/R) by using transgenic animals expressing channelrhodopsin (ChR2) under the mec-4 promotor (Methods). In response to natural stimuli, the posterior TRNs (PVM and PLML/R) respond to posterior touch, inducing forward acceleration, whereas the anterior TRNs (ALML/R and AVM) respond to anterior touch, inducing reversals [2, 6, 49, 85, 116]. To characterize the dynamics of these

responses, we applied an m-sequence light stimulus to either the anterior or posterior region of transgenic animals, selectively stimulating the anterior or posterior TRNs, respectively (Figure 3.2A). We first computed linear filters characterizing the relationship between anterior TRNs and either discrete or continuous behavior (Figure 3.2 and Figure B. 1). As a control, we also performed experiments with animals that were not fed all trans-retinol (ATR), a cofactor required for ChR2 function. The computed filters for control animals are flat, zero-mean signals (Figure 3.2, gray lines). In contrast, the acceleration BWA for the ATR-fed worms results in a filter with a robust negative peak, -13 ± 0.50 μm/s2 (Figure 3.2Ei). The presence of this peak in the experimental group and its absence in the control group suggest that the filter is optogenetically induced, and not due to spontaneous behavior. We attribute small fluctuations as experimental noise rather than representing a true high frequency response. Lastly, this deceleration in the experimental group is expected from typical reversal responses to anterior touch stimulation [2, 6].

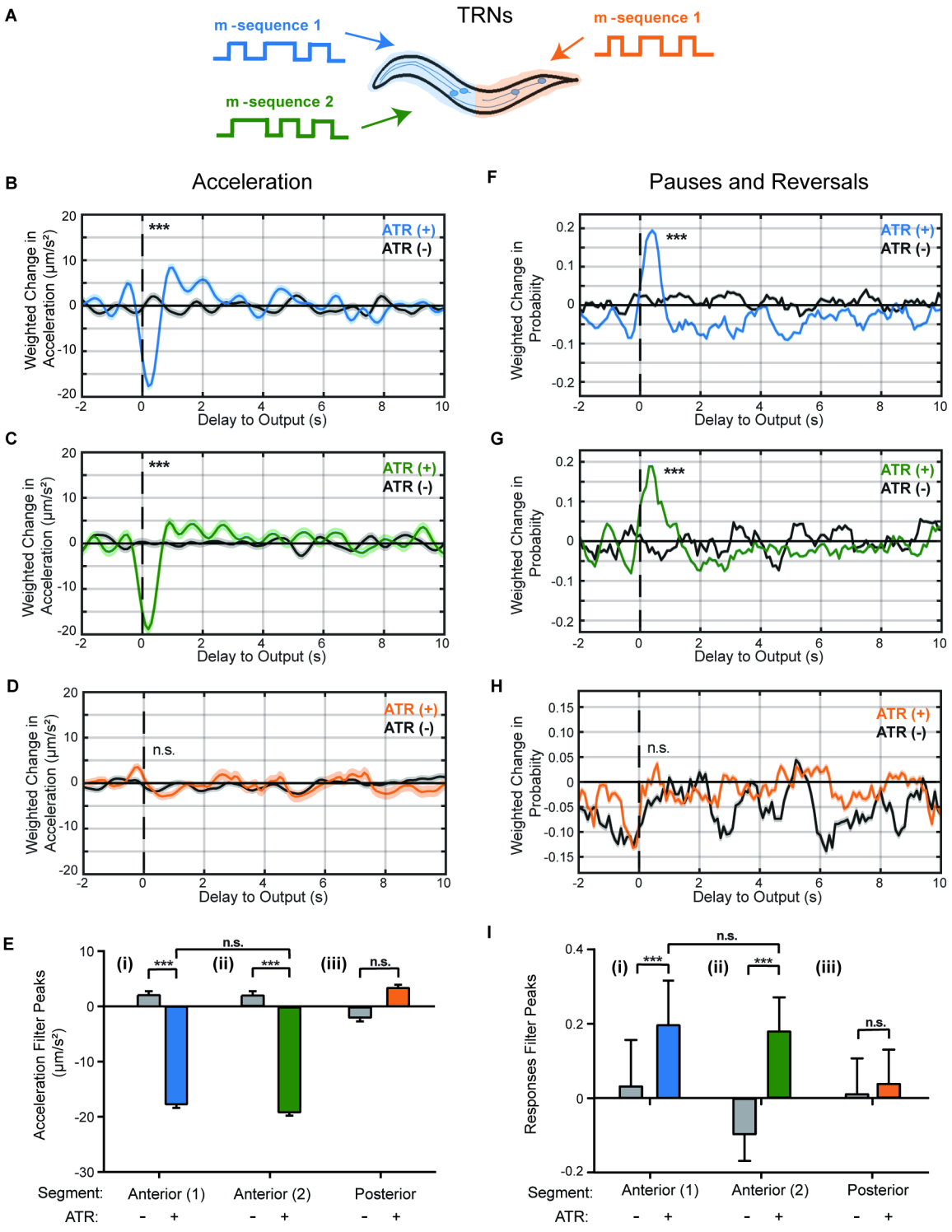

Figure 3.2 Linear filters for the touch receptor neurons (TRNs) responses are robust and reproducible. (A) Schematic of stimulus patterns and TRNs analyzed. Animals used in these experiments express channelrhodopsin using the mec-4 promoter (Methods). (B-D) Linear filters computed for acceleration when stimulating the

anterior (B,C) and the posterior (D) TRNs with an m-sequence. Colored plots represent filters computed from ATR-fed animals, gray plots represent filters computed from control (not ATR-fed) animals. Dark line and light shade represent BWA and SEM, respectively (n values listed in Table S1). (E) Comparisons of peak values from computed linear filters in B-D. Error bars indicate SEM. Statistical significance computed using student's t-test (*p<0.001). (F-H) Linear filters computed for pauses and reversals when stimulating the anterior (F,G) and the posterior (H) TRNs with an m-sequence. Colored plots represent filters computed from ATR-fed animals, black plots represent filters computed from control (not ATR-fed) animals. Dark line and light shade represent BWA and SEM, respectively (n values listed in Table S1). (I) Comparisons of peak values from computed linear filters in F-H. Error bars indicate SEM (n values listed in Table S1). Statistical significance computed using student's t-test (***p<0.001).**

In order to further assess the validity of the resulting filters, we performed statistical tests comparing true filters and filters computed from shuffled data (Methods). We compute magnitudes for all filters, defined as the L2 norm, to the correctly computed filter. Data is shuffled in four different ways (Methods). In all tests, the BWA computed from experimental data has the highest magnitude compared to filters computed from shuffled data (Figure 3.3). Together with the statistical comparison of ATR-fed and non ATR-fed animals, we conclude that the BWA for acceleration is robust and descriptive of the behavioral response.

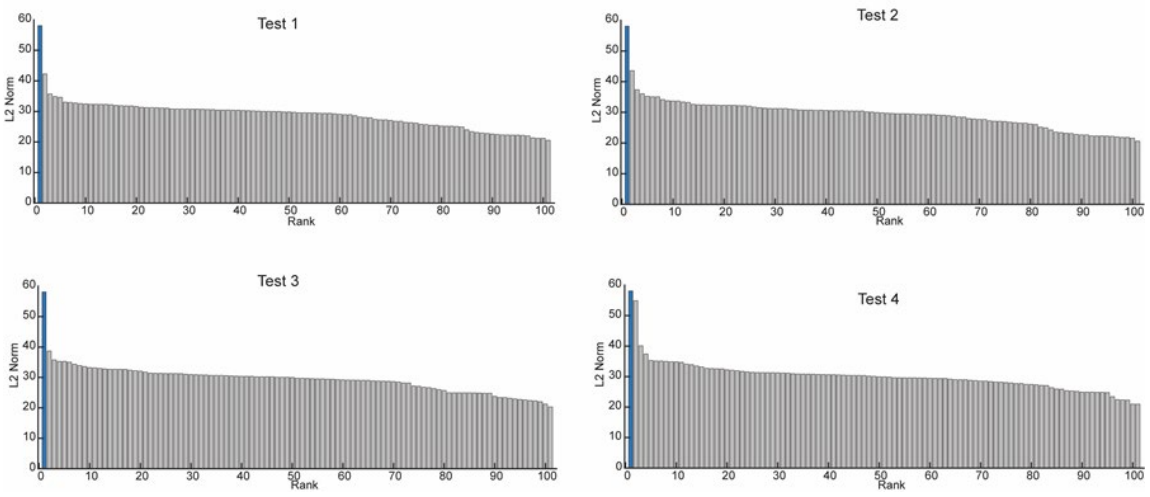

Figure 3.3 Comparison of shuffled data significance tests. Results from comparison of four methods of shuffling data for statistical significance tests of linear filters. (A) Cyclic shuffling of stimulus vector by a random integer. (B) Cyclic shuffling of behavior vector by a random integer. (C) Random permutation of stimulus vector. (D) Random permutation of behavior vector. Bar plots represent the magnitude of filters, computed as the L2 norm, and are plotted in ranked order from highest to lowest magnitude. Colored bar represents appropriately computed filter, gray bars represent filters computers with shuffled data.

In addition, our method also reveals new information about the dynamics of these responses. From the BWA, we can characterize metrics such as the delay to the peak (0.2s) and the decay timescale of the filter (0.4s); these temporal characteristics are critical for accurately predicting response to activation of the anterior TRNs. In comparison, the BWA computed with velocity also returns a linear filter with a negative peak (-6.1 ± 0.39 μm/s), although with a longer delay to peak (0.7s) and longer decay timescale (0.6s) (Figure B. 1). The difference between temporal characteristics of these two filters suggests that although animals reverse for a relatively long time after the stimulus (1.3s), the deceleration portion of this reversal only takes place in the first 0.6s after a stimulus.

To ensure that the computed linear filters are not an artifact from the input signal itself, we tested a different m-sequence stimulus. When computing the BWA for acceleration in these trials, we observe a similar linear filter to those obtained with the previous stimulus (Figure 3.2C, as compared to Figure 3.2B). This filter is also statistically significant when compared to shuffled data (Figure 3.4). When comparing the peak values of the filters computed with different stimuli, there is no statistical difference (Figure 3.2Eii). These results demonstrate that the linear filters are indeed characteristic of *C. elegans*' behavioral output specifically in response to the activity in the anterior TRNs.

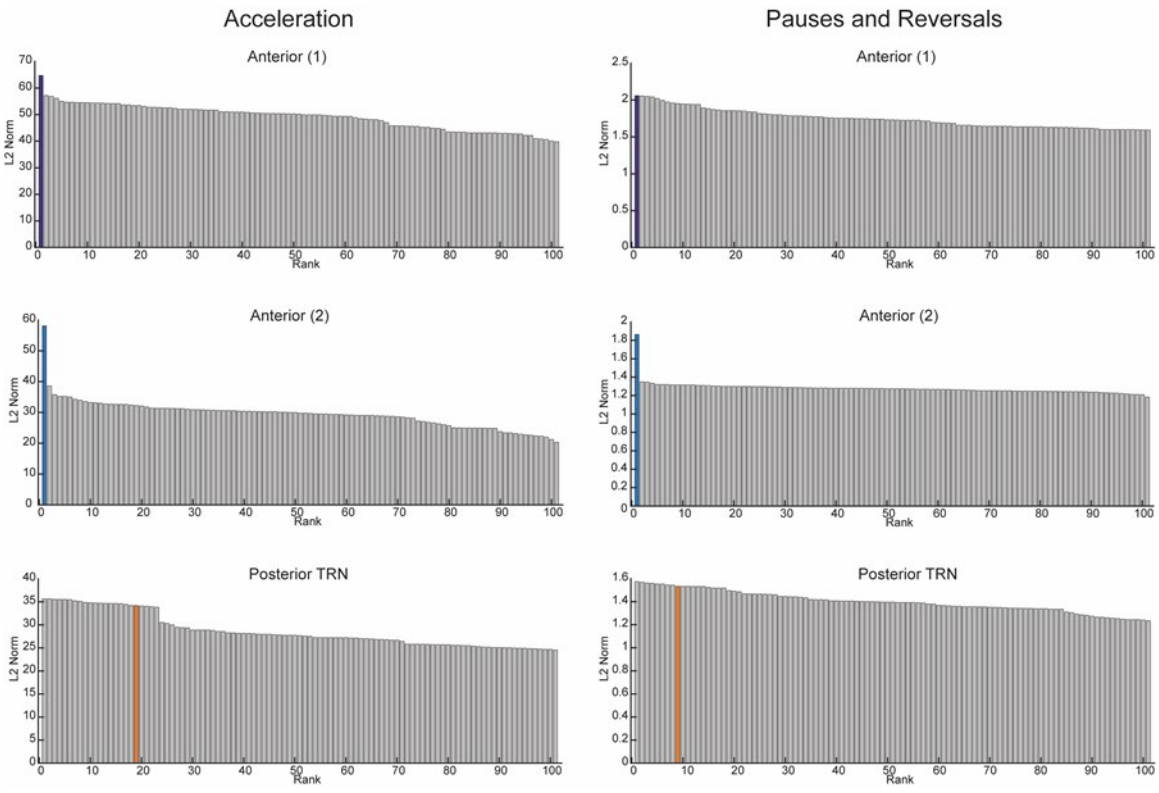

Figure 3.4 Significance test results for linear filters for TRNs. Results from shuffled data significance tests for linear filters computed for activation of TRNs in Figure 2. (A-C) Significance test results for computed filters for acceleration for anterior TRNs (A,B) and posterior TRNs (C). (D-F) Significance test results for computed filters for pauses and reversals for anterior TRNs (D,E) and posterior TRNs (F). Bar plots represent the magnitude of filters, computed as the L2 norm, and are plotted in

ranked order from highest to lowest magnitude. Colored bar represents appropriately computed filter, gray bars represent filters computers with shuffled data.

Next, we sought to compare the dynamics of the animals' response between anterior or posterior TRN activities. Previous findings have shown that applying a mechanical force to the posterior region of the animal induces an acceleration, and PLM is required for these responses [2, 6, 117]. As with the anterior TRNs, we stimulated the posterior TRNs by applying an m-sequence light stimulus to the posterior half of the animal, and computed the BWA for the same quantified behaviors (Figure 3.2 and Figure B. 1). The filter for acceleration has a positive peak (2.8 ± 0.48 μm/s2), although with a much smaller magnitude than its anterior counterpart and is not statistically significant compared to non ATR-fed worms (Figure 3.2D). Additionally, the filter is not statistically significant when testing against filters for shuffled data (Figure 3.4). Interestingly, although the computed linear filter for the posterior TRNs has a peak in the direction that is consistent with previous findings, it is close to zero-mean. One interpretation that is consistent with literature is that worms have a lower rate of responses when activating PLM and PVM in comparison to the activating anterior TRNs. This is not surprising, as worms are generally moving forward and do not require a change in behavior to escape the weak stimulus, whereas avoidance of a weak anterior stimulus requires a directional change.

In addition to continuous signals, we also estimated linear filters for the probability of transitions between defined states. Unlike in predicting continuous variables (e.g. acceleration and velocity), filters computed for these behaviors indicate a change in probability of transitions to these behaviors. When computing the BWA with transitions into pauses or reversals in response to anterior TRNs, we observe linear filters with positive

peaks that are statistically significant as compared to non ATR-fed animals (Figure 3.2F,G, I). Similarly, the filters computed from shuffled data support this statistical significance (Figure 3.4). This indicates that activating the TRNs induce an increase in probability of transitions to pauses or reversals, and this increased likelihood happens within the first second after a stimulus. In contrast, when stimulating the posterior TRNs, the filter computed for transitions into pauses and reversals is close to zero-mean, indicating that the stimulus does not alter these behaviors significantly (Figure 3.2H,I, and Figure 3.4).

3.3.3 Reverse Correlation Analysis of Harsh-Touch Sensing PVD Neurons

In addition to the TRNs, *C. elegans* has another set of neurons that are responsible for body touch sensation. The PVD neurons are morphologically unique sensory neurons that have extensive and organized dendritic structures expanding most of the body of the worm; in contrast, TRNs are tiled (Figure 3.1A). Additionally, the PVD neurons are known to respond to harsh touch, as opposed to gentle touch or nose touch [84, 87-90]. Because of the morphological and functional differences between the PVD and TRN systems, we ask whether there are also downstream differences in spatial and temporal behavioral response dynamics. To do so, we applied the reverse correlation method to animals expressing ChR2 in the PVD neurons.

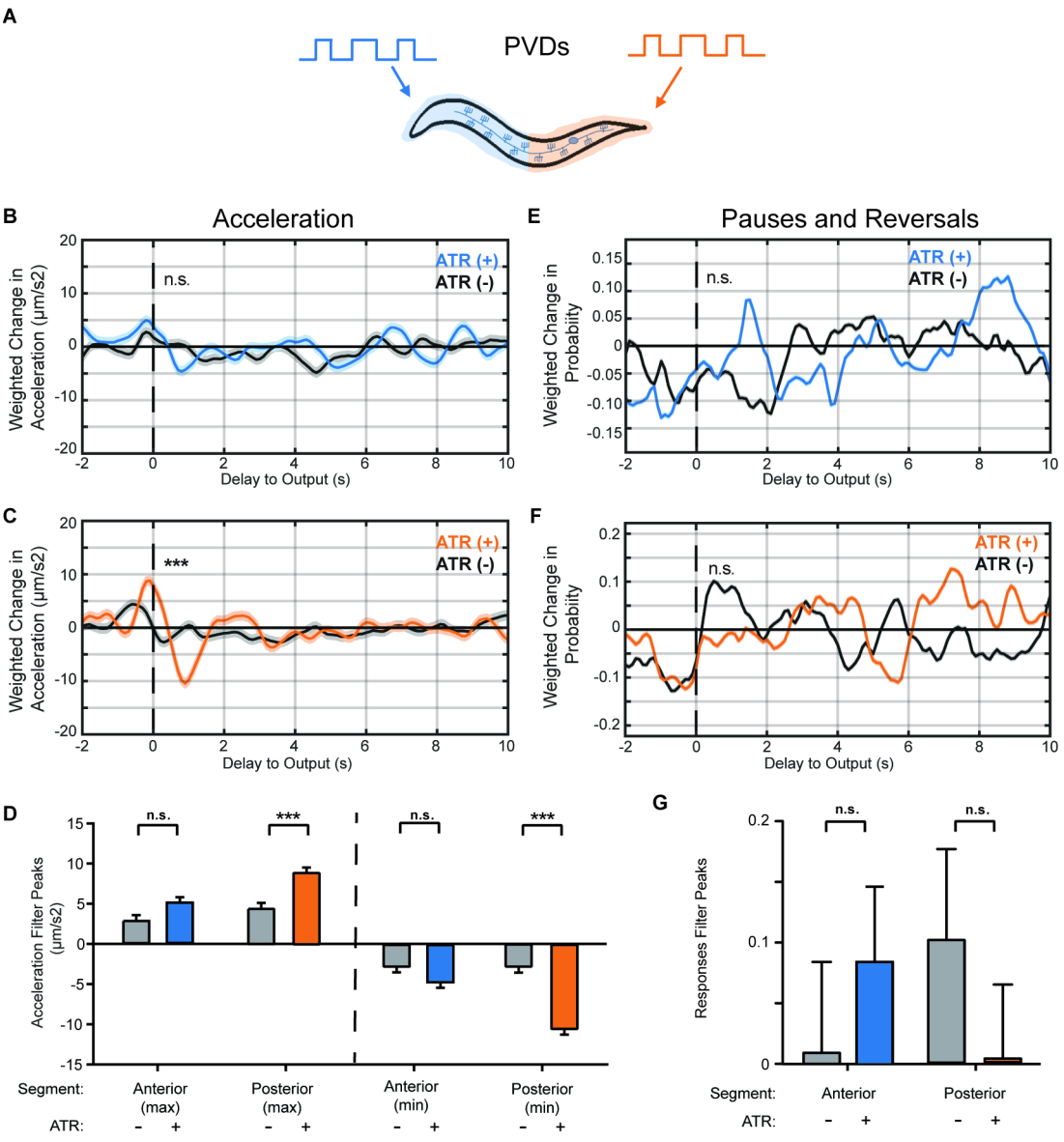

Figure 3.5 Linear filters for PVD activity illuminate dynamic differences between gentle and harsh touch systems. (A) Schematic of stimulation patterns and segments of PVD being characterized. (B,C) Linear filters computed for acceleration when stimulating the anterior (B) and posterior (C) regions. Colored plots represent filters computed from ATR-fed animals, black plots represent filters computed from control (not ATR-fed) animals. Dark line and light shade represent BWA and SEM, respectively (n values listed in Table S1). (D) Comparisons of peak values from computed filters. Error bars indicate SEM (n values listed in Table S1). (E,F) Linear filters computed for pauses and reversals when stimulating the anterior (E) and posterior (F) regions. Colored plots represent filters computed from ATR-fed animals, black plots represent filters computed from control (not ATR-fed) animals. Dark line and light shade represent BWA and SEM, respectively (n values listed in

Table S1). (G) Comparisons of peak values from computed filters. Error bars indicate SEM (n values listed in Table S1).

For comparison with the TRNs, we again divided the stimulus regions into anterior and posterior segments, and computed the BWA and estimated linear filters for the same behaviors (Figure 3.5A). Interestingly, when the animal is stimulated either anteriorly or posteriorly, the BWA for acceleration have positive peaks (Figure 3.5B,C), indicating that activating either of these segments of PVD induces an increase in velocity. This positive peak is also observed for both segments when computing the BWA with velocity (Figure B. 2). However, only the filters from the posterior segment are statistically different from the non-ATR group, with a higher positive peak for both acceleration (4.0 ± 0.58 μm/s2 vs 7.1 ± 0.58 μm/s2) and velocity (3.5 ± 0.32 μm/s vs 7.1 ± 0.32 μm/s) (Figure 3.5D and Figure B. 2). When computing the BWA with transitions into pauses or reversals in response to either anterior or posterior PVD, we observe flat, zero-mean linear filters (Figure 3.5E, F). The filters are statistically indistinguishable from the non-ATR fed control group (Figure 3.5G), indicating that activation of the PVDs do not induce a change in probability of these events. When comparing these filters with shuffled data, only the posterior acceleration filter is statistically significant (Figure 3.6). This contrast from the TRN filters suggests a different role for PVD sensory neurons in the behavioral circuit – that PVD activation promotes positive acceleration, and TRNs promote negative acceleration, consistent with previous findings [85, 89].

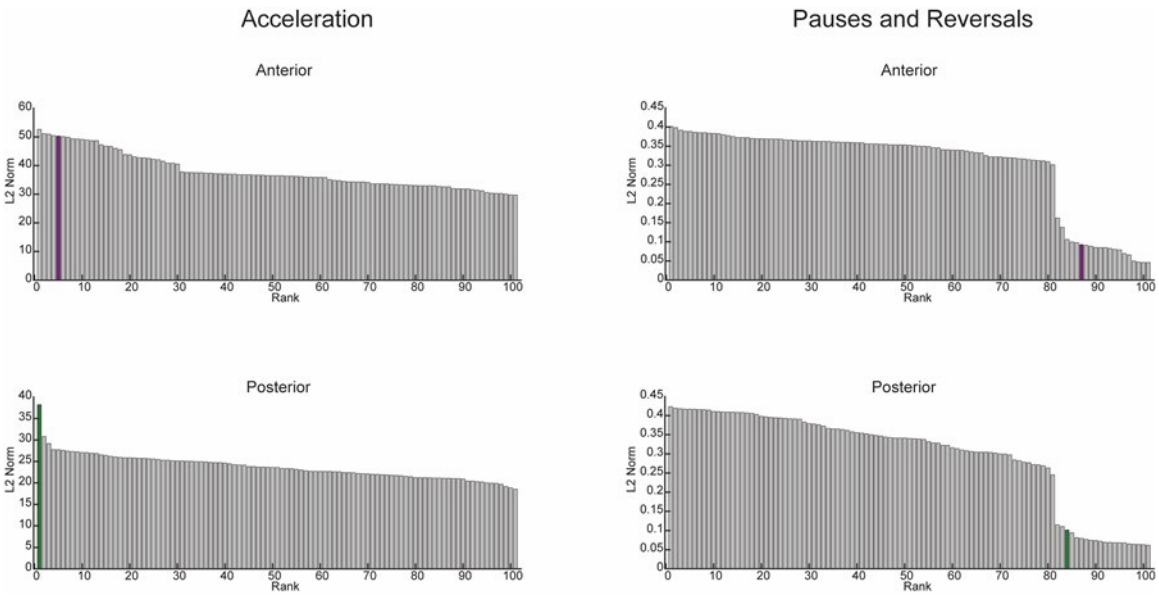

Figure 3.6 Significance test results for linear filters for PVD. Results from shuffled data significance tests for linear filters computed for activation of PVD in Figure 3. (A,B) Significance test results for computed filters for acceleration for anterior (A) and posterior (B) segments of PVD. (C,D) Significance test results for computed filters for pauses and reversals for anterior (C) and posterior (D) segmentS of PVD. Bar plots represent the magnitude of filters, computed as the L2 norm, and are plotted in ranked order from highest to lowest magnitude. Colored bar represents appropriately computed filter, gray bars represent filters computers with shuffled data.

In addition to the magnitudes, the context of peak occurrence can also be informative. The PVD acceleration filters have significant negative peaks following the positive peaks; the magnitudes of the negative peaks are of similar values to the first positive peak (Figure 3.5D). This suggests that the acceleration in response to PVD activation is more likely to occur when preceded by a negative acceleration. In other words, worms that are slowing down or reversing are more likely to respond to PVD activation and produce a positive acceleration. In contrast, the anterior TRN acceleration filters only contain one significant peak. These differences in the acceleration filters further supports the idea that PVD and TRNs influence different aspects of behavior.

3.3.4 Linear-Nonlinear Models Predict Behavioral Response

In general, the filters computed from BWA in response to a white noise signal capture the linear dynamics of the analyzed systems. However, biological systems are rarely linear24. A common approach for modeling the nonlinear dynamics of a system is to use a linear-nonlinear cascade, where a static nonlinear filter is used to characterize the nonlinear dynamics not captured by reverse correlation [95, 98, 100, 118]. To define static nonlinear filters, we used the linear filters computed from BWA and compared predicted outputs with measured experimental outputs (Methods). We first compared predicted acceleration values with the quantified experimental values (Figure 3.7A, gray circles). There is a positive correlation between predicted and experimental outputs, indicating that the model does indeed capture linear dynamics in these responses. To mathematically characterize the nonlinear dynamics, we fit a static filter using a nonlinear function (Figure 3.7A blue lines, Methods). We also characterized nonlinear filters for velocity (Figure B. 3) and transitions into pauses or reversals (Figure 3.7B, Methods). The quadratic functions accurately model these relationships, suggesting that they capture a large portion of the nonlinear dynamics of the anterior TRNs. We also computed static nonlinear filters for stimulation of the posterior TRNs. In comparison to the anterior TRNs, there is a lower correlation between experimental measurements and predicted values (Figure 3.7C,D, Figure B. 3). This is expected, as the estimated linear filters for these neurons were close to zero-mean, yielding a small range of predicted responses. Furthermore, because the linear filters alone led to a low predictability of responses for posterior TRNs, nonlinear functions also fail to capture a large portion of the variability in responses (Figure 3.7C,D, Figure B. 3, orange lines).

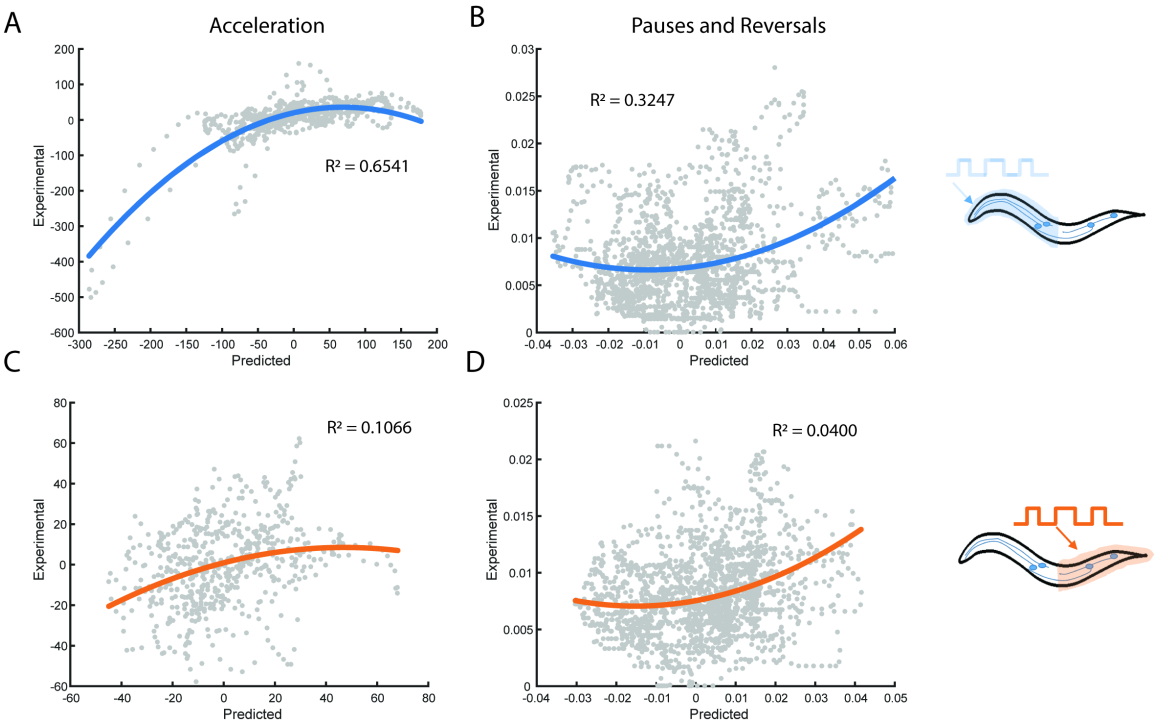

Figure 3.7 Static nonlinear filters capture nonlinear dynamics in behavioral outputs. (A,B) Static nonlinear filters fitted for predicted values from the linear filter (x-axis) against experimental values (y-axis) when stimulating the anterior TRNs, including acceleration (A) and transitions into reversals (B). (C,D) Static nonlinear filters when stimulating the posterior TRNs, including acceleration (C) and transitions into reversals (D). Linear filters and experimental values are subsets of data used in Figure 2 (n=600 for all conditions). Colored traces represent computed nonlinear filters and gray dots represent independent time-points from measured and predicted values. Probability of discrete events is computed as the probability of an event occurring at a given time point.

Using the static nonlinear filters, we sought to test the accuracy of using linear-nonlinear (LN) cascade models to predict behavioral responses to novel stimuli. To do this, we probed the anterior TRNs with a different m-sequence stimulus from the one used to compute the filters (Figure 3.8A, Methods). We first compared the velocities of animals predicted velocities when using the linear filter only (Figure 3.8B). Although the magnitude of predicted velocity from the model did not exactly match the experimental measurements, the model accurately predicts temporal dynamics of velocity in response to

this novel stimulus. Next, we incorporated the static nonlinear filter to predict velocities (Figure 3.8C). When using the LN model, the magnitudes of predicted velocities are more similar to experimental values, leading to more accurate predictions. In addition to predicting the continuous velocity of the animals, we also tested L and LN models for pauses and reversals, and observe predicted increases in probability of events similar to experimental values (Figure B. 4A,B).

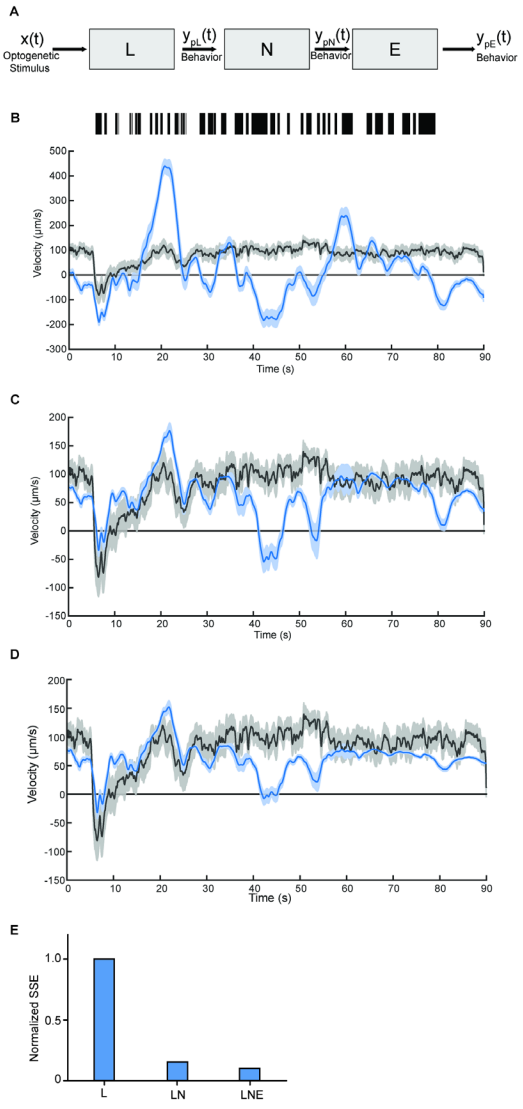

Figure 3.8 Linear-Nonlinear-Exponential (LNE) model accurately predicts behavioral response. (A) Schematic of LNE model for behavioral responses to

mechanosensory neuron activity: a LTI system modeled from BWA, followed by a static nonlinear filter and exponential decay filter. (B-D) Comparison of predictions of velocity for L (B), LN (C), and LNE (D) models (blue) and experimental traces (black). Dark line and shade represent average and SEM, respectively (n = 31 animals). (E) Comparison of performance of models, computed as the sum of squared error (SSE).

Although the LN models generally predict behavioral dynamics, a key discrepancy between model predictions and experimental measurements is the lack of adaptation to stimulus. In our experiments, we observe a time-dependent decrease in the magnitude of responses, which fails to be captured in time-scales of the dynamic linear filters. Biologically, this habituation of responses is commonly observed in sensory systems [119]. To model this decay of responses, we apply a dynamic exponential function following the LN cascade (Figure 3.8A). We tested a wide range of decay rate values using this model and found that a decay rate of 50s best provided the most accurate predictions (Figure 3.9). Interestingly, this decay rate is consistent with previous findings from investigations of habituation to stimulation of TRNs[120]. When adding this exponential component to our model, the accuracy of our model's predicted behavioral responses improve for later time points of the trials, improving the overall accuracy of our models (Figure 3.8D, Figure B. 4C,D). Our results illustrate how the linear filters computed from BWA, when combined with additional nonlinear filters, can accurately predict temporal dynamics of behavioral responses to sensory neuron activation.

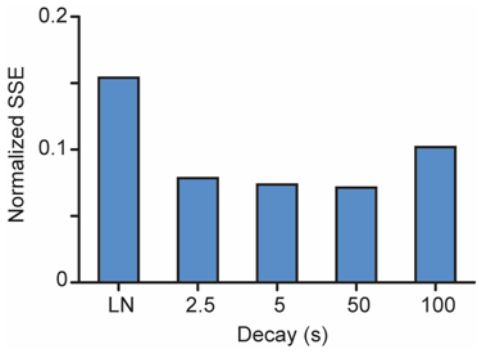

Figure 3.9 Comparison of decay factors. Comparison of model predictions of velocity for various exponential decay factors. Exponential decays of 2.5s, 5s, 50s, and 100s were tested, with 50s showing the best fit. Performance of models is computed as the sum of squared error (SSE), normalized to the linear model performance value..

3.3.5 Spatially Refined Selective Illumination Improves Resolution of Linear Filters from BWA

We have thus far characterized mechanosensory systems by probing either the anterior or posterior segments of the animal, similar to previous investigations of the receptive fields of mechanosensory systems [89, 91]. To further examine the spatial resolution of the mechanosensory systems, we took advantage of our selective-illumination light stimulus, which allows for the probing of specific spatial segments as small as 14µm [49]. We characterized the TRN system with better resolution by increasing the number of segments in our stimulus to 4 (Figure 3.10A). We applied an m-sequence stimulus selectively to one of the four segments, and computed linear filters for both continuous and discrete behavioral outputs (Figure 3.10 and Figure B. 5). This segmentation of the TRN system allows for the computation of separate filters for the processes and cell bodies of ALM and AVM, as well as separate filters for PVM and PLM cell bodies (while keeping a high number of photons in the stimulus region). We first computed filters for acceleration in response to stimulating four segments. The filters for the most anterior quarter and

second-most anterior quarter have a prominent negative peak, statistically significant when compared to non-ATR fed animals (Figure 3.10B,C,F). These filters are also statistically significant when compared to shuffled data (Figure 3.11). Interestingly, these filters are similar to the filter computed from stimulating the entire anterior region (compare to Figure 3.2B,C). This suggests that there are no observable differences in acceleration dynamics between cell body and axon activity of the anterior TRNs. Similarly, the filters for acceleration in response to the most posterior quarter and second most posterior quarter are both flat and are statistically indistinguishable from filters computed with non-ATR fed animals (Figure 3.10D,E,F). These filters are also not statistically significant when comparing to shuffle data (Figure 3.11). Similar to the anterior region, the acceleration filters for the separate posterior segments are similar to the flat filter computed from stimulating the entire posterior region (compare to Figure 3.2D).

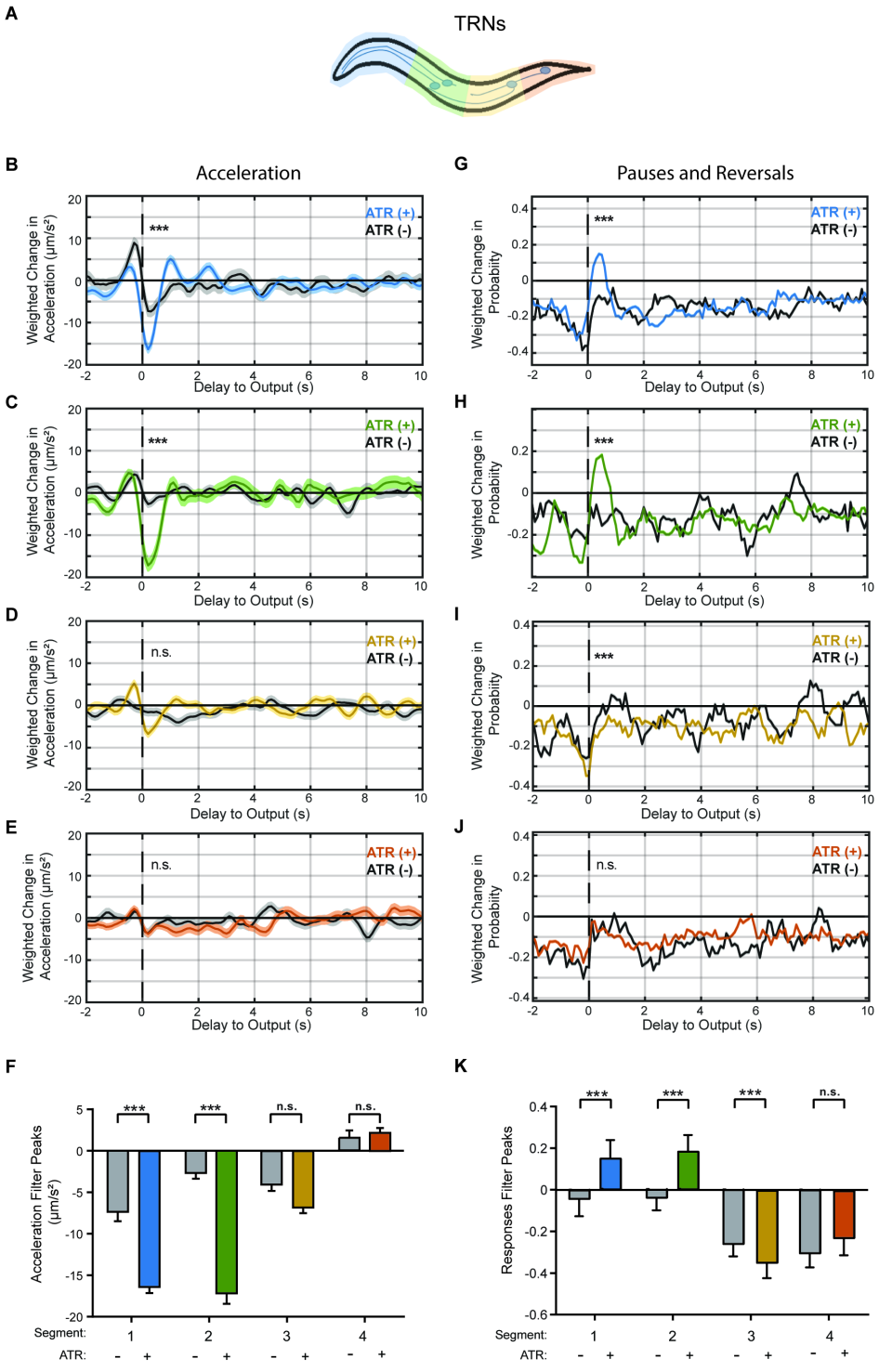

Figure 3.10 Decreasing stimulus region allows for the estimation of a spatiotemporal receptive field with higher resolution. (A) Schematic of stimulus patterns and TRNs analyzed. (B-E) Linear filters computed for acceleration when stimulating the most anterior (B), the second-most anterior quarter (C), second-most posterior quarter (D), and the most posterior quarter (E) of the TRNs with an m-sequence. Colored

plots represent filters computed from ATR-fed animals, black plots represent filters computed from control (not ATR-fed) animals. Dark line and light shade represent BWA and SEM, respectively (n values listed in Table S1). (F) Comparisons of peak values from computed filters in B-E. Error bars indicate SEM (n values listed in Table S1). (G-J) Linear filters computed for acceleration when stimulating the most anterior (G), the second-most anterior quarter (H), second-most posterior quarter (I), and the most posterior quarter (J) of the TRNs with an m-sequence. Colored plots represent filters computed from ATR-fed animals, black plots represent filters computed from control (not ATR-fed) animals. Dark line and light shade represent BWA and SEM, respectively (n values listed in Table S1). (K) Comparisons of peak values from computed filters in B-E. Error bars indicate SEM (n values listed in Table S1).

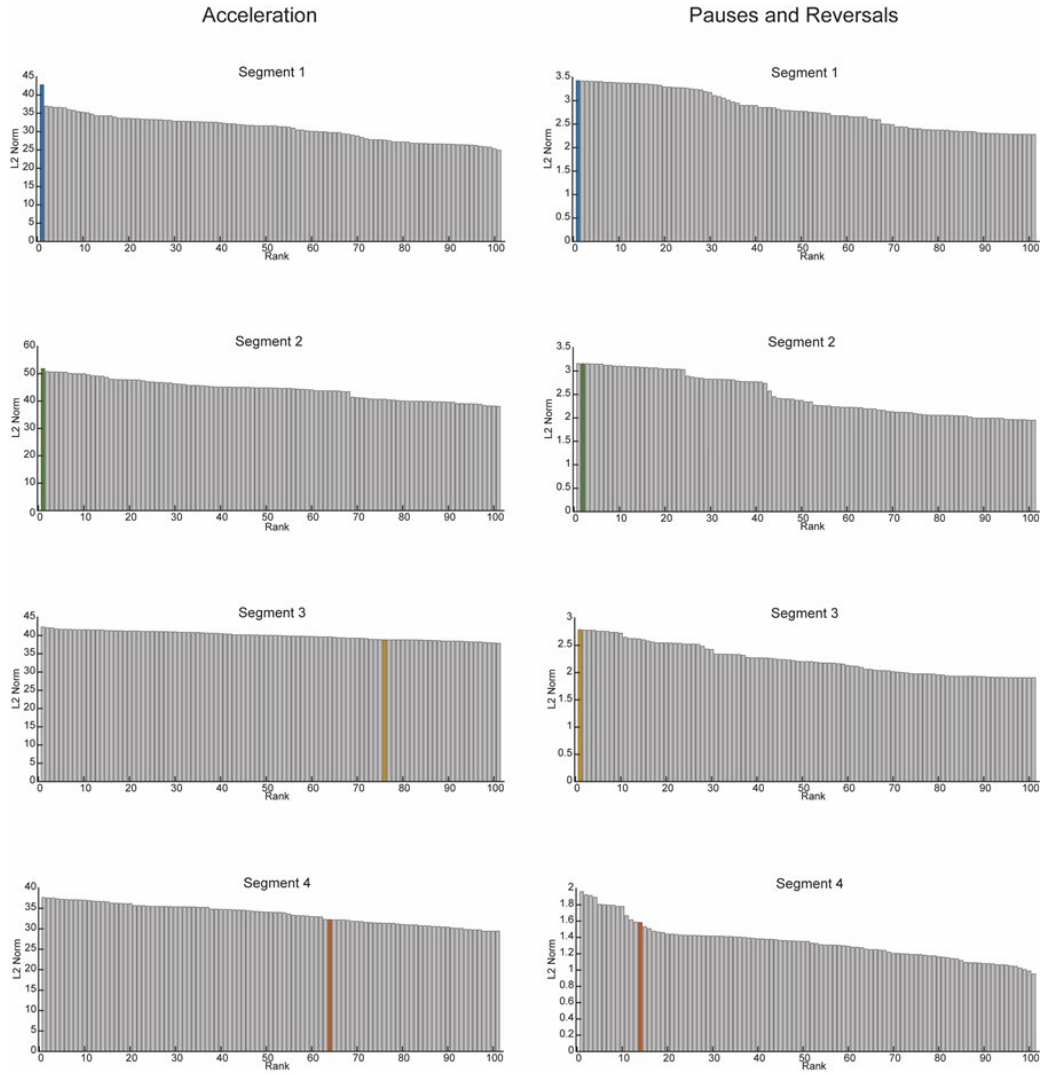

Figure 3.11 Significance test results for linear filters for refined TRN analysis. Results from shuffled data significance tests for linear filters computed for activation of TRNs

in Figure 6. (A-D) Significance test results for computed filters for acceleration for most anterior (A), second-most anterior (B), second-most posterior (C), and most posterior (D) segments of TRNs. (E-H) Significance test results for computed filters for pauses and reversals for most anterior (E), second-most anterior (F), second-most posterior (G), and most posterior (H) segments of TRNs. Bar plots represent the magnitude of filters, computed as the L2 norm, and are plotted in ranked order from highest to lowest magnitude. Colored bar represents appropriately computed filter, gray bars represent filters computers with shuffled data.

In contrast to the acceleration filters, when computing linear filters with transitions into pauses or reversals, we find differences in spatial encoding. The results for the anterior segments were similar to acceleration, with the resulting filters for the most anterior quarter and second-most anterior quarter being statistically significant (Figure 3.11) and having positive peaks similar to the filter computed when stimulating the entire anterior regions (compare Figure 3.10G,H,K to Figure 3.2F,H,I). This suggests that there is low spatial encoding of activity in the anterior TRNs. In contrast with the anterior region, dividing the posterior segment of the TRNs separates the cell bodies of PVM and PLM is different filters. The filter for the most posterior quarter was again very similar to the flat filter computed when stimulating the entire posterior region (Figure 3.10J and Figure B. 5). Interestingly, the filter for second-most posterior quarter is statistically significant (Figure 3.11) and has a negative peak close to t=0 (Figure 3.10I,K), indicating that there is a reduced probability of pauses and reversals when activating PVM. This suggests that PVM has a previously undescribed function of inhibiting pauses and reversals. Additionally, this implies that there is spatial encoding of activity in the posterior TRNs: filters computed when activating either of the PVM or PLM cell bodies encode for different responses.

3.4 Discussion

The nervous system continuously transduces sensory stimuli into layers of neural activity and appropriate behavioral outputs. One of the biggest challenges in mapping this neuronal encoding is the lack of experimental and computational methods that provide a quantitative framework for characterizing how a layer of neural activity is transduced into the downstream circuit. In this work, we use reverse correlation analysis with a custom tracking platform to investigate the spatial and temporal encoding of two mechanosensory systems, the gentle touch sensing TRNs and the harsh touch sensing PVDs. We computed several linear filters that quantitatively describe transformations between sensory neuron activity and behavioral outputs, and support previous findings about the systems. Analysis of the PVDs produced linear filters that indicate an increase in velocity and acceleration from their activation, which is consistent with literature on its function [84, 87, 89, 90, 121]. Similarly, the linear filters computed for the TRNs were also consistent with previous literature, as the anterior TRNs show decreases in velocity and acceleration, and an increase in probability of pauses and reversals [2, 6, 42, 51, 85], and the posterior TRNs show an increase in acceleration [2, 6, 85]. It should be noted that we do not measure expression levels of ChR2 in the sensory systems, and any differences in computed filters could be explained by differences in expression levels. However, when assuming uniform expression levels across the sensory systems, our results provide spatiotemporal receptive fields for these systems that are consistent with previous findings [6].

The linear filters resulting from our method provide several insights into the circuitry and morphological differences between the two sensory systems. First, although we used identical stimuli for both segments, the filters produced from activating the anterior TRNs were much more robust than the filters from activating the posterior TRNs,

suggesting that downstream interneurons in this circuit are more responsive to the anterior neurons. This preference in downstream activity has also been observed in experiments involving tap responses, which show that reversals dominate over accelerations when tapping cultured plates, and this preference occurs downstream of sensory neuron activity [85]. In contrast, the filters for the posterior segments of PVD were more robust than the anterior segments. This is also consistent with previous findings that show PVD is required for posterior harsh touch sensation, but not required for anterior harsh touch [89]. A key difference in our experiments is that we bypass mechanoreceptor activation, and can therefore ignore differences in sensory neuron response to different spatial stimuli, as well as other neurons that might affect response rate. Therefore, the differential decision making observed in our experiments suggest that the two sensory systems have different strengths of connections to postsynaptic command interneurons. Particularly for PVD, although the number of physical synapses to forward command neuron PVC and backward command neuron AVA are similar [120], the functional connectivity seems to be higher for PVC compared to AVA.

Our results also provide insight on the levels of spatial encoding in the TRNs and PVD systems. The TRNs, which employ a tiled network to cover the body, appear to have more spatial encoding. When comparing the computed filters for the anterior and posterior TRNs, most behaviors show opposite directions of response. Furthermore, when analyzing this system in four segments, each segment produced a unique set of linear filters. In contrast, the branched network in PVD does not appear to spatially encode behavioral responses. The filters from activating the anterior and posterior segments of the PVD system have similar dynamics, with the anterior filters having slightly smaller magnitudes

and longer delays. This contrast between the two systems suggests that although both the TRNs and PVDs have spatially distributed processes to sense touch throughout the body, the unique morphological strategies in the two systems lead to differences in their capabilities of encoding responses. Biologically, this disparity in encoding can be explained by their morphologies, as the tiled TRN system consists of more nodes, which could allow for more specific behavioral responses.

Lastly, we investigated the role of the cryptic PVM neuron. Although shown to respond to mechanical stimuli [81], its role in mediating behavior is poorly understood [2, 6, 51, 85]. We found that activating PVM did not induce significant changes in velocity, but induced a slight decrease in acceleration. Interestingly, PVM activation significantly reduced the probability of reversal events. These filters suggest a unique function for PVM in modulating escape response. In contrast to the other TRNs, PVM does not induce escape responses, but rather suppresses these behaviors, as well as decrease the velocity of forward movement.

These findings demonstrate the utility of our method for providing new insights into the dynamics of the mechanosensory system in *C. elegans*, one of the earliest and most morphologically characterized neural circuits. By using a quantitative framework to compare the dynamics between the two sensory systems, we captured properties that are supported by previous literature, and provide further insights in the temporal and spatial encoding in these systems. Additionally, we used linear filters computed from BWA to create LNE models that accurately predict the behavioral responses of animals in response to activity in sensory neurons alone. Because this method is noninvasive and independent

of natural stimulus, it can be easily extended to investigate the dynamics of other neural circuits in *C. elegans* and other model organisms.

CHAPTER 4. FRET IMAGING IN FREELY MOVING *C. ELEGANS* REVEALS CONFORMATIONAL CHANGES IN TWITCHIN KINASE

Mechanical stimulation is crucial for the development and maintenance of muscle. However, little is known about how mechanical signals are sensed by muscle. Mounting evidence suggests that the twitchin/titin kinases are key force-sensing molecules, but evidence of force-induced conformational changes in vivo is lacking. To test this hypothesis, I imaged transgenic *C. elegans* expressing a properly localized twitchin fragment containing FRET moieties to report conformational changes surrounding the kinase domain. Imaging FRET in freely moving animals is technically challenging: first, the magnification required limits the size of the field-of-view, making it difficult to track moving animals; second, spatial specificity in measurements requires robust tracking of the animal's posture; third, movement artifacts are exacerbated in moving samples, and can have nonlinear effects that alter signals. I present here a novel technique for precisely and accurately extracting FRET signals in freely moving *C. elegans*. I implement a platform to track and simultaneously image freely moving animals in three channels (donor, acceptor, and bright-field). To extract fluorescence signals and muscle contraction states in each frame, I developed an automated computer vision algorithm. Thus, fluorescence and body curvature measurements with spatial and temporal precision can be obtained in vivo. By imaging transgenic animals carrying twitchin kinase fragment containing FRET moieties, we observe statistically significant periodic changes in FRET

signals during muscle function, consistent with a change in conformation around the kinase domain of twitchin.

This work was done in collaboration with Dr. Guy Benian (Emory University) and Dr. Olga Mayans (University of Konstanz, Germany). The reagents were designed and constructed by Yohei Matusnaga and Hiroshi Qadota from the Benian lab and Barbara Franke and Rhys M. Williams from the Mayans lab.

4.1 Introduction

Mechanical stimulation is crucial for the development and maintenance of muscle. Lack of muscle activity leads to atrophy of muscle, and exercise leads to increased muscle mass. However, little is known about how mechanical signals are sensed by muscle, and lead to a response. Mounting evidence suggests that the giant polypeptides of the twitchin/titin family are key force-sensing molecules[122]. These proteins are enormous (0.7—4 MDa) and are composed of multiple immunoglobulin (Ig) and fibronectin type 3 (Fn) domains, and one or two protein kinase domains, and in some cases, confirmed or putative highly elastic regions [123]. Depending on the protein and the organism, the protein kinase domains of these giants are either active kinases or inactive pseudokinases [124]. The protein kinase domain of vertebrate titin is a pseudokinase [125], but even for this domain, there is muscle activity-dependent "activation" that permits binding to autophagosome receptors and an E3 ubiquitin ligase [126].

These kinase domains are autoinhibited by sequences that flank their catalytic cores [124, 127, 128]. A major question is how these kinases are activated. The current hypothesis is that they are activated by small mechanical pulling forces that occur during

normal muscle activity. This idea was first suggested by [129] from molecular dynamics simulations of titin kinase, in which the ~60 residue sequence C-terminal of the catalytic core is pulled out of the catalytic pocket. Force-driven activation of titin kinase is supported by atomic force microscope (AFM) pulling on titin kinase that results in ATP binding [130]. The largest segment of a giant kinase for which we have a crystal structure is from C. elegans twitchin kinase [131].This segment consists of Fn-NL-kinase-CRD-Ig, in which NL is a 45 residue sequence, and CRD is a 60 residue sequence, that flank the catalytic core ("kinase"). The structure shows that the CRD is wedged between the two lobes of the catalytic core blocking access to ATP and petpidic substrate. The NL forms a "crown" resting on the back of the hinge between N- and C-terminal lobes; specific residues in the NL interact with residues important for ATP binding and catalysis. Recombinant *C. elegans* twitchin kinase is an active kinase in vitro when assayed with model peptide substrates [128, 132]. The NL and the CRD each inhibit kinase activity by ~50%, and when both are present the kinase is completely inhibited [131]. Molecular dynamics simulations of Fn-NL-kinase-CRD-Ig, suggest that the mechanically sensitive portion is the NL; the NL is the first portion to be removed from the structure, and the CRD remains attached to the large C-terminal lobe even after the N-terminal lobe has been unwound.

The question remains whether these force-induced conformational changes (removal of the NL of twitchin kinase, removal of CRD of titin kinase) occur in vivo. To address this question we have created transgenic *C. elegans* in which a properly localizing twitchin fragment contains FRET moieties inserted to report conformational change surrounding the kinase domain. Contracting muscles during normal locomotion would cause a conformational change surrounding the kinase domain, resulting in an increase in FRET

signal. To test this hypothesis, it is necessary to quantitatively measure the FRET signal and the muscle contractions (using local body curvature as a proxy) in freely moving animals, which is technically challenging. This would require two-color imaging with high spatial and temporal precision; additionally, movement artifacts, exacerbated in freely moving samples, could contribute to FRET signals and therefore need to be ruled out. In this work, we developed a custom tracking platform and quantitative analysis pipeline to address these challenges. We demonstrate that as the worm moves, there is indeed a detectable and statistically significant change in FRET signal that correlates with muscle contraction, which suggests that one mechanism for the kinase activation is directly due to twitchin conformational changes during contraction.

4.2 Methods

4.2.1 Tracking and Fluorescence Imaging

Tracking and fluorescence imaging were performed on a custom platform adapted from [49]. The platform used an inverted microscope (Leica-DMIRB) with a low-magnification objective (x5) to image freely moving animals. We imaged the posture of the animals using near-infrared light (this should had been declared as an abbreviation in the main text at the first place of occurrence) by applying a long-pass filter (715nm) to the transmitted light path and capture images using a large sensor NIR camera (Basler acA2040-180kmNIR).

A major innovation was the addition of an additional optical path with specific optics for imaging the FRET moieties. A chroma filter cube was used for FRET imaging, which requires the excitation of only the donor fluorophore from the excitation light. The

excitation light was delivered using a projector. A DV2 beamsplitter with [part numbers] emission filters were used to simultaneously image mCFP and mCitrine. Images were recorded using a Hamamatsu ImageXEM, with an exposure time of 50ms.

To keep the animal in the field-of-view (FOV) in all three channels, we adapted the tracking algorithm from [49] to track the GFP marker in the pharynx. We segmented the marker and performed image processing to remove noise from images. We computed the centroid of the pharynx in terms of x-y pixels on the camera FOV, and based on the position of the computed centroid, a command was sent to a motorized stage to move the animal to the center of the FOV. A Lenovo desktop computer with an Intel Core i7¬4790 Processor (8MB Cache, up tp 4.0GHz) and a 512GB Solid State Drive and 16GB RAM was used to process images for tracking. This process allowed for tracking of the animal at a rate of 13Hz, while fluorescence images are captured at a frame rate of 19.69 fps. Brightfield NIR images were captured at a frame rate of 35 fps.

4.2.2 Quantitative Behavior and Fluorescence Analysis

Quantitative values for curvatures and emitted fluorescence intensities were extracted using a custom analysis script as described in Fig 4. Because images are captured at a lower frequency with the fluorescence camera in comparison to the brightfield camera, we temporarily matched a brightfield image to each fluorescence image. The three images (NIR, mCFP, mCitrine) were spatially aligned by using set point registration of grid images taken prior to the experiment. This resulted in a data set of videos with consistent frame rates in three color channels.

For each time point, we used the brightfield images to compute the body outline and posture using analysis similar to [14, 133, 134]. We used this information to quantify muscle contraction states by computing the curvature of each point along the midline of the animal. To precisely quantify fluorescence values as a function of distance along the body, we use the midline of the body outline as a map of distances. We created separate binary mask images for the dorsal and ventral side of the animal by removing the midline from the body outline. For each point along the midline, a perpendicular line to the tangent of the curve was drawn, and the pixels that overlap with either the dorsal or ventral sides of the animal were used as a mask to extract fluorescence values. Tracking of individual sides throughout recordings was performed by comparing angles between three vectors: the centroid of each side mask to the closest point in the midline, and the tail to head vector using the midline endpoints.

4.2.3 Statistics

4.2.3.1 Muscle Contraction and Fluorescence Values

Muscle contraction values were quantified as curvature values and multiplied by -1 depending on either the dorsal or ventral side. FRET values for each point in time and along the body of the animal were computed as:

$$\mathrm{FRET}(x,t) = \frac{(\mathrm{mCtirine}(x,t) - \mathrm{mCFP}(x,t))}{(\mathrm{mCitrine}(x,t) + \mathrm{mCFP}(x,t))} \quad (5)$$

This quantification allows for normalization of overall changes in fluorescence. When comparing statistics for individual colors, values are normalized by changes from the minimum quantified value ($\Delta F/F_{min}$).

4.2.3.2 Correlation values and cross correlations

Correlation coefficients between muscle contractions and FRET values were computed using MATLAB. Cross correlation was computed using normalization to allow comparison of results between two strains. Each sample consisted of the values for contraction or FRET with respect to time for each point along the midline of each worm. Samples with low values of fluorescence emission were omitted from analysis. Statistical significance was analyzed used student's t-test.

4.2.3.3 Comparisons per muscle contraction cycle

Each cycle of muscle contraction was extracted by searching for local maxima and minima in normalized curvature data. We set thresholds for peak prominences and widths to minimize false detections of muscle contractions. Time points for each muscle contraction cycle were recorded and used to extract FRET changes as a function of muscle contraction. Changes in FRET for each part of the cycle were computed by subtracting the FRET values at the last index of the cycle from the values at the first index of the cycle. Statistical significance was evaluated using student's t-test.

4.3 Results

4.3.1 Design and validation of TwcKR FRET chimeras

In order to monitor the stretch-induced unfolding of NL and/or CRD sequences in the multi-domain kinase region of twitchin, we constructed a Fn-NL-TwcK-CRD-Ig (TwcKR) protein chimera carrying FRET moieties N- and C-terminal to the NL-Kin-CRD assembly that could act as a stretch sensor in vivo. For the design of the TwcKR-FRET chimera, the crystal structure of TwcKR (PDB code 3UTO) was examined visually and regions deemed not critical for structural integrity identified. These regions could thereby accommodate fluorescent protein (FP) moieties. In this evaluation, the location of each residue respect to mechanistically important loci in TwcKR [131, 135] was considered as well as the number and type of intramolecular contacts sustained by each residue. Importantly, locations selected for FRET partner insertion had to be within a 10 nm distance limit, as this is required for FRET to occur [136, 137]. Applying these criteria, dispensable structural elements - whose alteration would not disrupt the packing of the inhibitory NL and CRD tails against the kinase domain or affect the integrity of the kinase active site - were identified. Specifically, two loci were selected: a flexible 7-residue segment in the frontal fraction of the NL sequence (6207-DERKRRR-6213); and a 2-residue motif (6584-QP-6585) in the linker sequence between CRD and domain Ig26. These sites fulfill the distance requirements to allow FRET to take place. Upon stretch-induced unraveling of NL or CRD sequences a loss of FRET signal is expected to take place in this construction.

The sites identified were modified to receive mCitrine and mCFP FRET reporters, respectively (Figure 4.1A). Both FP are enhanced, monomeric variants of the Green Fluorescent Protein from Aequorea victoria [138, 139]. mCFP is a cyan fluorescent protein that acts as FRET donor; it is highly photostable and has λEx/λEm maxima at 433/475nm.

The mCitrine fluorescent protein, is an enhanced yellow fluorescent protein with increased brightness and photostability that acts as FRET acceptor, having λEx/λEm maxima at 516/529nm. For inclusion of mCitrine, the 6207-DERKRRR-6213 sequence (~1.6 nm end-to-end distance) was excised and replaced with the FP, including a GSG linking motif at each termini. The mCFP sequence and flanking GSG residues were inserted between the two given residues in the locus described. This resulted in a Fn-mCitrine-NL-Kin-CRD-mCFP-Ig protein chimera, where FRET moieties are located approximately 5-7 nm from each other (calculation based on the crystal structure PDB 3UTO and allowing for intramolecular flexibility and dynamics) (Figure 4.1A,B).

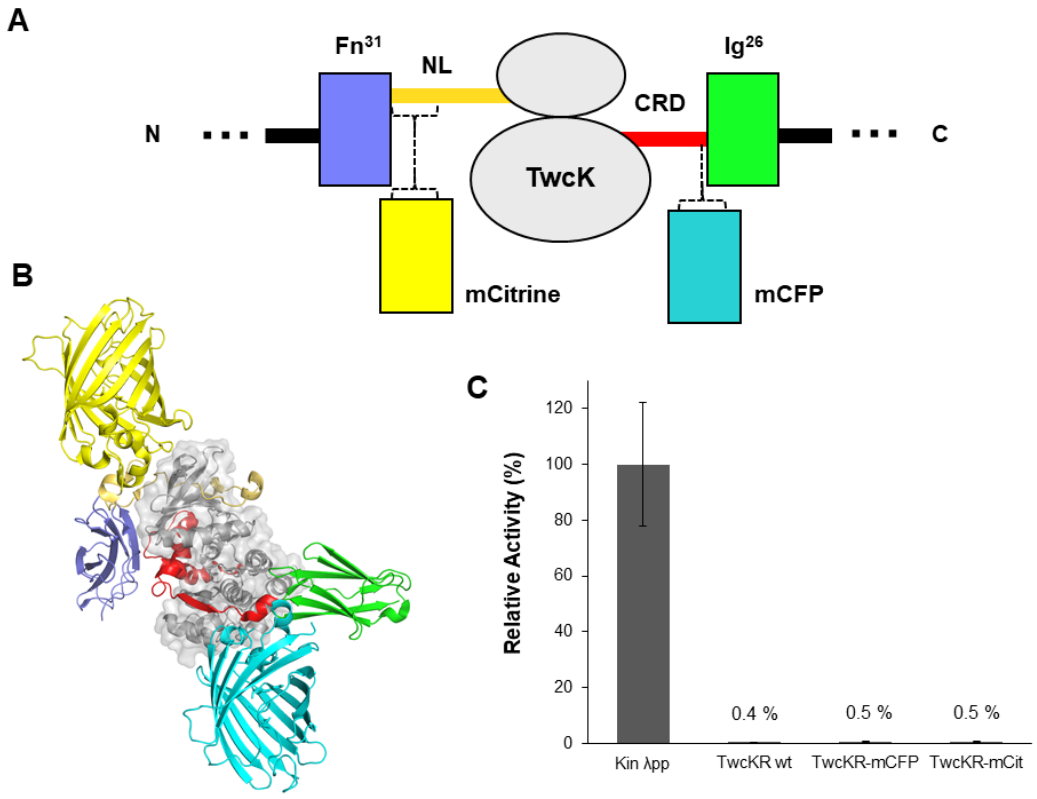

Figure 4.1 Molecular composition of the TwcKR-FRET sensor. A) Domain composition of the multi-domain TwcKR region showing the FRET insertion points. B) Structural recomposition illustrating the size and arrangement of TwcKR-FRET

domain components (crystal structures used had PDB accession code 3UTO, 1CV7 and 2YFP). C) Activity measurements of TwcKR variants using the Kinase Glo™ luminescent assay ("kin λpp" indicates the twitchin kinase domain lacking flanking segments and having been treated with λ phosphatase". Courtesy of Dr. Guy Benian.

To assess the structural impact of inserting FP proteins in the vicinity of the TwcK autoinhibitory tails, the catalytic activity of recombinantly expressed TwcKR-mCFP and TwcKR-mCit proteins was measured in a phosphotransfer assay. The NL and CRD regulatory extensions cooperatively suppress catalytic activity in TwcKR while the maximal TwcK activity is displayed by the TwcK catalytic domain lacking both NL and CRD tails (Kin) following dephosphorylation. The disruption of either tail leads to partial, but significant, levels of catalysis [131]. Catalytically active TwcKR-FRET constructs would therefore be indicative of a disruption of the packing of the autoinhibitory tails and, thereby, of the structural integrity of the NL-Kin-CRD assembly. In this study, catalytic assays showed that both TwcKR-mCFP and TwcKR-mCit have negligible activity equivalent to that of wild-type TwcKR and corresponding to approximately 0.5% of the maximal activity of the Kin catalytic domain (Figure 4.1C). This proved that the insertion of FP proteins in TwcKR for the purpose of engineering a FRET sensor has not caused an undesirable structural perturbation of this multidomain segment.

To monitor a FRET signal in vivo required addition of mCitrine and mCFP to twitchin expressed in nematodes. Because the unc-22 gene encoding twitchin is large (>60 kb; [140]), the conventional manipulation of the gene for the insertion of FRET moieties was unsuccessful. We next tried to insert the FRET proteins into the endogenous unc-22 gene using CRISPR/Cas9 technology, also without success. Thus, as an alternative strategy, we created transgenic animals expressing various portions of twitchin containing

the kinase domain under the control of a muscle specific promoter and with an HA tag. Endogenous twitchin localizes to sarcomeric A-bands in a characteristic manner in which there is lack of localization in the middle of A-bands [141]. Using anti-HA antibodies to localize the fragments (Figure 4.2A) we identified a minimal twitchin fragment that displayed normal twitchin A-band localization: Ig-Ig-Fn-NL-Kin-CRD-Ig-Ig-Ig-Ig-Ig.

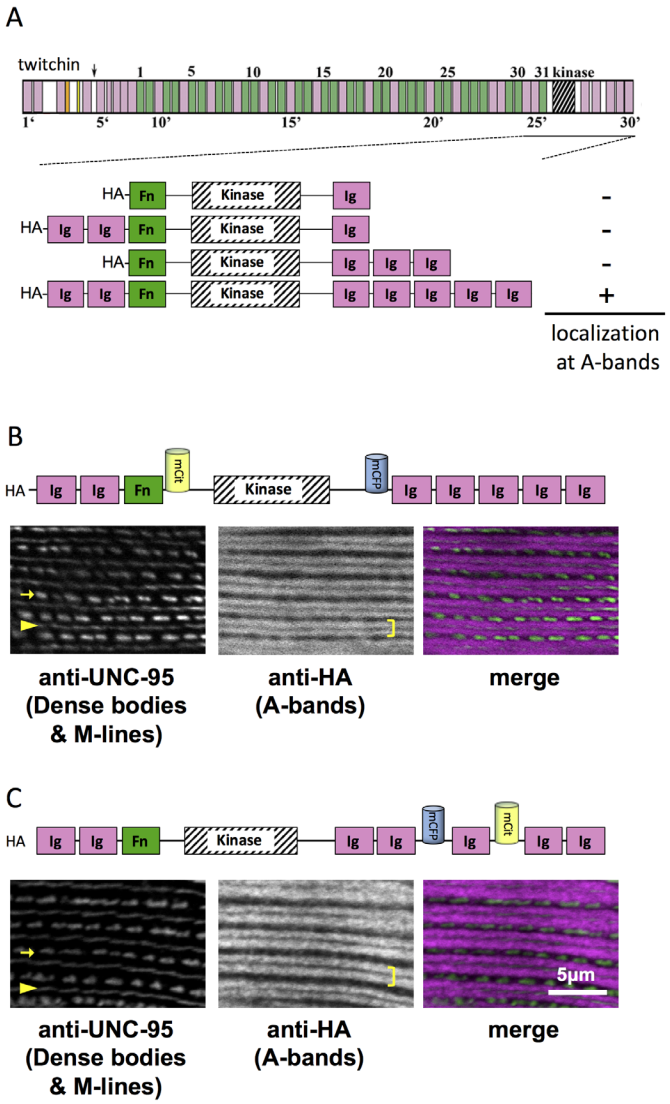

Figure 4.2 A portion of twitchin containing FRET moieties properly localizes in the sarcomere. A) Schematic representation of domain organization of twitchin and

segments containing the kinase domain tested for localization to A-bands. Note that HA-Ig-Ig-Fn-NL-Kin-CRD-Ig-Ig-Ig-Ig-Ig localizes to sarcomeric A-bands, the normal location of full-length twitchin. B) The minimally localizing twitchin fragment containing FRET moieties surrounding the kinase domain localizes to A-bands. Above, schematic; below, immunofluorescent localization. C) The minimally localizing twtichin fragment containign FRET moieties surrounding Ig28 also localizes to A-bands. Above, schematic; below, immunofluorescent localization. Arrow, row of dense bodies; arrowhead, M-line; bracket, A-band. Courtesy of Dr. Guy Benian.

We next placed mCitrine and mCFP around the kinase domain in this minimally-localizing fragment, in the same locations used in the recombinant protein (Figure 4.1). The resulting fragment, Ig-Ig-Fn-mCitrine-NL-Kin-CRD-mCFP-Ig-Ig-Ig-Ig-Ig, when expressed in transgenic worms (strain GB282) also localized normally to A-bands (Figure 4.2B). As a "negative control", we created a transgenic animal expressing the same minimally-localizing fragment but carrying FRET moieties placed on either side of Ig28. Ig28 is joined by short linker sequences to its flanking Ig domains. In this construct, FRET moieties are located 5-7 nm apart (as above, based on structural knowledge and accounting for possible intrachain FP motions). However, Ig28 has a stable fold and will unwind only under extreme force (~100 pN; e.g. [142], making this a non-extensible construction, where the FRET moieties cannot change their position relative to each other significantly at physiological muscle force. To sum up, the test construct (Ig-Ig-Fn-mCitrine-NL-Kin-CRD-mCFP-Ig-Ig-Ig-Ig-Ig) and the control construct (Ig-Ig-Fn-NL-Kin-CRD-Ig-Ig-mCitrine-Ig-mCFP-Ig-Ig) share a same twitchin backbone, have a same chemical composition and carry FRET moieties at comparable distance. However, since only the NL/CRD sequences in this fragment are expected to undergo substantial conformational changes at physiological stretch, only the FP labels in the test construct can alter their FRET signal significantly during muscle function. As shown in Figure 4.2C, Ig-Ig-Fn-NL-Kin-

CRD-Ig-Ig-mCFP-Ig-mCitrine-Ig-Ig, when expressed in transgenic worms (strain GB284), also localizes to A-bands. A similar localization of test and control fragments was expected as the base twitchin fragment is the same in both cases.

4.3.2 Precision measurements of FRET signal and curvature in freely moving animals

To study the relationship between FRET signals and muscle contractions, we sought to record fluorescence signals in freely moving animals. Muscle contraction cannot be directly measured precisely because of the size of the worm and the resolution of microscopy techniques; we reasoned that curvature is a good proxy for the state of muscle contraction. To measure both curvature and FRET in moving animal, however, is technologically challenging, as two-color imaging for FRET requires high-NA high-magnification, which only allows small field of view that is not adequate for tracking freely moving animals. In addition, since the fluorescent signals can change in magnitude, precisely registering the exact location along the worm body from frame to frame over the entire duration of the experiment is nontrivial. To address these problems, we integrated a previously developed tracking system with FRET imaging capability [49] (Figure 4.3A): this microscope-based platform enables single-animal tracking with high resolution in brightfield mode, while maintaining the animal in the field-of-view in every frame for FRET measurement; for every frame, the outline of the worm is precisely known and the FRET signal can then be mapped to the body and thus accurately correlated with local curvature.

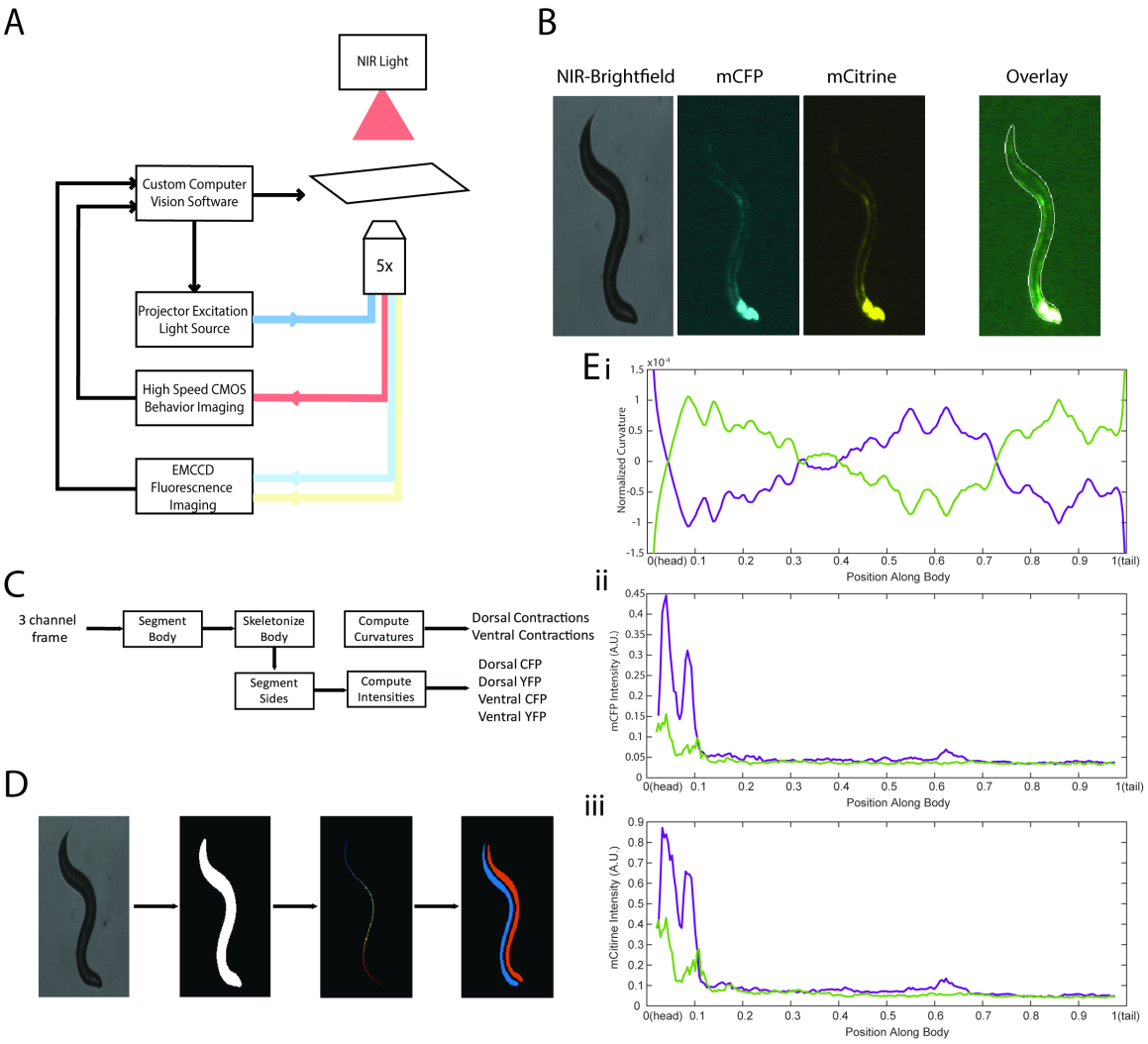

Figure 4.3 Experimental platform for posture tracking and fluorescence imaging. A) Schematic of the platform adapted from Stirman et al, 2011, which uses an inverted microscope with a 5x objective with two optical channels to image in brightfield using NIR and fluorescence imaging using a projector to provide excitation light (Methods). Tracking is performed by live analysis of a subsample of images, maintaining the pharynx of the animal in the center of the FOV of fluorescence images (Methods). B) Sample frames acquired using the platform, showing the three channels captured at each time point: NIR brightfield (left), mCFP (center), and mCitrine (right). C) The three channels are spatially aligned to allow for accurate extraction and comparisons of muscle contractions and FRET values. D) Schematic of analysis pipeline. The algorithm is performed on each frame, taking as inputs the raw three channel images. The brightfield image is then processed to produce a binary mask of the body outline of the animal. The binary image is then used to create an ordered set of points along the midline of the animal, from head to tail. The midline and body outline are subsequently used to create individual binary mask images of the dorsal and ventral sides of the animal. A tracking algorithm is used to robustly characterize the two sides

separately (Methods). E) Using the midline of the animal, (i) the magnitude of contractions are characterized, and using the mask images, (ii-iii) the fluorescnence intensities are characterized along the length of the animal for both the dorsal and ventral sides (0 = head, 1 = tail). This part is missing from the figure.

To implement this system, we added an optical path to enable two-color imaging for measuring FRET signals. The system uses an LCD-projector as a light source, which allows simultaneous and individual control of excitation bands. In order to image the donor and acceptor fluorophores in the transgenic animals, we used the blue light source to excite the donor CFP; we use a beam splitter for simultaneous imaging of the donor CFP and the mCitrine acceptor (Figure 4.3A). Fluorescence imaging was performed with an EMCCD camera, with a frame rate of 20 fps. By using a 5x objective to give a large field of view to capture the entire worm body, the spatial resolution of measurements is thus limited by the camera. In our experiments, all animals express a bright GFP marker in the pharynx (using the myo-2 promoter), which allows us to maintain the pharynx in the center of the field-of-view. Tracking (stage update) is performed at 10 Hz, which is fast enough to maintain the pharynx in the field-of-view at all time. In order to accurately determine the timings of muscle contractions, we simultaneously imaged the animals in bright-field mode with an near-infrared (NIR) light source, with a frame rate of 30 fps (Figure 4.3A, methods). By using point set registration, we aligned each fluorescence frame to a bright field frame, allowing for accurate comparisons of fluorescence signals and body postures (Figure 4.3B). This platform is therefore capable of automatic tracking of worms with simultaneous two-color fluorescence imaging, with a spatial resolution of ~2um and temporal resolution of 50ms, allowing for imaging of freely moving animals expressing the FRET moieties, and doing so for a long period of time.

To extract FRET signals and muscle contraction states in each frame of recorded videos, with spatial specificity along the length of the animal, accurately and without bias, we developed an automated analysis script (Figure 4.3C). This analysis pipeline consists of several image processing and computer vision processes (Figure 4.3D). For each set of frames, muscle contraction states are characterized by normalized curvature measurements; ventral and dorsal side of the worm body are tracked and treated separately, and assigned opposite curvatures. We use the brightfield NIR channel image, which has a high contrast between the background and foreground, allowing for robust and smooth segmentation of the body outline. The binary image of the body outline is used to create an ordered set of points along the midline of the animal, from head to tail. The midline and body outline are subsequently used to create individual binary mask images of the dorsal and ventral sides of the animal. FRET signals are computed from extracted mCFP and mCitrine emission intensities from the corresponding fluorescence recordings.

One specific challenge in this analysis is the automatic classification of dorsal and ventral sides, as animals may lie on either (the left or right) side as they are initially put down on the agar plate, and the animals change locomotion directions drastically throughout recordings. To robustly track the two sides throughout recordings, we compute the angles between the center of mass of each side and the midline of the animal (Methods). This allows us to continuously track the ventral and dorsal assignments. With this algorithm, we can thus obtain time series values of muscle contractions and fluorescence intensities as a function of exactly locations along the body (Figure 4.3D).

By using this analysis pipeline on the three channel recordings, we obtained quantifications of muscle contractions and fluorescence intensities with spatial and

temporal precision for each trial. For each recording, fluorescence intensities, FRET signal, and curvature can be visualized in kymographs (Figure 4.4A-C). We characterized values for both the dorsal and ventral sides of the animal independently. As expected, most of the time the animals move forward with a traveling wave propagating backwards, and curvature values show clear and smooth diagonal patterns (Figure 4.4A), similar to recorded kymographs in other studies [Wen et al 2012, Fouad et al 2018, Gao et al 2018]. In addition to muscle contractions, for each recording we also extract mCFP and mCitrine emission measurements as a function of both time and distance along the worm body (Figure 4.4B, C). In comparison to curvature measurements, fluorescence measurements are more variable between animals and along the anterior-posterior axis of the animal and have a lower signal-to-noise ratio. Nonetheless, these measurements also display a diagonal pattern similar to muscle contractions, suggesting that FRET and curvature of the muscle elements are related. Significantly, when examining the curvature and fluorescence signals for an individual segment, we see oscillatory patterns in time, with similar frequencies for all signals (Figure 4.4D,E). Additionally, this consistency between the fluorescence signals and curvature dynamics of freely moving animals suggests that the relationships between these variables may be causal.

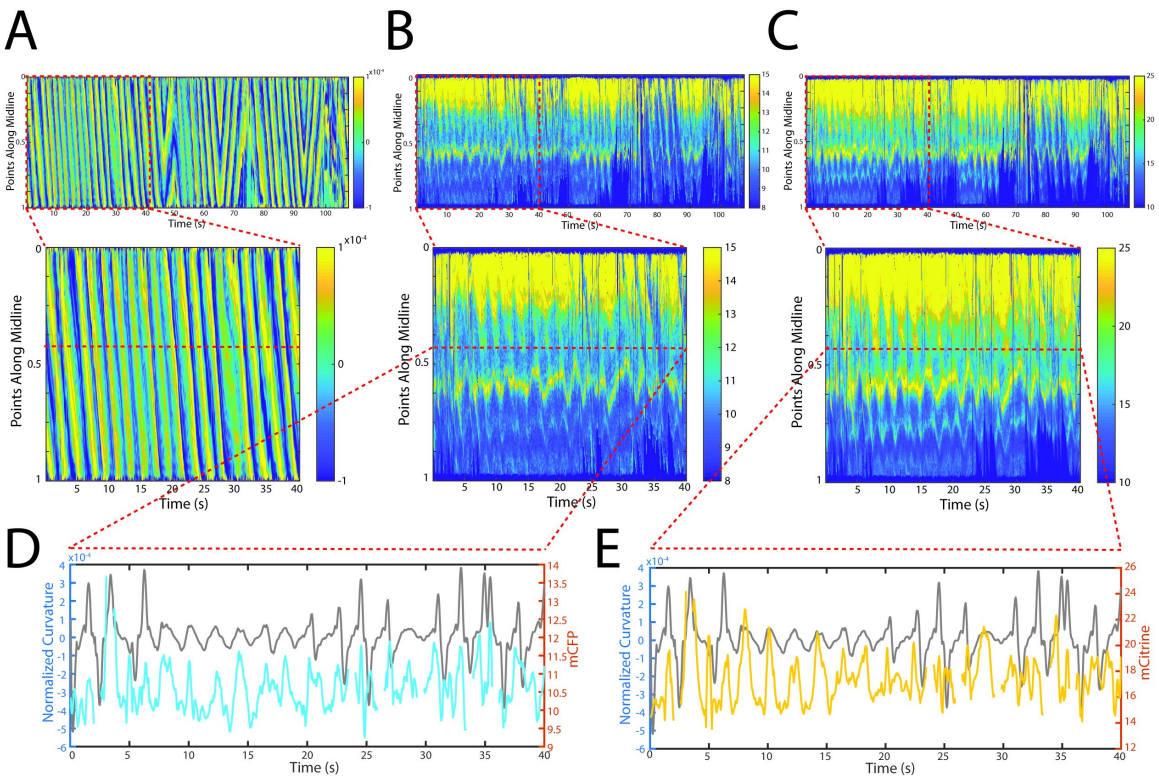

Figure 4.4 Tracking platform and analysis pipeline provide precise spatio-temporal measurements of normalized curvature and fluorescence intensities. A) Sample measurements of normalized curvature (C(x,t)) for one side during a recording. B) mCFP and (C) mCitrine fluorescence measurements in the same side for the recording in (A). D,E) Sample traces of normalized curvature and (D) mCFP and (E) mCitrine intensities for a given point along the animal.

4.3.3 A possible conformational change in the kinase domain of twitchin

Using our imaging, tracking, and analysis platform, we next investigated the relationship between the state of muscle contractions and twitchin conformational changes. We developed two transgenic strains: GB282 (FRET testing strain), which expresses a properly-localizing twitchin fragment with FRET moieties flanking the kinase domain, and GB284 (control), which expresses a similar twitchin fragment with FRET moieties flanking the Ig-28 domain in the same twitchin localizing fragment (Figure 4.2B). A positive FRET signal results from donor fluorophores (mCFP) exciting acceptor

fluorophores (mCitrine), which typically results in intensity decreases for the donor and increases for the acceptor. However, when imaging the FRET testing strain (GB282), we observe increases in both mCFP and mCitrine intensities during muscle contractions (Figure 4.5A-C). This suggests that a movement artifact can affect our measurements, likely a result of fluorophores becoming more densely packed in space during contractions, leading to higher measured values of fluorescence intensities in our imaging platform. However, when computing FRET signals normalized by overall changes in intensities (Methods), we still observe traveling wave (diagonal patterns) similar to curvature (Figure 4.5D). This positive change in FRET during muscle contractions can arise both from true FRET signals and from nonlinearities in movement artifacts.

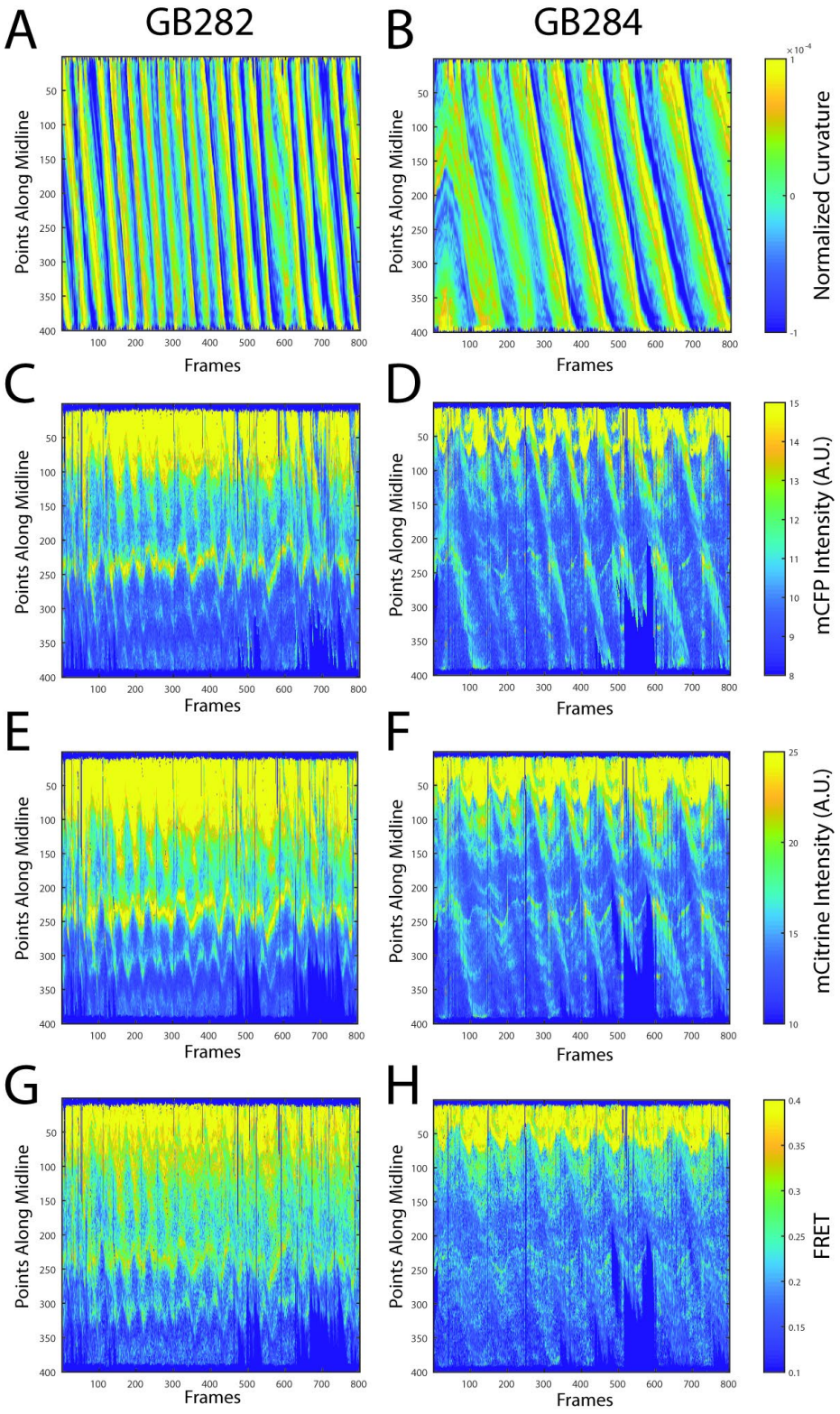

Figure 4.5 FRET signals for GB282 and GB284 are qualitatively correlated with muscle contractions. A-D) Sample measurements for GB282 of Curvature (A), mCFP

(B), mCitrine (C), and FRET (D) for one side of a recording. E-H) Sample measurements for GB284 of Curvature (E), mCFP (F), mCitrine (G), and FRET (H) for one side of a recording.

To determine if movement artifacts can result in significant FRET signals and whether these artifacts overwhelm the true FRET signals, we imaged the negative control strain (GB284) where we do not expect the FRET pair to change relative distance during muscle contraction. Similar to GB282, we observe increases in both mCFP and mCitrine intensities during muscle contractions (Figure 4.5E-G), suggesting that a movement artifact indeed arises as a result of imaging fluorescence intensity in freely moving animals. This is further corroborated by the computed normalized FRET signal, where we still observe diagonal patterns similar to curvature; however, compared to GB282, the control group (GB284) shows smaller changes in the overall FRET signal (Figure 4.5H). As GB284 expresses the fluorophores directly flanking Ig28 without any significant flexible segments in between, the computed FRET signals can only be explained either by nonlinearities in the intensity movement artifacts, or from interactions between the FRET moieties in adjacent molecules, and not donor to acceptor activities. The higher changes in computed FRET for GB282 suggest that an additional FRET signal arises from interactions between the FRET moieties flanking the kinase domain in a single molecule. Taken together, although movement artifacts leads to non-zero FRET signals, qualitatively higher signals in GB282 compared to GB284 suggest that a conformational change occurs near the kinase domain of twitchin during muscle contractions.

To quantitatively compare the difference in FRET signals between GB282 and GB284, we sought to characterize direct correlations between computed FRET signals and curvature measurements, using multiple recordings and treating each point along a worm

as an independent sample. We first computed cross correlations between these values (Figure 4.6A, B). For both strains, the majority of samples have a maximum correlation at a delay of t=0, suggesting that there is no observable delay between FRET signals and curvature as measured in our imaging platform. Moreover, the periodic patterns observed in the cross correlation plots suggest that the observed positive correlation is indeed due to locomotion, and not arbitrary artifacts. As there is no delay between these signals, we computed correlation coefficients to quantitatively compare relationships between fluorescence signals and curvature measurements in the two strains. As expected, we observe positive correlation coefficients for both mCFP and mCitrine intensities in both strains (Figure 4.6C). Interestingly, the correlation coefficients for mCFP are statistically similar for both strains (Figure 4.6C. left), whereas correlation coefficients for mCitrine are statistically higher for GB282 compared to GB284 (Figure 4.6C, middle and right). This suggests that movement artifact only partially explains the increases in mCitrine during muscle contractions for GB282. Taken together, these results suggest that although movement artifacts lead to positive computed FRET signals during muscle contractions in both strains, a significant portion of the computed FRET signal in GB282 arises from conformational changes around the kinase domain.

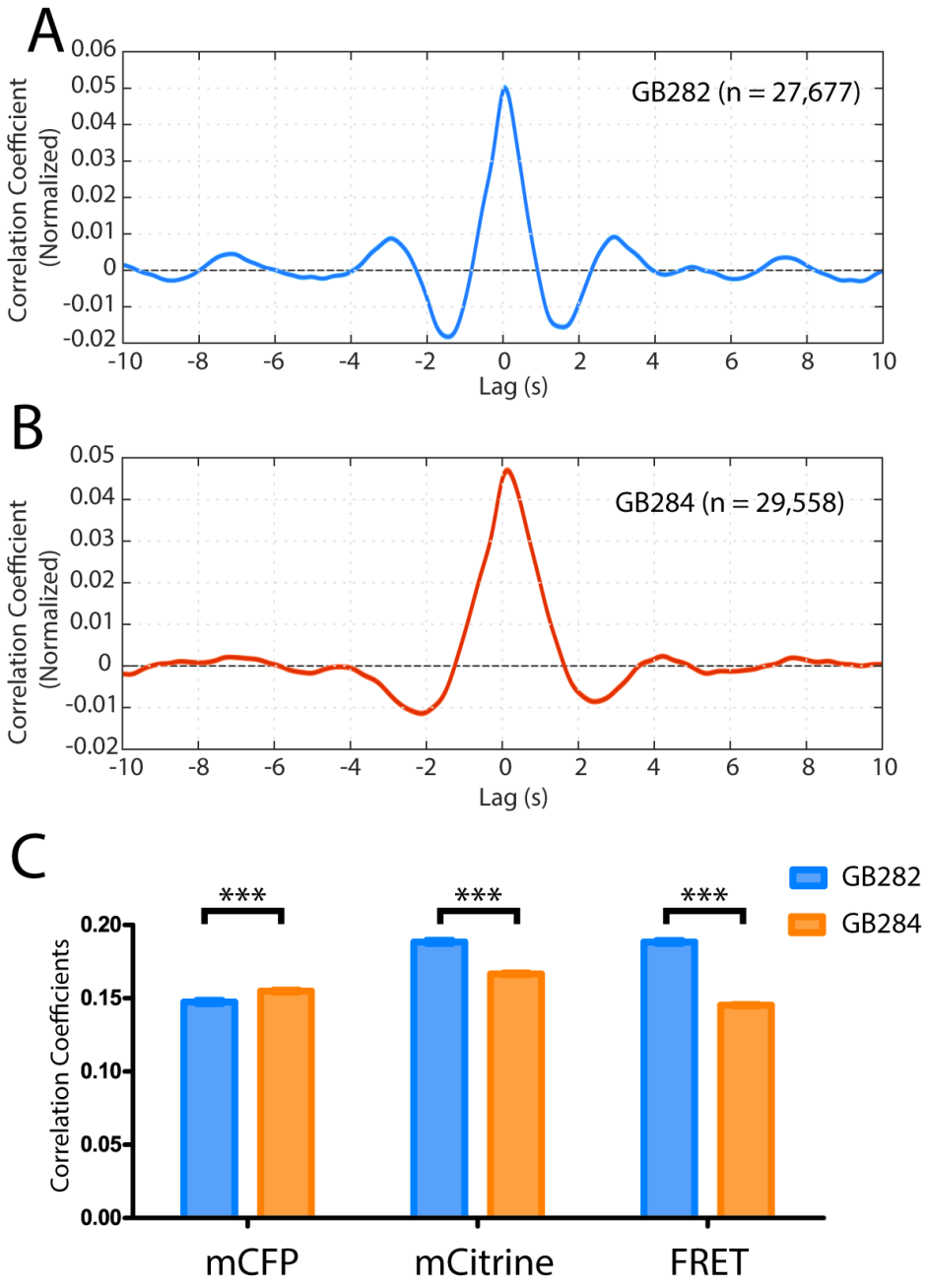

Figure 4.6 Statistical analysis reveals correlation between muscle contractions and FRET activity. A) Cross correlation analysis for GB282 (n= 27,677/30). B) Cross correlation analysis for GB284 (n=29,558/30). C) Correlation coefficients between muscle contractions and mCFP, mCitrine, and FRET for strains GB282 (n=27,677/30) and GB284 (n=29,558/30) (student's t-test).

To further quantify the effect of the movement artifact in the measured FRET signals, we sought to compare the average measured FRET signals for all cycles of muscle

contractions. To do this, we performed another automated analysis, searching for all muscle contraction cycles in our data set of curvature measurements, from full relaxation to full relaxation (Figure 4.7A). We then aligned computed FRET signals to those time points for both strains. Although both strains exhibit increases in FRET during muscle contractions and decreases during muscle relaxations, the magnitude of these changes are significantly higher for GB282 (Figure 4.7B). We compared changes in FRET in four separate sections of the muscle contraction cycle: Fully relaxed to mid-cycle , mid-cycle to fully contracted , fully contracted to mid-cycle , and mid-cycle to fully relaxed. For each part of the muscle contraction cycle, the magnitudes of changes in computed FRET were significantly higher for GB282 compared to those for GB284 (Figure 4.7C). Taken together, these results indicate that a large portion of the observed FRET signal in GB282 arises from interactions between the FRET moieties due to conformational changes near the kinase domain of twitchin.

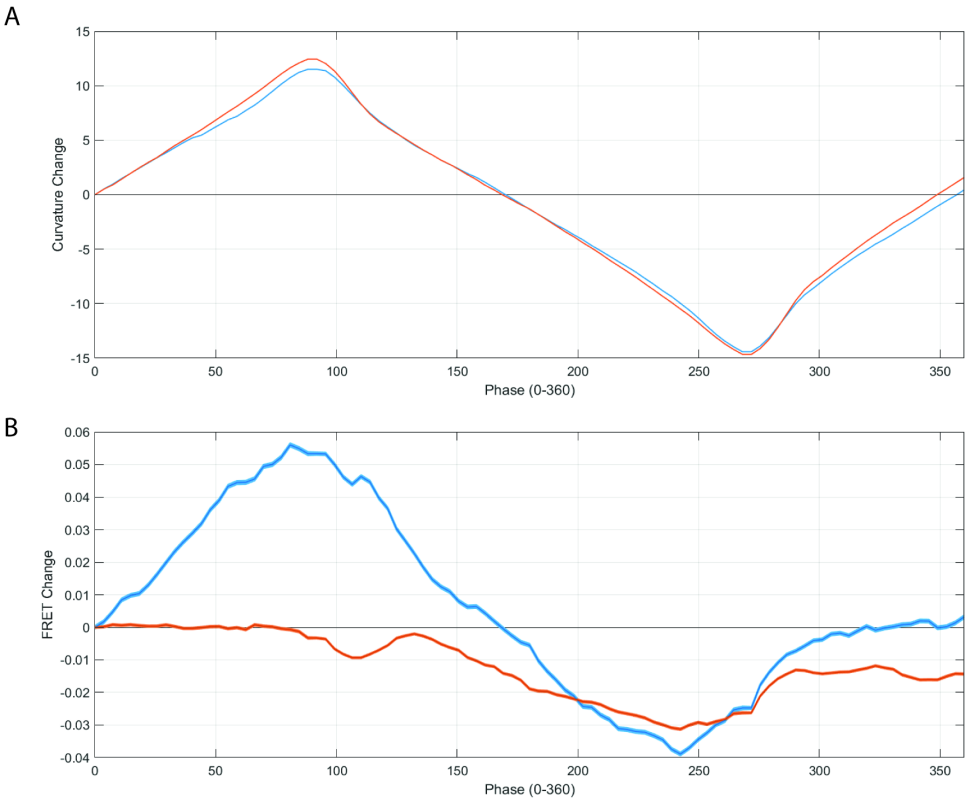

Figure 4.7 Changes in FRET suggest a conformational change during muscle contraction cycles. A) Average normalized curvature values aligned to cycles of muscle contractions, with 90 degrees representing maximum contraction, and 270 degrees representing maximum relaxation, for GB282 (blue, n>=13,840/30) and GB284 (orange,n>=11,707/30). B) Average FRET values for GB282 (blue) and GB284 (orange) aligned to same cycles of muscle contractions as in (A).

4.4 Discussion

Kinases of the titin/twitchin family are integral part of elastic, sarcomeric filaments that exist embedded within the lattice of actin-myosin motors. These cytoskeletal kinases experience pulling forces during muscle function. The mechanical strain has been speculated to induce the conformational deformation of regulatory tail extensions flanking these kinases and which pack against their functional centers. Mechanically-induced changes in these regulatory segments have been speculated to control kinase activity and/or the recruitment of sarcomeric proteins to kinase-based signallosomes, thereby liking

mechanosensing with stress-response pathways in the myofibril and suggesting that these kinases might act as mechanosensory nodes in the sarcomere. However, despite the central significance of this mechanism to muscle physiology, data supporting it derive only from AFM studies and SMDS simulations with no study having tested to date its existence in vivo at physiologically relevant forces. To address this outstanding question, we sought to investigate the mechanical regulation of twitchin kinase in vivo during muscle activity and using live, freely moving animals. To overcome the technical challenges of this goal, we applied an integrative approach, developing a transgenic nematode that expresses a twitchin fragment with FRET moieties near the kinase domain, and developing a tracking platform with a robust analysis pipeline for precise measurements of FRET signals in freely moving animals. We observe significant changes in FRET signals during muscle contractions in test over control *C. elegans* strains, suggesting that we have observed conformational changes in the twitchin kinase flanking regions.

As expected, movement artifacts greatly affected fluorescence measurements in freely moving animals. Movement artifacts were particularly a problem as we were imaging body wall muscles; it is possible that fluorophores become more densely packed during muscle contractions, leading to a measured rise in fluorescence simply due to the density of fluorophores. Additionally, optical aberrations due to the nearby cuticle or agar can greatly affect measurements. We used two strategies to overcome these movement artifacts in our measurements. First, by using FRET, we computed ratiometric values that were normalized to the sum of the two fluorophores. Although this was effective in removing a large portion of movement artifacts, it only removed linear effects. Second, we compared test and control strains expressing a same twitchin fragment but containing

FRET moieties at different locations. It is reasonable to expect that both fragments will incorporate equally in the sarcomere, which is supported by their antibody labelling in sarcomeres. It could be expected that artifacts – for example, FRET arising from inter- vs. intra-molecular interactions and lattice packing effects in the sarcomere – will be equally present in both strains. As the FRET signal is substantially larger in the test strain, we conclude that the measured FRET signal is due to conformational changes near the kinase domain which exceeds movement artifacts. By using these two strategies, we were able to confirm with statistical significance that we observed a FRET signal due to conformational changes in TwcK taking place at physiological forces during muscle contraction as a result of the shearing forces arising in the sarcomere.

In addition to the biological insight of twitchin, the novel technologies described in this chapter also provide insight in the technical challenges and capabilities of fluorescence imaging in freely moving animals. In order to perform FRET imaging in freely moving animals, we integrated a tracking platform with fluorescence microscopy, which enabled recordings of the whole animal within the FOV while maintaining high enough spatial resolution to measure fluorescence along the body of the animal. Additionally, novel image processing pipeline was necessary to extract spatiotemporal measurements of fluorescence from experimental recordings. To our understanding, this is the first demostration of spatiotemporal FRET measurements in freely moving *C. elegans*. In addition to the investigation of twitchin conformational changes, this novel technology can be applied to investigate the function of any cell or pathway in freely moving animals. This allows for the direct investigations of how specific cells or proteins affect or are affected by the animal's movement. One potential application is the investigation of how activity in

neuronal processes vary compared to cell bodies of various neurons, and whether spatial dynamics in neuronal processes correlate with behavior. Another potential application is in the field of proprioception, as this technology allows for measuring neuronal activity in varying postures of the animal. Altogether, the novel technologies developed in this chapter overcome key technical limitations in fluorescence imaging experiments, and allow for novel investigations in freely moving animals.

CHAPTER 5. CONCLUSIONS

5.1 Thesis Contributions

The objective of this thesis was to develop integrated platforms for all-optical interrogation of the nervous system of *C. elegans*. Specifically, I aimed to use image processing techniques in combination with microfluidic devices, to improve robustness, as well as enable new capabilities, in both experimentation and analysis of several components of the *C. elegans* nervous system. This advances the field of *C. elegans* neuroscience by enabling novel experiments and addressing biological questions not previously possible.

In Chapter 2, I developed several integrated techniques to solve specific biological questions. In the first section, I, in collaboration with a previous member of the lab (Dr. Ivan Caceres), developed an integrated platform to perform an automated genetic screen to investigate novel pathways affecting spinal muscular atrophy (SMA). We developed an image processing algorithm to perform classification mutant phenotypes using the worm model of SMA. Using this algorithm, we performed an automated forward genetic screen, improving the throughput from previous approaches by ~100X. The screen resulted in 21 isolated alleles that revert the neurodegeneration mutation. These alleles are now being further studied to identify possible novel pathways affecting SMA. In the second section, I developed image processing techniques to improve both throughput and precision in analyzing calcium imaging recordings. In collaboration with an alum of the lab (Dr.

Yongmin Cho), we used microfluidics and calcium imaging to record neuronal responses to mechanical stimuli in *C. elegans*. I developed a neuron tracking algorithm that automates the analysis of recordings from our experiments. Furthermore, I developed a graphical user interface (GUI) that enables user supervision of the neuron tracker, allowing for accurate extractions of fluorescence intensities. I also developed an algorithm to track neuronal processes in calcium imaging recordings. Using this technique enables spatiotemporal visualization of neuronal activity.

In Chapter 3, I developed a novel experimental platform for investigating dynamics in neuronal circuits. I adapted a platform designed by an alum of the lab (Dr. Jeffrey Stirman), which uses real-time image processing and optogenetics to track and selectively stimulate neurons in freely behaving animals. I used signal processing theory to perform optimized experiments to characterize dynamics in response to activation of specific neurons. Using this platform, I investigated spatial and temporal dynamics of two mechanosensory systems, the gentle touch receptor neurons (TRNs) and harsh touch sensing PVDs. Our results suggest that the tiled network of the gentle-touch neurons has better resolution for spatial encoding than the harsh-touch neurons. Additionally, I produced linear-nonlinear models that accurately predict behavioral responses based only on sensory neuron activity. The results in this work capture the overall dynamics of behavior induced by the activation of sensory neurons, providing simple transformations that quantitatively characterize these systems. Furthermore, this platform can be extended to capture the behavioral dynamics induced by any neuron or other excitable cells in the animal.

In Chapter 4, I developed an integrated platform combining fluorescence imaging with live-tracking of freely behaving animals to enable the investigation of the function of a muscle molecule *in vivo*. In addition, I developed a novel algorithm to automatically analyze recordings, resulting in spatiotemporal maps of fluorescence intensities in muscles. The experimental platform enabled for high throughput experimentation, and the image processing algorithm enabled extraction of data in high resolution, allowing for robust analysis with high sample sizes. I used these developed tools to investigate the possibility of twitchin as a force sensing molecule. In collaboration with Dr. Guy Benian (Emory University), we show that the kinase domain of twitchin go through conformational changes during muscle contractions.

In general, the platforms developed in this thesis were designed with the goal of answering specific biological questions about the *C. elegans* nervous system. These platforms have enabled novel insight into various aspects of the nervous system, furthering understanding of nervous systems in general, as well as insights on neurological and other human disorders.

5.2 Future Directions

The work presented in this thesis demonstrate the capabilities of integrating existing experimental techniques with novel algorithms to perform high-throughput in vivo functional imaging and behavior tracking, while tracking probing specific neurons or external stimuli. In this section, I discuss possible applications of our technologies for future work.

5.2.1 Investigation of interneuron function in mechanosensation circuit

In Chapter 3, I developed a novel experimental platform to investigate the dynamics of the mechanosensation circuit in *C. elegans*. In this work, I use reverse correlation to quantify mathematical transformations from sensory neuron activation to behaviour outputs. This method resulted in linear and nonlinear filters that accurately predicted behavioural outputs from sensory neuron stimulation. Although this technique successfully captured dynamics between sensory neuron activity and behaviour response, the interneurons involved in this circuit are not investigated. Similar to the sensory neurons involved in mechanosensation, the interneurons involved in the circuit have been identified, but little is known about their temporal dynamics and integration of presynaptic inputs.

One future direction for the work in Chapter 3 is to extend our method to include functional imaging of interneurons. In addition to using optogenetics to activate sensory neurons and tracking to quantify behavioural outputs, simultaneous functional imaging of interneurons can be used to observe how interneurons compute sensory neuron activity to produce behavioural outputs. Reverse correlation can be performed with extracted activity signals of interneurons instead of behavioural outputs. This would allow for the quantification of transformations from sensory neuron activity to interneuron activity. Furthermore, spatial integration of sensory neurons can be investigated by taking advantage of the selective illumination capabilities of the platform. A key challenge in this future direction is the experimental challenge of simultaneously using optogenetics, functional imaging, and tracking of freely moving animals.

5.2.2 Investigation of age differences in mechanosensation dynamics

In chapter 3, we elucidated the linear and nonlinear filters for TRNs and PVDs using only day 1 adult animals. Another future direction for the work in Chapter 3 is to investigate the effect of age in mechanosensation dynamics. It is known that the synaptic connections of TRNs change throughout development, but little is known about how these different synaptic connections affect circuit dynamics and behavioural outputs. By performing the same experiments with animals at different stages in their life cycle, we may elucidate key functions for specific synaptic connections.

APPENDIX A. SUPPLEMENTAL INFORMATION FOR CHAPTER 2

A.1 Supplemental Information for Section 2.1.1

Isolated Allele	Number of Motor Neurons		
	Mean	Std	% ≥15
Non mutagenized (n=60)	9.3	2.8	6.7%
a182 (n=25)	12.6	2.3	26.1%
a183 (n=24)	13.4	2.0	32.0%
a184 (n=23)	12.9	2.5	26.1%
a185 (n=21)	11.8	3.9	33.3%
a186 (n=25)	14.2	2.0	56.0%
a187 (n=25)	16.5	1.2	92.0%
a188 (n=25)	15.1	2.6	64.0%
a189 (n=25)	15.3	2.4	68.0%
a190 (n=25)	17.0	1.4	92.0%
a192 (n=25)	15.2	2.2	76.0%
a193 (n=25)	14.9	1.6	64.0%
a194 (n=25)	14.5	2.0	60.0%
a195 (n=25)	17.5	1.2	96.0%
a196 (n=25)	15.2	1.3	60.0%
a197 (n=25)	12.3	2.0	12.0%
a198 (n=25)	14.5	1.9	56.0%
a199 (n=25)	16.0	1.8	76.0%
a200 (n=25)	12.4	2.4	16.0%
a201 (n=25)	16.7	1.1	100.0%
a202 (n=25)	12.6	2.4	24.0%
a203 (n=25)	16.2	1.7	80.0%

Table A. 1 Summary of manual confirmation of isolated alleles from Section 2.1.1.

A.2 Granulometry

In addition to the worm described in Chapter 2, I also worked on a loosely related project in collaboration with two alums from the lab (Dr. Ivan Caceres and Dr. Maria Elana Casas). This project was also focused on a biological question, and involved classification

of lipid droplet mutants in *C. elegans*. Analysis of densely packed overlapping objects is a common, yet complex computational problem. Segmentation algorithms have been used for object recognition; however, applying a robust nonparametric algorithm for a high degree of occluded objects is difficult. To address this issue, we developed a modified granulometry algorithm that characterizes overlapping objects through a semi-quantitative textural analysis of the object size distribution. We use the method to characterize *C. elegans* lipid droplet size distributions, which are densely packed and highly overlapping. Efficient classification of various lipid droplet phenotypes is highly desired, as it would allow for the discovery of novel genes and mutations associated with lipid storage and metabolism. We show that our method can accurately classify between wild type and mutant lipid droplet phenotypes, without the need to optimize parameters. We use this algorithm to conduct a novel automated genetic screen of lipid droplet size distribution phenotypes, where a priori knowledge of the sizes is unknown and varies between each animal. We performed the screen approximately 500 times faster than previously capable, and discovered a new lipid droplet mutant.

My main contribution to this work was to characterize the accuracy of our method. I first sought to estimate the object size distributions of synthetic images with known distributions. I generated a synthetic image library with densely packed, overlapping disks of three different sizes and random intensity values (Figure A. 1A). Our method yielded accurate results for object distribution by size, with an average error of roughly 1% for each size (Figure 3B), and a total cumulative error of 3.46±1.72% (Figure A. 2A), demonstrating our ability to accurately determine the number of disks in an image without individual segmentation. In addition to disks, synthetic libraries with varying sizes were

also created for square and rhombus shapes. The cumulative mean error for the square and rhombus shapes were 1.51±0.99% and 9.41±1.48%, respectively (Figure A. 2B), demonstrating that the granulometry algorithm can also estimate size distributions of varying shapes.

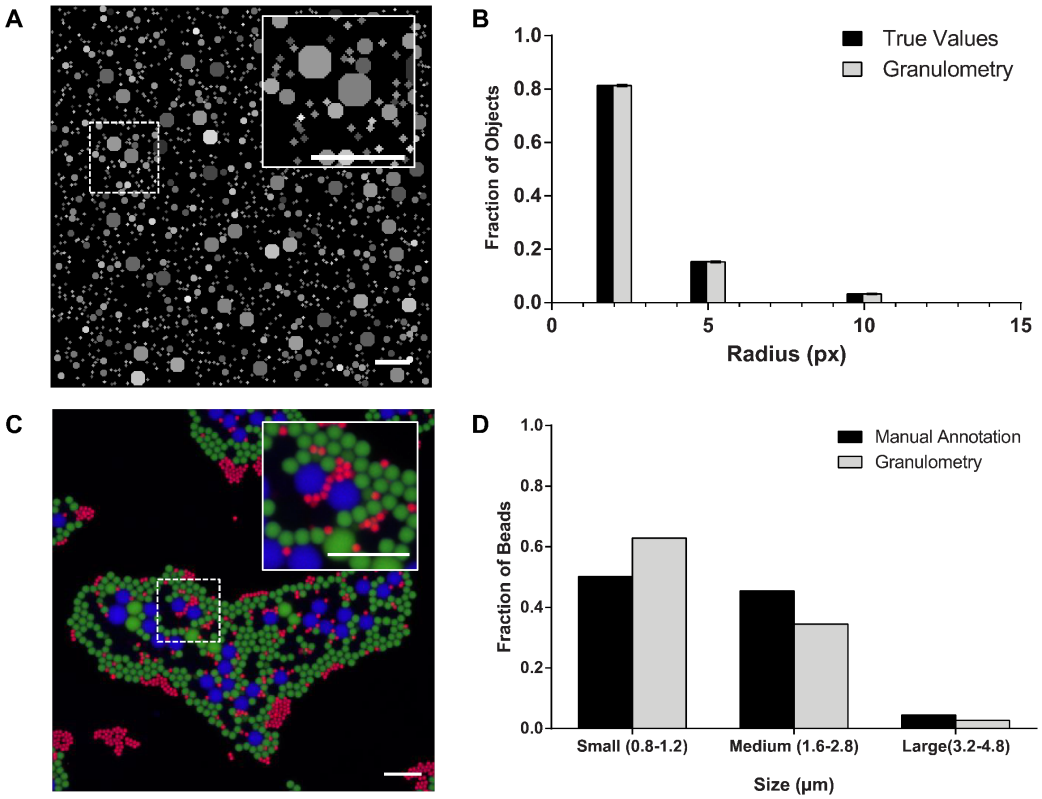

Figure A. 1 Validation of granulometry algorithm using synthetic and confocal microscopy beads for size reference. A) Representative synthetic image with disks of varying diameters (2, 5, 10 px) and varying intensities (1-255), insert shows structuring elements are not perfect disks but a close approximation. (Scale bars = 50 px) B) Synthetic image validation shows that granulometry is very accurate when objects are similar to structuring elements used in morphological openings. (n=100 images) C) Representative confocal image of clustered beads of varying intensities, colors, and diameters, insert shows how edges are not as well defined as in the synthetic images. (Scale bars = 10 µm) D) Results show that the hand annotated value of the diameters in the image closely follow that of the modified granulometry algorithm, indicating that although each method has inherent error partially due to the gradient at the edges, the modified granulometry algorithm diameters are similar to the hand annotated diameters. (n = 25 images).

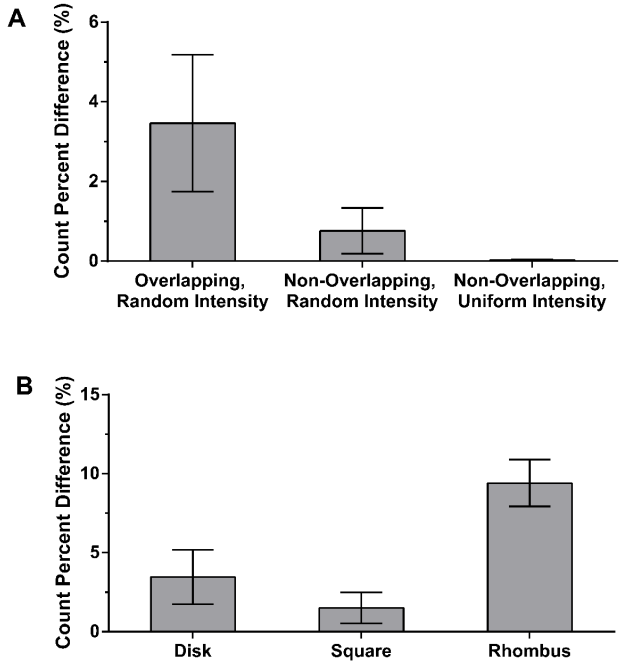

Figure A. 2 Source of algorithm errors. A) The inter-object distance was tested and the error in the number of objects detected was calculated from the defined parameters of the synthetic image. The least amount of error is seen when uniform intensity is used and there is no touching or overlapping objects. The error is less than 0.25% for any of these scenarios so it can be concluded that a small portion of the error for the algorithm is due to the proximity of objects, and more so from changes in intensity. The changes in intensity is corrected in the algorithm by preprocessing the image to have a more uniform intensity for the foreground which includes the objects to be measured. B) In addition to disks, the algorithm can also be used to analyze other shapes such as squares and rhombi. The cumulative mean error of the number of objects detected is less than 10% for each of the different sizes, demonstrating that the algorithm can also be used on other structures other than disks with similar accuracy.

I considered two possible sources of error in our method: object proximity and intensity differences between objects. One source of error in our method is close proximity between objects, where neighboring or overlapping objects are considered a single object. To test how much of the error is due to this problem, I tested our method on new synthetic images with no overlapping objects. When analyzing these images, our method yielded an

improved accuracy with a total cumulative error of 0.76±0.58% (Figure A. 2A). To determine how much of the error is due to intensity variation, I tested our method on a library of synthetic images of objects with uniform intensity. With this library of images, the error was almost eliminated, with a reduced cumulative error of 0.02±0.01% (Figure A. 2A). These findings indicate that object proximity and intensity variation account for the majority of errors in our algorithm.

I next sought to characterize our method with real microscopy images with unknown noise. To do this, I took confocal-microscopy images of densely packed fluorescent beads of three various sizes (Figure A. 1C). I compared the object size distributions resulting from our algorithm with manually annotated values, and observed similar values (Figure A. 1D). This comparison shows that our algorithm is capable of distinguishing amongst the three bead diameter sizes in the mixed population showing that the algorithm can determine the size distributions in an image with a high density of objects and edges without sharp gradients. As in synthetic image experiments, errors between computational analysis and manually measured values can be attributed to the density and close proximity of objects (fluorescent beads). To characterize this effect, I created image libraries of bead with specific diameters and assessed the accuracy of our analysis method (Figure A. 3A). In analyzing beads with size ranges from 0.5 μm to 5 μm, the standard deviation for each of the different sizes is less than 1 μm of the stated manufacturer's size range (Figure A. 3B, C). This minimal overlap between the size distributions of the various bead sizes demonstrates that the sizes are accurately discernable when using our method.

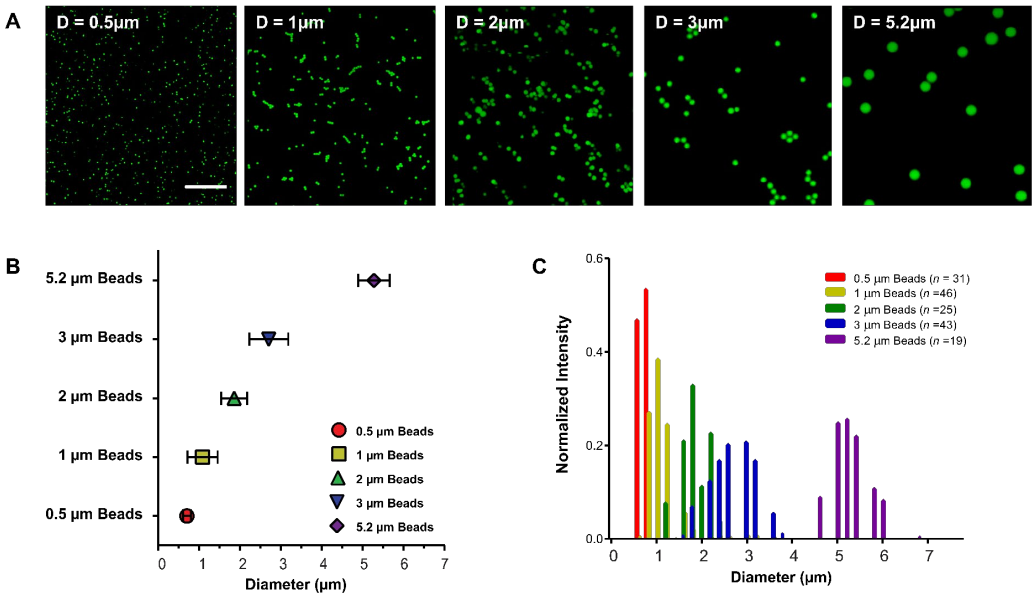

Figure A. 3 Algorithm accuracy in characterizing a library of fluorescent bead images. A) Representative images of fluorescent beads imaged with increasing sizes where the diameter is indicated on the top left corner. The beads were selected to be in the biologically relevant size range of the lipid droplets in *C. elegans*. (scale bar = 20 µm) B) Mean diameter size for the individual bead populations were calculated using granulometry, and the manufacturer's stated diameter matches up closely with that of the analyzed diameter. C) Full distribution results from granulometry show the size ranges for the beads detected. This shows that various sizes are discernable when using granulometry.

APPENDIX B. SUPPLEMENTAL INFORMATION FOR CHAPTER 3

B.1 Supplemental Figures and Table

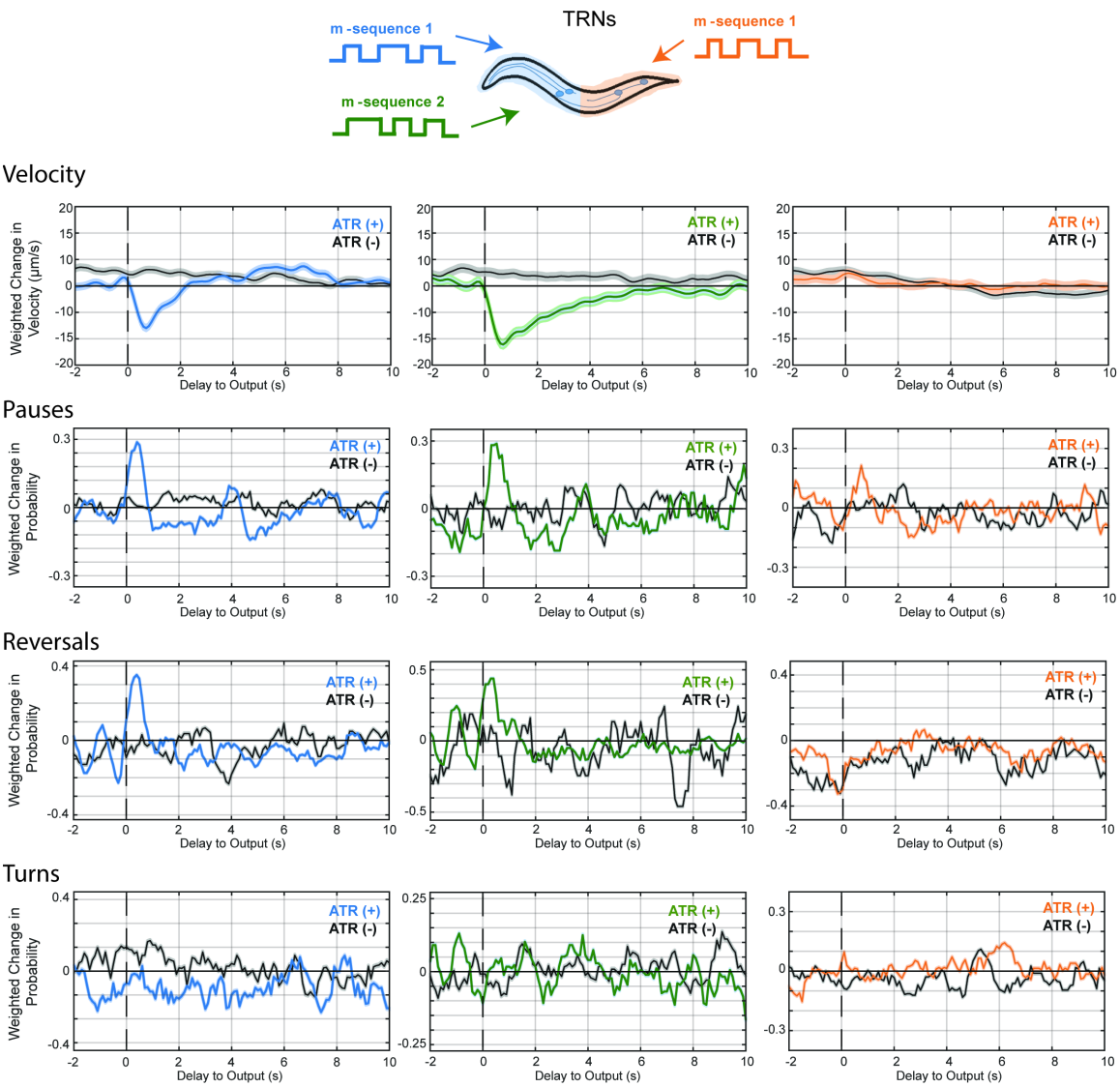

Figure B. 1 Additional linear filters for TRNs. Linear filters computed for various behaviors when stimulating the anterior TRNs with an m-sequence signal (left), a different m-sequence signal (center), and the posterior TRNs (right). Dark line and light shade represent BWA and SEM, respectively. Colored plots represent filters computed from ATR-fed animals, black plots represent filters computed from control (not ATR-fed) animals. Sample sizes listed in Table S1.

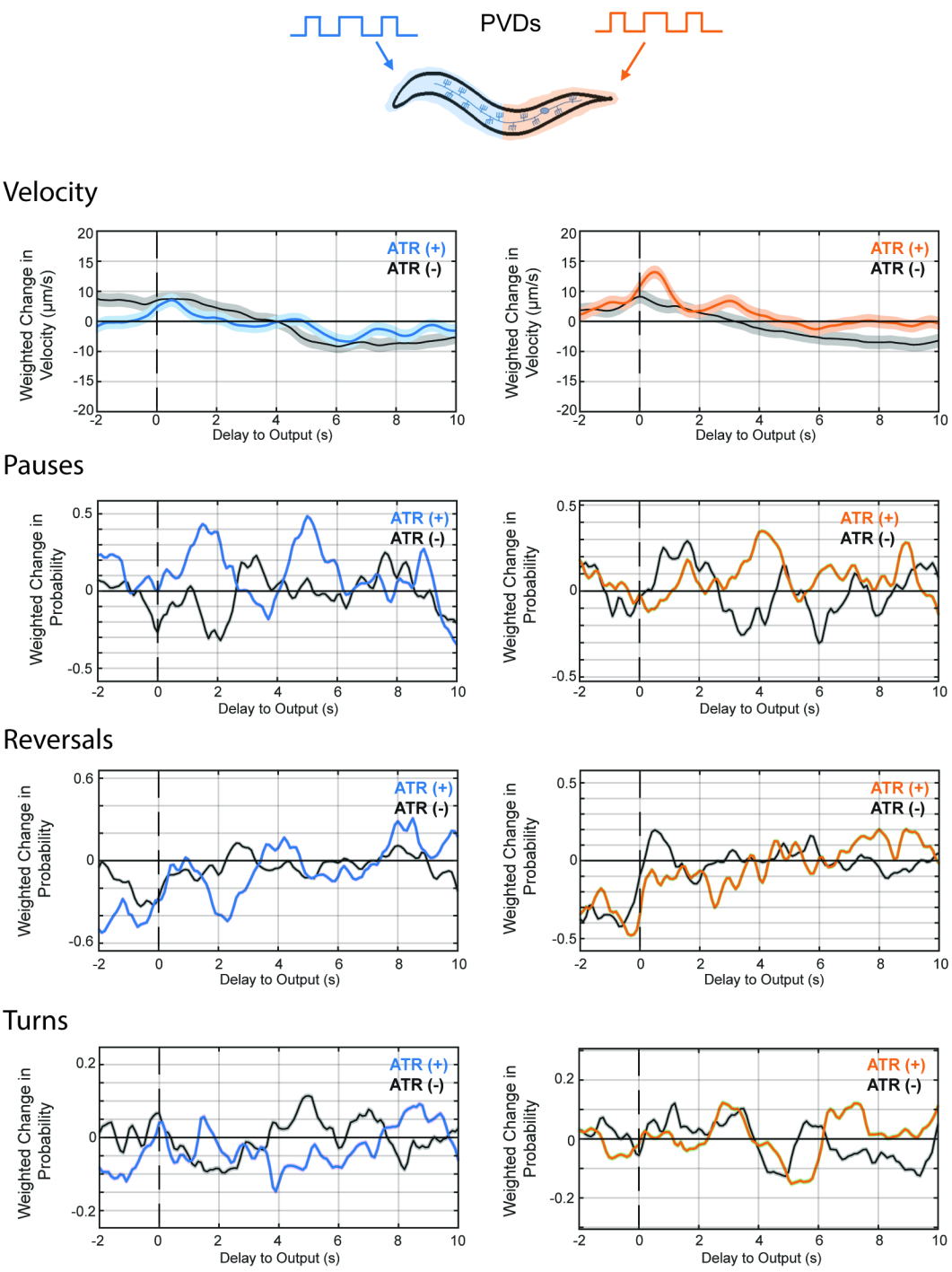

Figure B. 2 Additional linear filters for PVDs. Linear filters computed for various behaviors when stimulating the anterior (left) and posterior (right) PVDs with an m-sequence signal. Dark line and light shade represent BWA and SEM, respectively. Colored plots represent filters computed from ATR-fed animals, black plots

represent filters computed from control (not ATR-fed) animals. Sample sizes are listed Table S1.

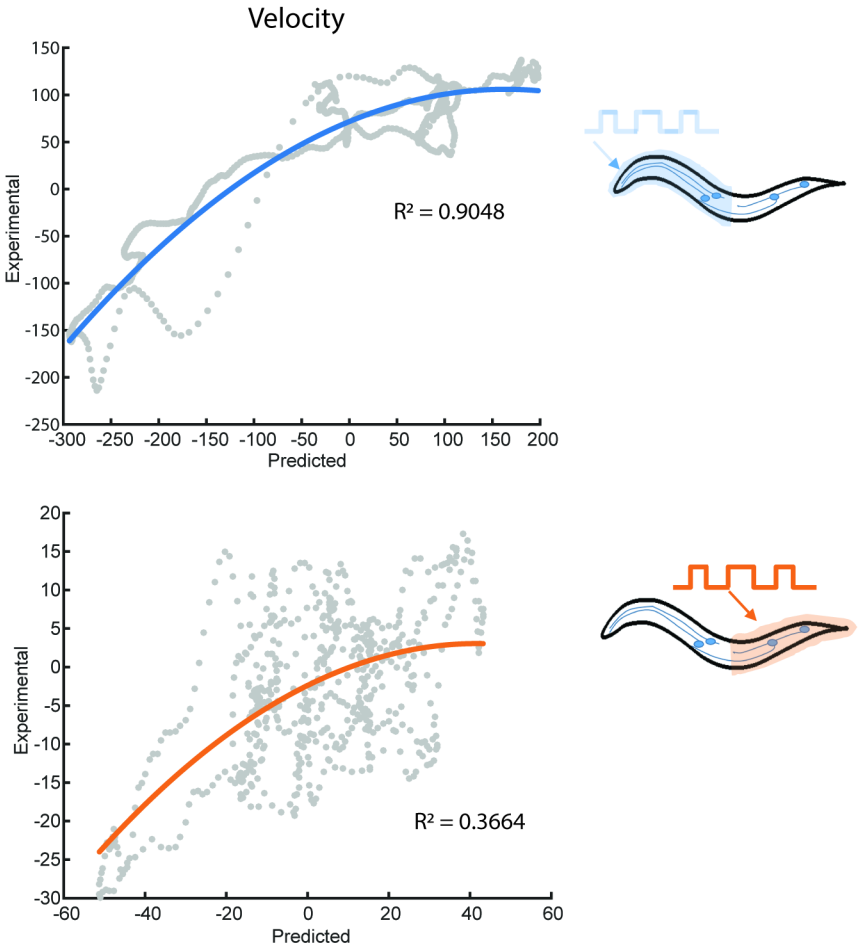

Figure B. 3 Static nonlinear filters for velocity. Static nonlinear filters fitted for predicted values from the linear filter (x-axis) against experimental values (y-axis) when stimulating the anterior TRNs. Linear filters and experimental values are subsets of data used in Figure 2 (n>1,730 for all conditions). Colored traces represent computed nonlinear filters and gray dots represent independent time-points from measured and predicted values..

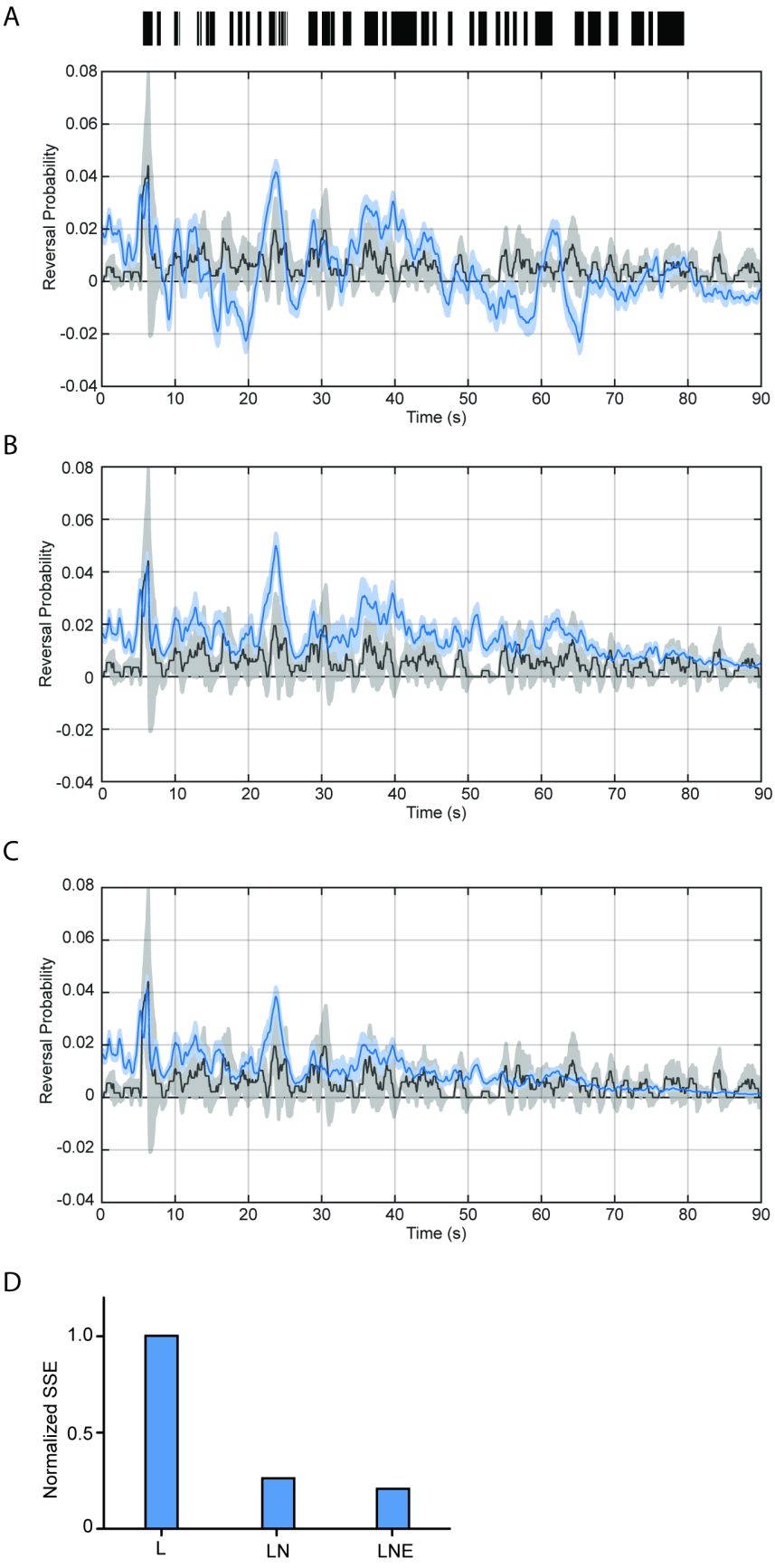
A
B
C
D
Reversal Probability
Time (s)
Normalized SSE
L
LN
LNE

Figure B. 4 Model predictions of reversal initiations. Comparison of model predictions of reversal transitions (blue) and experimental traces (black) when using A) only the linear filter, B) a linear-nonlinear (LN) model, and C) an additional exponential component (LNE). Dark line and shade represent average and SEM, respectively (n=31 animals). Probability of reversal transitions is computed as the average of animals initiating a reversal at that time point. D) Comparison of performance of models, computed as the sum of squared error (SSE) and normalized to the linear model performance value.

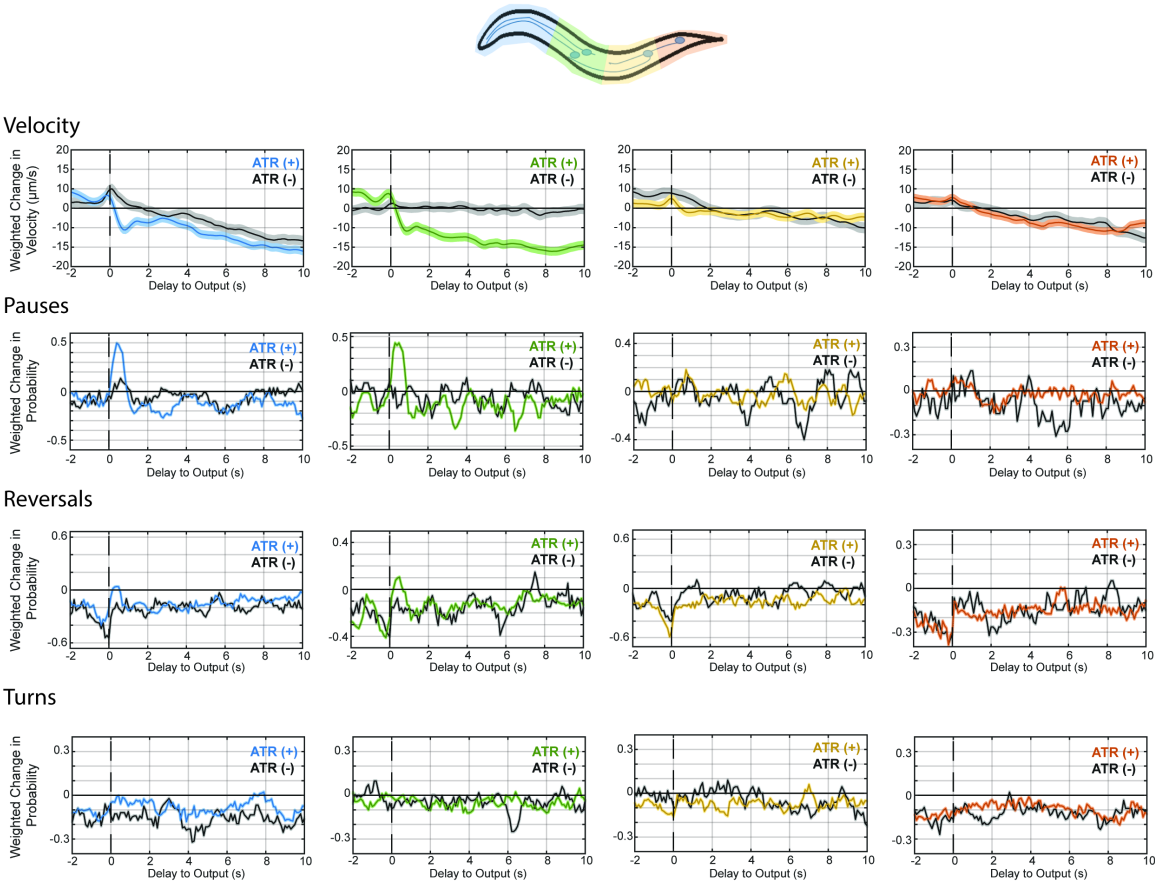

Figure B. 5 Additional filters for spatially refined analysis of TRNs Linear filters computed for various behaviors when stimulating the most anterior quarter (left), the second-most anterior quarter (second from left), the second-most posterior quarter (second from right), and the most posterior quarter (right) of the TRNs with an m-sequence signal. Dark line and light shade represent BWA and SEM, respectively. Colored plots represent filters computed from ATR-fed animals, black plots represent filters computed from control (not ATR-fed) animals. Sample Sizes are listed Table S1.

Figure	Segment	Behavior	ATR		nonATR	
			Time-Points/Events	Animals	Time-Points/Events	Animals
Figure 3.2	Anterior (1)	Acceleration + Pauses + Reversals	88031	113	75618	98
			1766	113	1715	98
	Anterior (2)	Acceleration + Pauses + Reversals	36597	47	38238	50
			492	47	422	50
	Posterior	Acceleration + Pauses + Reversals	56744	61	47281	49
			667	61	571	49
Appendix B. 1	Anterior (1)	Velocity	88025	113	75618	98
		Pauses	643	113	1026	98
		Reversals	549	113	163	98
		Turns	745	113	876	98
	Anterior (2)	Velocity	36606	47	38238	50
		Pauses	156	47	218	50
		Reversals	203	47	37	50
		Turns	176	47	242	50
	Posterior	Velocity	56742	61	47281	49
		Pauses	197	61	191	49
		Reversals	212	61	133	49
		Turns	280	61	272	49
Figure 3.5	Anterior	Acceleration (max)	53878	61	45479	51
		Acceleration (min)	53816	61	45404	51
		Pauses + Reversals	491	61	555	51
	Posterior	Acceleration (max)	53878	61	45479	51
		Acceleration (min)	53807	61	45464	51
		Pauses + Reversals	491	61	555	51
Appendix B. 2	Anterior	Velocity	53834	61	45474	51
		Pauses	98	61	62	51
		Reversals	94	61	161	51
		Turns	313	61	340	51
	Posterior	Velocity	53834	61	45474	51

		Pauses	98	61	62	51
		Reversals	94	61	161	51
		Turns	313	61	340	51
Figure 3.7 Appendix B. 3	Anterior	Acceleration	600	113		
		Velocity	600	113		
		Pauses + Reversals	600	113		
	Posterior	Acceleration	600	61		
		Velocity	600	61		
		Pauses + Reversals	600	61		
Figure 3.10	Seg1	Acceleration	58713	67	35477	40
		Pauses + Reversals	538	67	302	40
	Seg2	Acceleration	59683	69	30729	35
		Pauses + Reversals	434	69	160	35
	Seg3	Acceleration	56490	66	28875	33
		Pauses + Reversals	366	66	127	33
	Seg4	Acceleration	62815	71	32219	36
		Pauses + Reversals	545	71	194	36
Appendix B. 5	Seg1	Velocity	58662	67	35502	40
		Pauses	129	67	110	40
		Reversals	409	67	192	40
		Turns	272	67	134	40
	Seg2	Velocity	59650	69	30729	35
		Pauses	100	69	65	35
		Reversals	334	69	95	35
		Turns	323	69	165	35
	Seg3	Velocity	56480	66	28876	33
		Pauses	149	66	50	33
		Reversals	217	66	77	33
		Turns	251	66	112	33
	Seg4	Velocity	62808	71	32216	36
		Pauses	224	71	58	36
		Reversals	321	71	136	36
		Turns	342	71	145	36

Table B. 1 Sample sizes for computed linear filters in Chapter 3.

B.2 BWA with Eigenworm Analysis

In addition to the behaviors characterized in Chapter 3, I also performed "Eigenworm" analysis, a method for describing posture in *C. elegans* using dimensionality reduction [39]. Stephens et al. found that almost all of the possible body postures can be describe by a linear combination of four orthogonal postures, or principal components. Using this method, we can therefore quantify postures of animals in our recordings with four vectors, each representing the magnitude of an Eigenworm, or eigenvalue, at that time point.

We then performed the BWA computation to each of these quantified eigenvalue traces for animals being stimulated in the anterior TRNs. Not surprisingly, all of the filters were noisy and not statistically significant when compared to filters computed for non ATR-fed animals (Appendix B. 6). This is expected, as we do not qualitatively observe any key postures in response to an anterior touch.

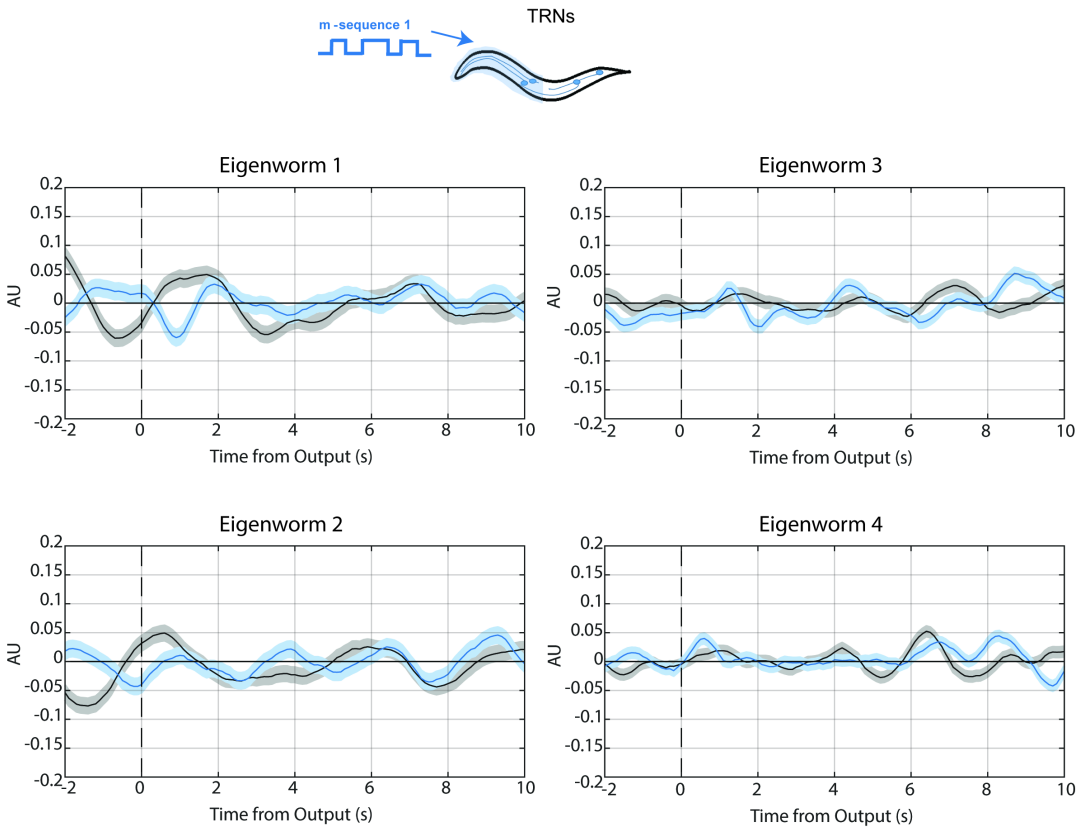

Appendix B. 6 Linear filters for anterior TRNs using Eigenworm Analysis.

Although we do not find significant filters when performing BWAs with the eigenvalues directly, computing BWAs with nonlinear relationships between eigenvalues yielded significant results. A key finding from Stephens et al. is that the first two Eigenworms function as an oscillator during forward and backward movement, and that the phase velocity between the two eigenvalues is a good indicator of animal velocity. We therefore computed the BWA with the phase velocity between the first two eigenvalues (Figure XX). Interestingly, the resulting filter is very similar to the filter for velocity from the same data set (compare to Appendix B. 1).

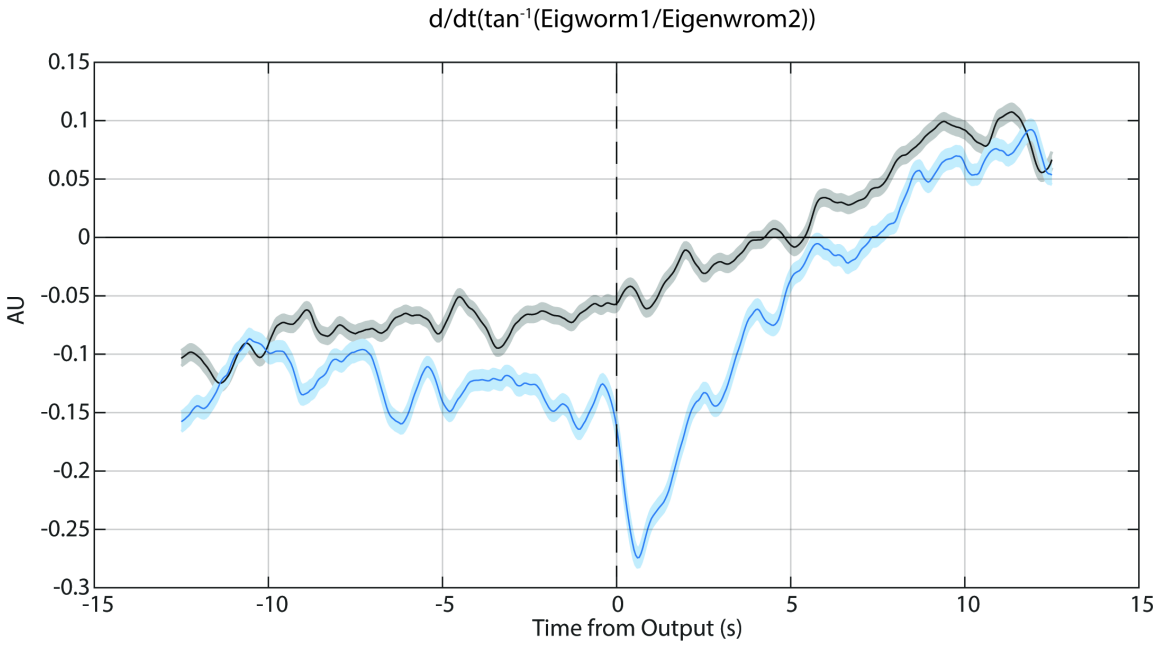

Appendix B. 7 Linear filter for anterior TRNs using the velocity of the phase between the first two Eigenworms.

REFERENCES

In general: You can use whichever style of references is used in your discipline, whether by alphabetical or by numbered citation. You can adjust the indentation by sliding the ruler 'nibs' on the ruler bar at the top of this window, if needed.

This template uses single spacing within the entries and doubles spaces after each one. These can be modified under **Format | Paragraph** but please note that double-spacing between entries and single-spacing within entries is required regardless of which method of citation and referencing you choose.

Select the first paragraph of the desired style and replace it with your first entry. When that entry is finished, hit **Return** to move to a new paragraph. Delete any other surrounding text.

This reference is formatted using a widely-used style called 'hanging indent.' The first line of each entry lines up with the margin. The other lines indent, causing the first line to 'hang'.

The "hanging indent" style is usually used when references are listed alphabetically by author in the "References" list and cited by author(s) and date within the text.

REFERENCES

1. Corsi, A.K., B. Wightman, and M.A.-O.h.o.o. Chalfie, *A Transparent Window into Biology: A Primer on Caenorhabditis elegans.* (1943-2631 (Electronic)).

2. Chalfie, M., et al., *THE NEURAL CIRCUIT FOR TOUCH SENSITIVITY IN CAENORHABDITIS-ELEGANS.* Journal of Neuroscience, 1985. **5**(4): p. 956-964.

3. Hobert, O., *The neuronal genome of Caenorhabditis elegans.* WormBook : the online review of C. elegans biology, 2013: p. 1-106.

4. Eric Kandel, J.S., Thomas Jessell, Steven Siegelbaum, A.J. Hudspeth, *Touch*, in *Principles of Neural Science, Fifth Edition*, J.S. Eric Kandel, Thomas Jessell, Steven Siegelbaum, A.J. Hudspeth, Editor. 2013, McGraw-Hill. p. 498-529.

5. Abbott, P.D.a.L.F., *Theoretical Neuroscience: Computational and Mathematical Modeling of Neural Systems*. 2001, The MIT Press

6. Goodman, M.B., *Mechanosensation.* WormBook : the online review of C. elegans biology, 2006: p. 1-14.

7. Goodman, M.B., et al., *Electrophysiological Methods for Caenorhabditis elegans Neurobiology*, in *Caenorhabditis Elegans: Cell Biology and Physiology, Second Edition*, J.H. Rothman and A. Singson, Editors. 2012. p. 409-436.

8. Pologruto, T.A., R. Yasuda, and K. Svoboda, *Monitoring neural activity and Ca2+ with genetically encoded Ca2+ indicators.* Journal of Neuroscience, 2004. **24**(43): p. 9572-9579.

9. Kerr, R.A., *Imaging the activity of neurons and muscles.* WormBook : the online review of C. elegans biology, 2006: p. 1-13.

10. Tian, L., et al., *Imaging neural activity in worms, flies and mice with improved GCaMP calcium indicators.* Nature Methods, 2009. **6**(12): p. 875-U113.

11. Kerr, R., et al., *Optical imaging of calcium transients in neurons and pharyngeal muscle of C-elegans.* Neuron, 2000. **26**(3): p. 583-594.

12. Chronis, N., M. Zimmer, and C.I. Bargmann, *Microfluidics for in vivo imaging of neuronal and behavioral activity in Caenorhabditis elegans.* Nature Methods, 2007. **4**(9): p. 727-731.

13. Clark, D.A., et al., *The AFD sensory neurons encode multiple functions underlying thermotactic behavior in Caenorhabditis elegans.* Journal of Neuroscience, 2006. **26**(28): p. 7444-7451.

14. Wen, Q., et al., *Proprioceptive Coupling within Motor Neurons Drives C. elegans Forward Locomotion.* Neuron, 2012. **76**(4): p. 750-761.

15. Hilliard, M.A., et al., *In vivo imaging of C-elegans ASH neurons: cellular response and adaptation to chemical repellents.* Embo Journal, 2005. **24**(1): p. 63-72.

16. Biron, D., et al., *An olfactory neuron responds stochastically to temperature and modulates Caenorhabditis elegans thermotactic behavior.* Proceedings of the National Academy of Sciences of the United States of America, 2008. **105**(31): p. 11002-11007.

17. Nagel, G., et al., *Light activation of channelrhodopsin-2 in excitable cells of Caenorhabditis elegans triggers rapid Behavioral responses.* Current Biology, 2005. **15**(24): p. 2279-2284.

18. Zhang, F., et al., *Multimodal fast optical interrogation of neural circuitry.* Nature, 2007. **446**(7136): p. 633-U4.

19. Boyden, E.S., et al., *Millisecond-timescale, genetically targeted optical control of neural activity.* Nature Neuroscience, 2005. **8**(9): p. 1263-1268.

20. Zhang, F., et al., *Channelrhodopsin-2 and optical control of excitable cells.* Nature Methods, 2006. **3**(10): p. 785-792.

21. Airan, R.D., et al., *Temporally precise in vivo control of intracellular signalling.* Nature, 2009. **458**(7241): p. 1025-1029.

22. Yizhar, O., et al., *Optogenetics in Neural Systems.* Neuron, 2011. **71**(1): p. 9-34.

23. Deisseroth, K., *Optogenetics.* Nature Methods, 2011. **8**(1): p. 26-29.

24. Liewald, J.F., et al., *Optogenetic analysis of synaptic function.* Nature Methods, 2008. **5**(10): p. 895-902.

25. Faumont, S., et al., *An Image-Free Opto-Mechanical System for Creating Virtual Environments and Imaging Neuronal Activity in Freely Moving Caenorhabditis elegans.* Plos One, 2011. **6**(9).

26. Lindsay, T.H., T.R. Thiele, and S.R. Lockery, *Optogenetic analysis of synaptic transmission in the central nervous system of the nematode Caenorhabditis elegans.* Nature Communications, 2011. **2**.

27. Schultheis, C., et al., *Optogenetic analysis of GABA(B) receptor signaling in Caenorhabditis elegans motor neurons.* Journal of Neurophysiology, 2011. **106**(2): p. 817-827.

28. Schultheis, C., et al., *Optogenetic Long-Term Manipulation of Behavior and Animal Development.* Plos One, 2011. **6**(4).

29. Gray, J.M., J.J. Hill, and C.I. Bargmann, *A circuit for navigation in Caenorhabditis elegans.* Proceedings of the National Academy of Sciences of the United States of America, 2005. **102**(9): p. 3184-3191.

30. Bargmann, C.I., *Chemosensation in C. elegans.* WormBook : the online review of C. elegans biology, 2006: p. 1-29.

31. Ryu, W.S. and A.D.T. Samuel, *Thermotaxis in Caenorhabditis elegans analyzed by measuring responses to defined thermal stimuli.* Journal of Neuroscience, 2002. **22**(13): p. 5727-5733.

32. Hedgecock, E.M. and R.L. Russell, *NORMAL AND MUTANT THERMOTAXIS IN NEMATODE CAENORHABDITIS-ELEGANS.* Proceedings of the National Academy of Sciences of the United States of America, 1975. **72**(10): p. 4061-4065.

33. Mori, I. and Y. Ohshima, *NEURAL REGULATION OF THERMOTAXIS IN CAENORHABDITIS-ELEGANS.* Nature, 1995. **376**(6538): p. 344-348.

34. Zariwala, H.A., et al., *Step response analysis of thermotaxis in Caenorhabditis elegans.* Journal of Neuroscience, 2003. **23**(10): p. 4369-4377.

35. Ha, H.I., et al., *Functional Organization of a Neural Network for Aversive Olfactory Learning in Caenorhabditis elegans.* Neuron, 2010. **68**(6): p. 1173-1186.

36. Zhang, Y., H. Lu, and C.I. Bargmann, *Pathogenic bacteria induce aversive olfactory learning in Caenorhabditis elegans.* Nature, 2005. **438**(7065): p. 179-184.

37. Baek, J.H., et al., *Using machine vision to analyze and classify Caenorhabditis elegans behavioral phenotypes quantitatively.* Journal of Neuroscience Methods, 2002. **118**(1): p. 9-21.

38. Feng, Z.Y., et al., *An imaging system for standardized quantitative analysis of C-elegans behavior.* Bmc Bioinformatics, 2004. **5**.

39. Stephens, G.J., et al., *Dimensionality and dynamics in the Behavior of C-elegans.* Plos Computational Biology, 2008. **4**(4).

40. Stephens, G.J., et al., *Emergence of long timescales and stereotyped behaviors in Caenorhabditis elegans.* Proceedings of the National Academy of Sciences of the United States of America, 2011. **108**: p. 7286-7289.

41. Stephens, G.J., et al., *From Modes to Movement in the Behavior of Caenorhabditis elegans.* Plos One, 2010. **5**(11).

42. Albrecht, D.R. and C.I. Bargmann, *High-content behavioral analysis of Caenorhabditis elegans in precise spatiotemporal chemical environments.* Nature Methods, 2011. **8**(7): p. 599-U120.

43. Swierczek, N.A., et al., *High-throughput behavioral analysis in C. elegans.* Nature Methods, 2011. **8**(7): p. 592-U112.

44. Ramot, D., et al., *The Parallel Worm Tracker: A Platform for Measuring Average Speed and Drug-Induced Paralysis in Nematodes.* Plos One, 2008. **3**(5).

45. Husson, S.J., et al., *Keeping track of worm trackers.* WormBook : the online review of C. elegans biology, 2013: p. 1-17.

46. Piggott, B.J., et al., *The Neural Circuits and Synaptic Mechanisms Underlying Motor Initiation in C. elegans.* Cell, 2011. **147**(4): p. 922-933.

47. Zheng, M., et al., *Calcium imaging of multiple neurons in freely behaving C. elegans.* Journal of Neuroscience Methods, 2012. **206**(1): p. 78-82.

48. Larsch, J., et al., *High-throughput imaging of neuronal activity in Caenorhabditis elegans.* Proceedings of the National Academy of Sciences of the United States of America, 2013. **110**(45): p. E4266-73.

49. Stirman, J.N., et al., *Real-time multimodal optical control of neurons and muscles in freely behaving Caenorhabditis elegans.* Nature Methods, 2011. **8**(2): p. 153-U78.

50. Leifer, A.M., et al., *Optogenetic manipulation of neural activity in freely moving Caenorhabditis elegans.* Nature Methods, 2011. **8**(2): p. 147-U71.

51. Shipley, F.B., et al., *Simultaneous optogenetic manipulation and calcium imaging in freely moving C-elegans.* Frontiers in Neural Circuits, 2014. **8**.

52. Guo, Z.V., A.C. Hart, and S. Ramanathan, *Optical interrogation of neural circuits in Caenorhabditis elegans.* Nature Methods, 2009. **6**(12): p. 891-U47.

53. Faumont, S. and S.R. Lockery, *The awake behaving worm: Simultaneous imaging of neuronal activity and behavior in intact animals at millimeter scale.* Journal of Neurophysiology, 2006. **95**(3): p. 1976-1981.

54. Xia, Y. and G.M. Whitesides, *SOFT LITHOGRAPHY.* Annual Review of Materials Science, 1998. **28**(1): p. 153-184.

55. Chung, K., M.M. Crane, and H. Lu, *Automated on-chip rapid microscopy , phenotyping and sorting of C . elegans.* Nature Methods, 2008: p. 1-7.

56. Caceres, I.d.C., et al., *Laterally Orienting C. elegans Using Geometry at Microscale for High-Throughput Visual Screens in Neurodegeneration and Neuronal Development Studies.* Plos One, 2012. **7**(4).

57. Lee, H., et al., *Quantitative screening of genes regulating tryptophan hydroxylase transcription in Caenorhabditis elegans using microfluidics and an adaptive algorithm.* Integrative Biology, 2013. **5**(2): p. 372-380.

58. Unger, M.A., et al., *Monolithic microfabricated valves and pumps by multilayer soft lithography.* Science, 2000. **288**(5463): p. 113-116.

59. de Carlos Cáceres, I., et al., *Automated screening of C. elegans neurodegeneration mutants enabled by microfluidics and image analysis algorithms.* Integrative Biology, 2018. **10**(9): p. 539-548.

60. Sleigh, J.N. and D.B. Sattelle, *C. ELEGANS MODELS OF NEUROMUSCULAR DISEASES EXPEDITE TRANSLATIONAL RESEARCH.* Translational Neuroscience, 2010. **1**(3): p. 214-227.

61. Verhaart, I.E.C., et al., *Prevalence, incidence and carrier frequency of 5q–linked spinal muscular atrophy – a literature review.* Orphanet Journal of Rare Diseases, 2017. **12**(1): p. 124.

62. Gennarelli, M., et al., *Survival Motor-Neuron Gene Transcript Analysis in Muscles from Spinal Muscular-Atrophy Patients.* Biochemical and Biophysical Research Communications, 1995. **213**(1): p. 342-348.

63. Lefebvre, S., et al., *Identification and characterization of a spinal muscular atrophy-determining gene.* Cell, 1995. **80**(1): p. 155-165.

64. Lefebvre, S., et al., *Correlation between severity and SMN protein level in spinal muscular atrophy.* Nature Genetics, 1997. **16**: p. 265.

65. Groen, E.J.N., K. Talbot, and T.H. Gillingwater, *Advances in therapy for spinal muscular atrophy: promises and challenges.* Nature Reviews Neurology, 2018. **14**: p. 214.

66. Dimitriadi, M., et al., *Conserved Genes Act as Modifiers of Invertebrate SMN Loss of Function Defects.* Plos Genetics, 2010. **6**(10).

67. Oprea, G.E., et al., *Plastin 3 is a protective modifier of autosomal recessive spinal muscular atrophy.* Science, 2008. **320**(5875): p. 524-527.

68. Monani, U.R., et al., *A single nucleotide difference that alters splicing patterns distinguishes the SMA gene SMN1 from the copy gene SMN2.* Human Molecular Genetics, 1999. **8**(7): p. 1177-1183.

69. Buckingham, S.D. and D.B. Sattelle, *Fast, automated measurement of nematode swimming (thrashing) without morphometry.* Bmc Neuroscience, 2009. **10**.

70. Sleigh, J.N., et al., *A novel Caenorhabditis elegans allele, smn-1(cb131), mimicking a mild form of spinal muscular atrophy, provides a convenient drug screening platform highlighting new and pre-approved compounds.* Human Molecular Genetics, 2011. **20**(2): p. 245-260.

71. Pulak, R., *Techniques for analysis, sorting, and dispensing of C-elegans on the COPAS (TM) flow-sorting system*, in *Methods in Molecular Biology*. 2006. p. 275-286.

72. Briese, M., et al., *Deletion of smn-1, the Caenorhabditis elegans ortholog of the spinal muscular atrophy gene, results in locomotor dysfunction and reduced lifespan.* Human Molecular Genetics, 2009. **18**(1): p. 97-104.

73. Di Giorgio, M.L., et al., *WDR79/TCAB1 plays a conserved role in the control of locomotion and ameliorates phenotypic defects in SMA models.* Neurobiology of Disease, 2017. **105**: p. 42-50.

74. Crane, M.M., K. Chung, and H. Lu, *Computer-enhanced high-throughput genetic screens of C. elegans in a microfluidic system.* Lab on a chip, 2009. **9**: p. 38-40.

75. Caceres, I.D., et al., *Laterally Orienting C. elegans Using Geometry at Microscale for High-Throughput Visual Screens in Neurodegeneration and Neuronal Development Studies.* Plos One, 2012. **7**(4).

76. Samara, C., et al., *Large-scale in vivo femtosecond laser neurosurgery screen reveals small-molecule enhancer of regeneration.* Proceedings of the National Academy of Sciences of the United States of America, 2010. **107**(43): p. 18342-18347.

77. Migliozzi, D., et al. *A microfluidic array for high-content screening at whole-organism resolution*. in *SPIE BiOS*. 2018. SPIE.

78. Gallotta, I., et al., *Neuron-specific knock-down of SMN1 causes neuron degeneration and death through an apoptotic mechanism.* Human Molecular Genetics, 2016. **25**(12): p. 2564-2577.

79. Dudley, N.R., B. Labbe Jc Fau - Goldstein, and B. Goldstein, *Using RNA interference to identify genes required for RNA interference.* (0027-8424 (Print)).

80. McIntire, S.L., et al., *THE GABAERGIC NERVOUS-SYSTEM OF CAENORHABDITIS-ELEGANS.* Nature, 1993. **364**(6435): p. 337-341.

81. Cho, Y., et al., *Automated and controlled mechanical stimulation and functional imaging in vivo in C. elegans.* Lab on a Chip, 2017. **17**: p. 2609-2618.

82. White, J.G., et al., *THE STRUCTURE OF THE NERVOUS-SYSTEM OF THE NEMATODE CAENORHABDITIS-ELEGANS.* Philosophical Transactions of the Royal Society of London Series B-Biological Sciences, 1986. **314**(1165): p. 1-340.

83. Sengupta, P. and A.D.T. Samuel, *Caenorhabditis elegans: a model system for systems neuroscience.* Current Opinion in Neurobiology, 2009. **19**(6): p. 637-643.

84. Chalfie, M. and M. Au, *Genetic control of differentiation of the Caenorhabditis elegans touch receptor neurons.* Science, 1989. **243**.

85. Wicks, S.R. and C.H. Rankin, *Integration of mechanosensory stimuli in Caenorhabditis elegans.* The Journal of neuroscience : the official journal of the Society for Neuroscience, 1995. **15**: p. 2434-44.

86. Suzuki, H., et al., *In vivo imaging of C-elegans mechanosensory neurons demonstrates a specific role for the MEC-4 channel in the process of gentle touch sensation.* Neuron, 2003. **39**: p. 1005-1017.

87. Albeg, A., et al., *C-elegans multi-dendritic sensory neurons: Morphology and function.* Molecular and Cellular Neuroscience, 2011. **46**: p. 308-317.

88. Chatzigeorgiou, M., et al., *Specific roles for DEG/ENaC and TRP channels in touch and thermosensation in C. elegans nociceptors.* Nature Neuroscience, 2010. **13**(7): p. 861-U106.

89. Li, W., et al., *The neural circuits and sensory channels mediating harsh touch sensation in Caenorhabditis elegans.* Nature Communications, 2011. **2**.

90. Husson, S.J., et al., *Optogenetic Analysis of a Nociceptor Neuron and Network Reveals Ion Channels Acting Downstream of Primary Sensors.* Current Biology, 2012. **22**(9): p. 743-752.

91. Nekimken, A.L., et al., *Pneumatic stimulation of C. elegans mechanoreceptor neurons in a microfluidic trap.* Lab Chip, 2017.

92. Stephens, G.J., et al., *Emergence of long timescales and stereotyped behaviors in Caenorhabditis elegans.* Proceedings of the National Academy of Sciences of the United States of America, 2011. **108**(18): p. 7286-7289.

93. Brown, A.E.X., et al., *A dictionary of behavioral motifs reveals clusters of genes affecting Caenorhabditis elegans locomotion.* Proceedings of the National Academy of Sciences of the United States of America, 2013. **110**(2): p. 791-796.

94. Yemini, E., et al., *A database of Caenorhabditis elegans behavioral phenotypes.* Nature Methods, 2013. **10**(9): p. 877-+.

95. Simoncelli, E.P., et al., *Characterization of Neural Responses with Stochastic Stimuli*. Cognitive Neurosciences Iii, Third Edition, ed. M.S. Gazzaniga. 2004. 327-338.

96. Chichilnisky, E.J., *A simple white noise analysis of neuronal light responses.* Network-Computation in Neural Systems, 2001. **12**(2): p. 199-213.

97. Ringach, D. and R. Shapley, *Reverse correlation in neurophysiology.* Cognitive Science, 2004. **28**(2): p. 147-166.

98. Sharpee, T.O., *Computational Identification of Receptive Fields.* Annual Review of Neuroscience, Vol 36, 2013. **36**: p. 103-120.

99. Nykamp Siam J Appl Math, D.Q., *WHITE NOISE ANALYSIS OF COUPLED LINEAR-NONLINEAR SYSTEMS* *. Society for Indiustrial and Applied Mathematics, 2003. **63**: p. 1208-1230.

100. Hunter, I.W. and M.J. Korenberg, *The identification of nonlinear biological systems: Wiener and Hammerstein cascade models.* Biological Cybernetics, 1986. **55**: p. 135-144.

101. Sakai, H.M., *WHITE-NOISE ANALYSIS IN NEUROPHYSIOLOGY.* Physiological Reviews, 1992. **72**(2): p. 491-505.

102. Chichilnisky, E.J. and D.A. Baylor, *Receptive-field microstructure of blue-yellow ganglion cells in primate retina.* Nature Neuroscience, 1999. **2**(10): p. 889-893.

103. Bredfeldt, C.E. and D.L. Ringach, *Dynamics of spatial frequency tuning in macaque V1.* Journal of Neuroscience, 2002. **22**(5): p. 1976-1984.

104. DeAngelis, G.C., I. Ohzawa, and R.D. Freeman, *Receptive-field dynamics in the central visual pathways.* Trends in Neurosciences, 1995. **18**: p. 451-458.

105. Ramirez, A., et al., *Spatiotemporal receptive fields of barrel cortex revealed by reverse correlation of synaptic input.* Nature Neuroscience, 2014. **17**(6): p. 866-875.

106. Behnia, R., et al., *Processing properties of ON and OFF pathways for Drosophila motion detection.* Nature, 2014. **512**(7515): p. 427-U443.

107. Kato, S., et al., *Temporal Responses of C. elegans Chemosensory Neurons Are Preserved in Behavioral Dynamics.* Neuron, 2014. **81**(3): p. 616-628.

108. Coen, P., J. Clemens, and A. Weinstein, *Dynamic sensory cues shape song structure in Drosophila.* Nature, 2014. **507**: p. 233-7.

109. Clemens, J., et al., *Connecting Neural Codes with Behavior in the Auditory System of Drosophila.* Neuron, 2015. **87**: p. 1332-1343.

110. Hernandez-Nunez, L., et al., *Reverse-correlation analysis of navigation dynamics in Drosophila larva using optogenetics.* eLife, 2015. **4**: p. e06225.

111. Gepner, R., et al., *Computations underlying Drosophila photo-taxis, odor-taxis, and multi-sensory integration.* eLife, 2015. **4**: p. e06229.

112. Liu, M., et al., *Temporal processing and context dependency in Caenorhabditis elegans response to mechanosensation.* eLife, 2018. **7**.

113. Suzuki, H., et al., *In vivo imaging of C-elegans mechanosensory neurons demonstrates a specific role for the MEC-4 channel in the process of gentle touch sensation.* Neuron, 2003. **39**(6): p. 1005-1017.

114. Eastwood, A.L., et al., *Tissue mechanics govern the rapidly adapting and symmetrical response to touch.* Proceedings of the National Academy of Sciences of the United States of America, 2015. **112**: p. E6955-63.

115. Huang, K.-M., P. Cosman, and W.R. Schafer, *Automated detection and analysis of foraging behavior in Caenorhabditis elegans.* Journal of Neuroscience Methods, 2008. **171**(1): p. 153-164.

116. Leifer, A.M., et al., *Optogenetic manipulation of neural activity in freely moving Caenorhabditis elegans.* Nature Methods, 2011. **8**: p. 147-U71.

117. Wicks, S.R., C.J. Roehrig, and C.H. Rankin, *A Dynamic Network Simulation of the Nematode Tap Withdrawal Circuit: Predictions Concerning Synaptic Function Using Behavioral Criteria.* Journal of Neuroscience, 1996. **16**.

118. Nykamp, D.Q. and D.L. Ringach, *Full identification of a linear-nonlinear system via cross-correlation analysis.* Journal of Vision, 2002. **2**(1).

119. Rose, J.K. and C.H. Rankin, *Analyses of habituation in Caenorhabditis elegans.* Learning & Memory, 2001. **8**(2): p. 63-69.

120. Timbers, T.A., et al., *Intensity discrimination deficits cause habituation changes in middle-aged Caenorhabditis elegans.* Neurobiology of Aging, 2013. **34**(2): p. 621-631.

121. Chatzigeorgiou, M., et al., *Specific roles for DEG/ENaC and TRP channels in touch and thermosensation in C. elegans nociceptors.* Nature Neuroscience, 2010. **13**: p. 861-U106.

122. Kruger, M. and W.A. Linke, *The giant protein titin: a regulatory node that integrates myocyte signaling pathways.* (1083-351X (Electronic)).

123. Kontrogianni-Konstantopoulos, A., et al., *Muscle giants: molecular scaffolds in sarcomerogenesis.* (0031-9333 (Print)).

124. Mayans, O., et al., *Structural basis for activation of the titin kinase domain during myofibrillogenesis.* (0028-0836 (Print)).

125. Bogomolovas, J., et al., *Titin kinase is an inactive pseudokinase scaffold that supports MuRF1 recruitment to the sarcomeric M-line.* (2046-2441 (Electronic)).

126. Lange, S., et al., *The kinase domain of titin controls muscle gene expression and protein turnover.* (1095-9203 (Electronic)).

127. Hu, S.-H., et al., *Insights into autoregulation from the crystal structure of twitchin kinase.* Nature, 1994. **369**: p. 581.

128. Lei, J., et al., *Protein kinase domain of twitchin has protein kinase activity and an autoinhibitory region.* Journal of Biological Chemistry, 1994. **269**(33): p. 21078-21085.

129. Gräter, F., et al., *Mechanically Induced Titin Kinase Activation Studied by Force-Probe Molecular Dynamics Simulations.* Biophysical Journal, 2005. **88**(2): p. 790-804.

130. Puchner, E.M., et al., *Mechanoenzymatics of titin kinase.* (1091-6490 (Electronic)).

131. von Castelmur, E., et al., *Identification of an N-terminal inhibitory extension as the primary mechanosensory regulator of twitchin kinase.* (1091-6490 (Electronic)).

132. Heierhorst, J., et al., *Substrate specificity and inhibitor sensitivity of Ca2+/S100-dependent twitchin kinases.* (0014-2956 (Print)).

133. Fouad, A.D., et al., *Distributed rhythm generators underlie Caenorhabditis elegans forward locomotion.* eLife, 2018. **7**: p. e29913.

134. Gao, S., et al., *Excitatory motor neurons are local oscillators for backward locomotion.* eLife, 2018. **7**: p. e29915.

135. Williams, R.M., et al., *Autophosphorylation Is a Mechanism of Inhibition in Twitchin Kinase.* (1089-8638 (Electronic)).

136. Evers, T.H., et al., *Quantitative understanding of the energy transfer between fluorescent proteins connected via flexible peptide linkers.* (0006-2960 (Print)).

137. Ohashi, T., et al., *An experimental study of GFP-based FRET, with application to intrinsically unstructured proteins.* (0961-8368 (Print)).

138. Griesbeck, O., et al., *Reducing the environmental sensitivity of yellow fluorescent protein. Mechanism and applications.* (0021-9258 (Print)).

139. Zacharias, D.A., et al., *Partitioning of lipid-modified monomeric GFPs into membrane microdomains of live cells.* (1095-9203 (Electronic)).

140. Benian, G.M., M.E. L'Hernault Sw Fau - Morris, and M.E. Morris, *Additional sequence complexity in the muscle gene, unc-22, and its encoded protein, twitchin, of Caenorhabditis elegans.* (0016-6731 (Print)).

141. Moerman, D.G., et al., *Identification and intracellular localization of the unc-22 gene product of Caenorhabditis elegans.* (0890-9369 (Print)).

142. Greene, D.N., et al., *Single-Molecule Force Spectroscopy Reveals a Stepwise Unfolding of Caenorhabditis elegans Giant Protein Kinase Domains.* Biophysical Journal, 2008. **95**(3): p. 1360-1370.